Diffusion MRI of the ex vivo porcine heart

Mazzoli, V.

Award date:
2013

Technische Universiteit Eindhoven

Biomedical Engineering Department
Biomedical NMR

Master Thesis Project

Diffusion MRI of the *ex vivo* porcine heart

Student:
Valentina Mazzoli (117218)

Defense Committee:
Gustav Strijkers
Klaas Kopinga
Klaas Nicolay
Martijn Froeling
Aart Nederveen

September 23, 2013

Abstract

In conventional Diffusion Tensor Imaging (DTI), water diffusion is assumed to occur in a free and unrestricted environment, in which the diffusion profile of water molecules can be modelled to be Gaussian. However, in biological tissue the complex microstructure makes the diffusion process highly hindered or even restricted. The aim of this study was to get a better understanding of the non Gaussian diffusion profile in the *ex vivo* porcine heart using different DW-MRI (Diffusion Weighted Magnetic Resonance Imaging) techniques and different post processing approaches.

Previous studies showed a non mono-exponential signal decay in cardiac tissue due to the effect of the applied b-values. Evidence was also found of dependence of the estimation of diffusion parameters on the experimental diffusion time. In this study, experiments with different diffusion times and different b-values were performed and the results connected to microstructure at the cellular level. Based on experimental observation and data fitting including both conventional DTI and bi-exponential models, it was speculated that water moving in the direction perpendicular to the axis of the cell is always in regime of restricted diffusion, while along the cell different regimes can be observed by tuning the experimental diffusion time.

A second MRI approach used Diffusion Kurtosis Imaging (DKI), which quantifies the level of diffusion restriction by providing a measure of deviation of the diffusion profile from a Gaussian shape. This method was found to be more sensitive to tissue microstructure than conventional DTI-based approaches, and kurtosis maps provided contrast between left and right ventricle, which was not visualized in conventional diffusion maps.

The last approach was to try to connect regional differences of diffusion parameters across the heart and deviations from a Gaussian diffusion profile with the presence of "crossing fibers". Partial volume effects are in fact to be expected in MRI scans, since previous histological studies showed the presence of intersecting myolaminae across the cardiac wall, which are intersecting each others. Constrained Spherical Deconvolution (CSD) method was proposed in order to overcome the "crossing fibers" problem, and used for data fitting and fiber tracking. The results show the presence of crossing fiber tracts at the level of a single voxel, which are not correctly identified with standard DTI.

Contents

I Introduction and theoretical background **4**

1 Introduction **5**

2 Structure of the heart **7**
2.1 Gross morphology 7
2.2 Microstructure 8
2.2.1 Fiber architecture 9
2.3 Macrostructure 10
2.3.1 Laminar structure 10
2.4 Models 11

3 Diffusion Imaging **13**
3.1 Principles of diffusion 13
3.1.1 Free self diffusion 14
3.1.2 Hindered and restricted diffusion 16
3.2 Diffusion Weighted MRI 19
3.2.1 Stejskal-Tanner sequence 19
3.2.2 Diffusion encoding 20
3.2.3 PGSE in the narrow pulse approximation 23
3.3 Diffusion Tensor Imaging 24
3.3.1 Obtaining the diffusion tensor from MR signal 26
3.3.2 Scalar parameters from the diffusion tensor 27
3.3.3 Fiber tractography 27
3.4 DTI of the heart 29

4 Beyond DTI **32**
4.1 Introduction to q-space 34
4.2 Multiple tensor approaches 35
4.3 DSI 35
4.3.1 DSI of the heart 36
4.4 HARDI 37
4.4.1 q-ball imaging 38
4.4.2 SD and CSD 39
4.5 Diffusion Kurtosis 41
4.5.1 DKI 41
4.6 Models of diffusion 44

II Results and discussion **46**

4.6.1 Tissue preparation . . . 47
4.6.2 Imaging . . . 47
4.6.3 Data processing . . . 48

5 Mixing time experiment **49**
5.1 Ex vivo heart at 3 T . . . 49
5.1.1 Imaging . . . 49
5.1.2 Data processing . . . 51
5.2 Ex vivo heart at 9.4 T . . . 52
5.2.1 Imaging . . . 52
5.2.2 Data processing . . . 52
5.3 Results . . . 52
5.3.1 Bi-exponential fitting . . . 53
5.3.2 Mono-exponential fitting of different shells . . . 55
5.4 Discussion . . . 57
5.5 Conclusions . . . 62

6 Kurtosis and Multishell analysis **64**
6.1 DKI . . . 64
6.1.1 Imaging . . . 64
6.1.2 Data processing . . . 64
6.1.3 Results . . . 65
6.2 Two-Component Diffusion Tensor Analysis . . . 67
6.2.1 Data processing . . . 67
6.2.2 Results . . . 67
6.3 Discussion . . . 69
6.4 Conclusions . . . 73

7 HARDI and DTI **74**
7.1 Phantom of crossing fibers . . . 74
7.1.1 Imaging . . . 74
7.1.2 Data processing . . . 74
7.1.3 Results . . . 75
7.1.4 Discussion and conclusion . . . 78
7.2 Ex vivo heart at 3 T . . . 78
7.2.1 Imaging . . . 78
7.2.2 Data processing . . . 79
7.2.3 Results . . . 79
7.3 Ex vivo heart at 9.4 T . . . 80
7.3.1 Imaging . . . 80
7.3.2 Data processing . . . 82
7.3.3 Results . . . 82
7.4 Discussion . . . 85
7.5 Conclusion . . . 87

8 General conclusions and future work **88**

Bibliography **89**

Part I

Introduction and theoretical background

Chapter 1

Introduction

Cardiac optimal function strongly depends on the geometrical structure and arrangement of the cardiac muscle fibers (myocytes). Interestingly, despite cardiac anatomy has been a topic of study for more than 4 centuries, some aspects of how myocytes are arranged in the cardiac wall still are unknown and no consensus has been reached about a global model of cardiac anatomy. One of the main difficulties in providing a general model is the presence of myolaminae, which are groups of fibers arranged in sheet-like structures, separated by cleavage planes. These myolaminae are geometrically arranged in an extremely complex way, which is not yet described and understood.
Many cardiac pathologies can affect myocardial mechanics, which may lead to dysfunction of the myocardium and suboptimal pump function of the heart. Therefore, a fuller understanding of normal and abnormal myocardial structure and function could aid in improving interpretations and predictions of changes in the diseased heart. The importance of providing a geometrical model of cardiac architecture is then of paramount importance not only for understanding how tension and electrical excitation propagates throughout the myocardium during contraction in healthy hearts, but also to study how this optimal propagation is affected by pathological conditions and diseases.
Diffusion MRI has been used as a tool for investigating cardiac fiber structure for about 20 years and offers great advantages over methods previously used, such as histology and dissection. In fact it is a completely non invasive technique, fast and relatively easy to implement. Furthermore it doesn't require the use of any contrast agent, since the contrast in Diffusion MRI is provided by the movement of water molecules naturally present in the body.
The most common Diffusion MRI technique used nowadays in cardiac muscles is Diffusion Tensor Imaging (DTI), which exploits the characteristic anisotropy of cellular structure to infer their orientation. However DTI heavily relies on a number of assumptions which are not necessarily holding in cardiac muscle cells.
A first limitation of DTI is its intrinsic inability to correctly identify structure that due to partial volume effects are crossing in a single image voxel. Since there are evidences of myolaminae crossing in the cardiac wall, the technique is probably not suitable if one wants to fully describe cardiac cell geometry, including the presence of myolaminae.
Some other Diffusion Imaging techniques such as HARDI have been applied in brain tissue to solve the "crossing fibers" problem, and to correctly identify crossing fibers within a voxel. In this thesis the HARDI approach is implemented in cardiac tissue and some preliminary results are shown.
Another assumption underlying the DTI model is that the diffusion profile in the tissue of interest has a Gaussian profile, which is not necessarily the case in real biological tis-

sues. There are some evidences in fact of deviation of the displacement profile of water molecules from a Gaussian shape for high b-values, although no studies were carried out to connect this deviation to characteristic of the cellular structure. Very little in fact is known about the diffusion behavior in cardiac muscles for high b-values and which characteristics influence the restricted water signal observed.
Nowadays in-vivo cardiac Diffusion MRI is becoming feasible for clinical studies [44], and it is then of great importance to understand what is actually measured in a Diffusion MRI experiment, which information can be correctly retrieved from the acquired data and whether some characteristics could be used as a marker of cardiac diseases.
In order to provide some deeper knowledge about diffusion in cardiac muscles, in this thesis the diffusion behavior for different b-values and different diffusion times is also investigated, and data are fitted to a kurtosis and a slow-exchange limit two compartments model to check whether more accurate information about microscale and cellular characteristics can be inferred using different Diffusion MRI approaches.

Chapter 2

Structure of the heart

The general organization of cardiac tissue has been a topic of research for many centuries. The heart is a muscular organ characterized by different levels of complexity[20]. While the general gross anatomy and global function of the heart is well known, together with detailed information about its micro- an ultra-structure, a detailed picture of the heart as a whole is still lacking.
The fundamental contractile cell of the heart is the myocyte, also referred to as myofiber. Myofibers are the building blocks of the heart, and there is general consensus on the fact that the way they are geometrically organized is fundamental for optimal contraction. Many observations have been made on myofiber architecture, but it is still not completely understood how those fibers are precisely arranged and connected between each others and how they determine the global heart function.
Much of the present knowledge about cardiac anatomy comes from traditional anatomical techniques, such as dissection and histological studies. These techniques however have several limitations: (i) they are often subjective, so hardly reproducible and qualitative, rather than quantitative, (ii) they are destructive, (iii) time consuming and (iv) inherently two-dimensional[19].
Improved knowledge about cardiac tissue architecture was reached in the last 20 years thanks to DT-MRI. However, despite extensive efforts and recent advances in imaging techniques, a complete model for cardiac architecture and functions is still lacking.
In this chapter an anatomical overview of the human heart at different levels will be given.

2.1 Gross morphology

The main function of the heart is to pump blood into the systemic and pulmonary circulation. It is a muscular organ that consists of 4 cavities: 2 atria (left and right) and 2 ventricles (left and right). The right atrium (RA) collects blood from the systemic circulation and returns deoxygenated blood from the body to the right ventricle (RV). The right ventricle extends from the right atrium to the apex and has the main function of sending deoxygenated blood from the body to the lungs. The blood flows from the RA to the RV through the Tricuspid valve and is then pumped through the Pulmonary valve into the respiratory system. Blood from the respiratory system is collected in the left atrium from where it flows through the Mitral valve into the left ventricle (LV). The blood in the left ventricle is then pumped through the Aortic valve into the systemic circulation. The LV wall is much thicker than the RV wall, as we may expect considering the fact that the systemic circulation is much larger than the respiratory circulation and therefore gives more resistance to the outflowing blood. The atria are separated from the

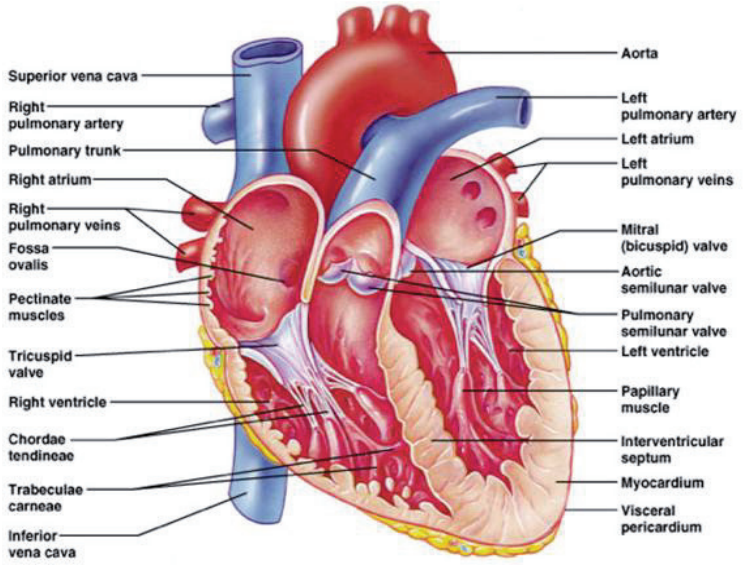

Figure 2.1: Schematic drawing of the gross anatomy of the heart.

respective ventricles by the base. The point farthest away from the base is called the apex.

The heart wall enclosing the chambers is made up of three layers. Covering the cardiac muscle is the epicardium, a serous membrane reducing the friction the heart experiences as it beats. The inner surface of the heart chambers is covered with a sheet of endothelium called the endocardium. It lines the ventricles as well as the valves and is continuous with the endothelium of the vessels entering and leaving the heart. Situated in between these sheets is the myocardium, the muscular layer that actually contracts. It is mainly composed of cardiac muscle cells, also called myocytes. The way these myocytes are organized in the myocardium is essential for optimal functioning of the heart.

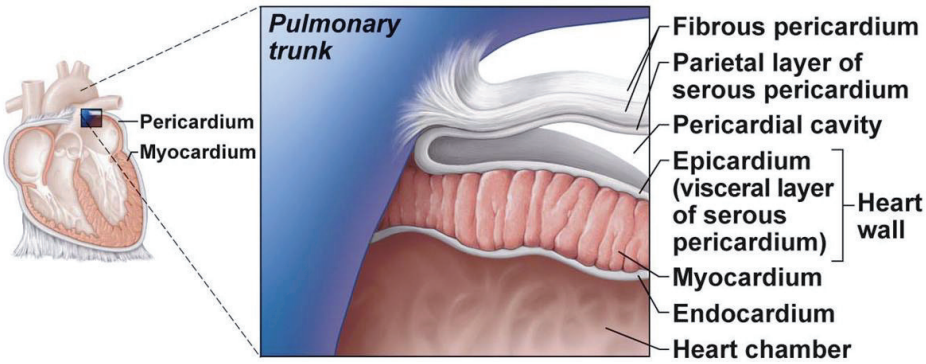

Figure 2.2: Schematic drawing of the different layers that make up the heart wall.

2.2 Microstructure

Muscle cells (myocytes) are long cigar-shaped cells, with a length typically ranging from 50 to 150 μm and a diameter ranging from 10 to 20 μm. The cells of cardiac muscle have

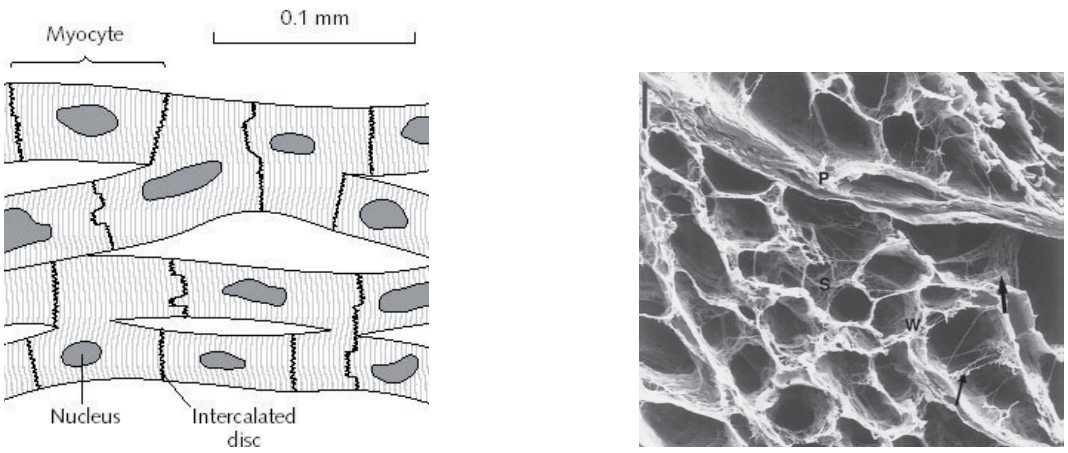

Figure 2.3: A) Schematic drawing of cardiac muscle cells. B) Electron microscopy of connective tissue skeletal of the human heart (transversal section), where the cellular elements have been dissolved. The perimysium (P) envelops groups of myocytes. The endomysium, supports and connects individual cells. The endomysial weave (W) envelops each individual myocyte and is connected to adjacent myocytes by lateral struts (s) presenting branches of variable size and extension. The size of the reference bar is $20\mu m$.

typically only one or two nuclei and can be found only in the heart. Myocytes are joined to their neighbors via the so called intercalated disc, and at their ends terminal abutments are usually with more than one cell, resulting in a mesh-like structure. The intercalated disc is a structure typical of cardiac muscle, and provides a strong mechanical connection among the cells allowing the muscle impulses to travel fast from cell to cell. A schematic drawing of the interconnections of myocytes between each others is shown in figure 2.3.
The extracellular space occupies only a limited amount of volume in skeletal muscles (around 10%) and it consists of connective tissues. The connective tissue has a honeycomb-like structure 2.3 and has a primary role in preserving the structure of the heart.

2.2.1 Fiber architecture

Due to the complex arrangement of cells in the heart, the definition of a main fiber direction is not as straightforward as in the case of skeletal muscles. One of the most used definitions of fiber directions is however the one proposed by Gilbert [19]: given the cylindrical shape, it is possible to define at every cardiac location, a principal direction of the cell, that corresponds with its long axis. The nucleus of the myocyte, characterized by an ellipsoidal shape, is normally aligned with this axis.
Seen from the apex the subepicardial fibers follow a left-handed helical path, while the subendocardial fibers follow the path of a right-handed helix. In the midwall region the fiber pathways are mainly circumferential. This fiber configuration has been shown to balance stress and strain across the ventricular wall, allowing the different tissue components to operate in a optimal mechanical regime [54][11].

2.3 Macrostructure

The myocytes in the myocardium are grouped together in layers 3 or 4 cells thick. These groups are referred to as myolaminae or sheets and are shown in figure 2.4. Extracellular collagen fibers provide tight coupling within the sheets, but loose coupling between adjacent sheets, which allows sliding of sheets during the cardiac cycle [40]. The general laminar structure is not rigid, since different myolaminae are shown to merge and divide and myofibers typically run from one sheet to another, surrounded by a collagen network. During the ventricular contraction, transmural wall thickening is observed, and that has a primary function in the ejection of blood toward the general body circulation. This is in fact required to generate the force needed to overcome the resistance in the circulation. The arrangement of myocytes in sheets has a really important role in the influence of spread of activation in the myocardium and in the thickening mechanism. It is hypothesized that the laminar model of the heart can be used to explain the general structural change during systole, since the typical 14% myocyte shortening leads to only an ∼8% increase in myocyte diameter, which cannot fully account for the observed 28–50% increase in average wall thickness. Such amount of wall thickening can be explained only by taking into account the secondary changes in fiber and sheet orientation. In particular, the sliding of sheets with respect to each other is considered as a primary mechanism of myocardial wall thickening [10].

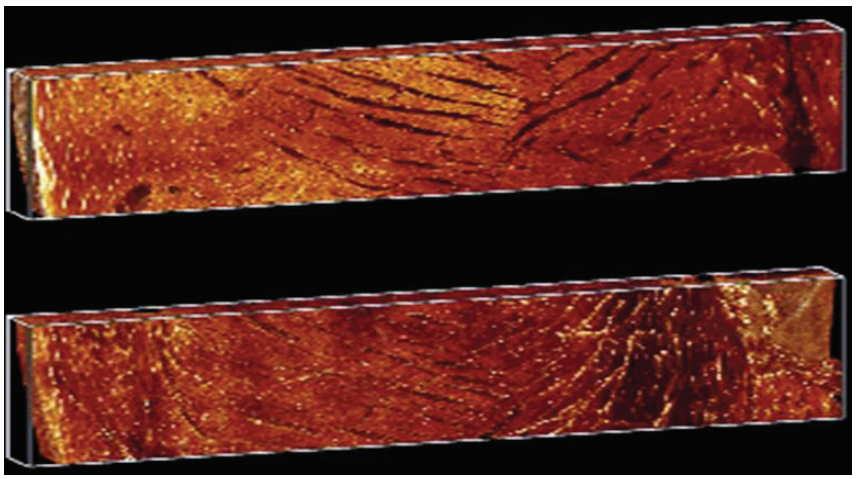

Figure 2.4: Confocal microscopy of a rat heart. The outermost face of the tissue block is the longitudinal—radial cardiac plane. Reproduced from [19]

2.3.1 Laminar structure

The geometrical arrangement of myocytes in the heart wall shows a high level of regularity, with fiber orientations with respect to the main axis of the heart changing smoothly from -60° at endocardium to $+60^\circ$ at epicardium and similar patterns shown across different species, as mentioned in the previous section.
This regularity is however lost if we consider the cardiac structure on a higher order. In fact the arrangement of myolaminae in the heart wall does not show the same characteristics in the different regions. This can be observed in figure 2.5. In this T_1 weighted image the natural contrast between collagen layers and surrounding tissue is enhanced by

the use of Gd-DTPA contrast agent. The collagen layers, which appear brighter than myolaminae in the image, can be used to infer the myolaminae orientation. As can be seen, the myolaminar orientation seems to change smoothly going from endo- to epicardium. However close to endocardium we can observe these laminae branching and intersecting at approximately 90°. The laminar structure appears more loose at the subendocardium, becoming more compact toward the subepicardium. Laminar structure is seen to be absent closest to the epicardium.

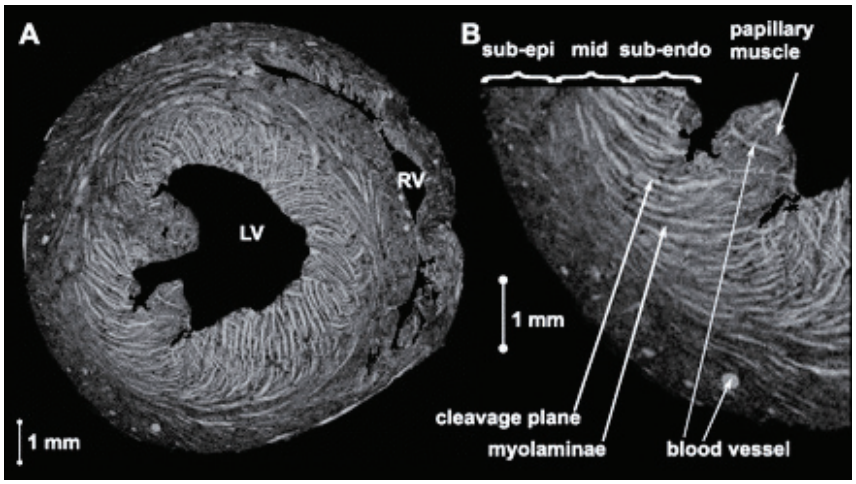

Figure 2.5: Laminar architecture in a near-equatorial short-axis slice.A)Short-axis slice. B)Magnified region of short axis slice Reproduced from [18]

2.4 Models

Due to the contradiction between the high level of symmetry of helical organization of fibers and asymmetric branching and merging of laminae, several models of cardiac structure have been presented in literature, and they are often incompatible with each others. Every model proposed so far refers to different levels of cardiac structure. i.e. focusing more on the fibers, or on the laminae. Some of the models can be found in the review paper by Gilbert et al.[19].
The recent debate about cardiac structure has focused mainly on two models: (i) the orthotropic myolaminar structure and (ii) the Helical Ventricular Myocardial Band (HVMB). The first model [40] refers to the possibility, for every given point of the myocardium, to define three principal orthogonal directions. These are oriented respectively along the axis of the fiber, perpendicular to the axis of the fiber in the direction parallel to the fiber sheet and perpendicular to the fiber sheet plane. The easiest version of the orthotropic model is schematically illustrated in figure 2.6. Here muscle layers are represented as transmural sheets, that are twisted in such a way to accommodate the known local fiber orientation. This simple description can't include the branches between adjacent layers. On the other hand, the HVMB model describes the cardiac muscle as a continuous muscle band. This band is oriented spatially as a helix formed by basal and apical loops [59]. According to this model, the continuity of the muscle would allow the complete "unwrapping" of the heart along natural cleavage planes.

Whereas both models are somehow compatible with the known helical structure of myofibers, they differ in the way the laminar organization is included. Further research

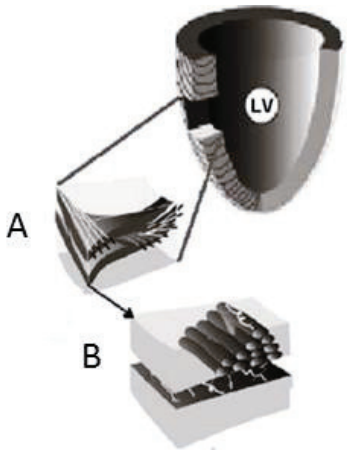

Figure 2.6: Schematic drawing of cardiac microstructure. (A) Transmural segments of myocardium contains layers of myofibers. (B) Adjacent layers are connected via collagen layers. The white lines indicate the component of extracellular collagen matrix . Reproduced from [40]

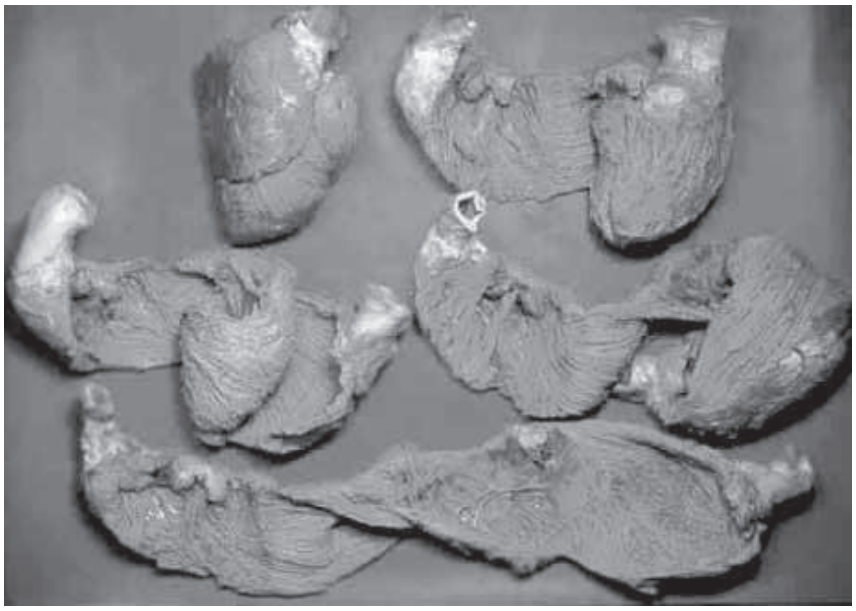

Figure 2.7: Consecutive stages of the unwinding or the ventricular myocardial band, as described by the Helical Ventricular Myocardial Band model. Reproduced from [59]

is needed to get a better understanding of the laminar structure and we propose that Diffusion Imaging with high angular resolution acquisition (HARDI) is one of the most promising techniques to achieve this goal.

Chapter 3

Diffusion Imaging

Diffusion Weighted Magnetic Resonance Imaging (DW-MRI) refers to a family of MR techniques used for measuring the dephasing of spins of protons in the presence of a magnetic field gradient. The amount of spin dephasing in a given object can be exploited to calculate diffusion of water molecules and, under certain assumptions, infer geometrical characteristic of the object itself. DW-MRI techniques are commonly applied in a large variety of fields, but they are of particular interest when used for studying biological tissues.
In the first part of this chapter the basic physical principles of diffusion will be explained. In the second part the techniques for measuring diffusion will be introduced. Finally, applications of DW-MRI will be presented, with particular interest in the study of the heart.

3.1 Principles of diffusion

Diffusion is the random displacement of molecules under the influence of temperature and/or concentration gradients.
Let's consider for example a solute that is present in a very low concentration in a fluid solvent. Let $n(\mathbf{r}, t)$ be the non-equilibrium density of solutes (number of particle per unit volume) at position $\mathbf{r}$ at time t. This density is related to the notion of flux by the continuity equation:

$$\frac{\partial}{\partial t} n(\mathbf{r}, t) = -\nabla \cdot \mathbf{J}(\mathbf{r}, t) \tag{3.1}$$

where $\mathbf{J}(\mathbf{r}, t)$ is the non-equilibrium average flux of solute particles at position $\mathbf{r}$ at time t.
The continuity equation expresses the conservation of mass, i.e. the density in a given region of the fluid can change in time because particles flow in and out of the region, but particles cannot be created or destroyed (we are here neglecting the possibility of chemical reactions to occur), so that the total number of solute molecules is constant.
Equation 3.1 can be simply proved considering any arbitrary volume Ω within our system (solute+solvent). The total number of solute molecules present in the given volume Ω is by definition:

$$N_\Omega(t) = \int_\Omega d\mathbf{r} n(\mathbf{r}, t) \tag{3.2}$$

Since mass flow trough the boundary S of the volume Ω is the only feasible mechanism for changing $N_\Omega(t)$, we have:

$$\frac{dN_\Omega(t)}{dt} = -\int_S d\mathbf{S}\cdot\mathbf{J}(\mathbf{r},t) = -\int_\Omega d\mathbf{r}\nabla\cdot\mathbf{J}(\mathbf{r},t) \tag{3.3}$$

where the second equality is derived using the divergence theorem. However, from 3.2:

$$\frac{dN_\Omega(t)}{dt} = \int_\Omega d\mathbf{r}\frac{\partial n(\mathbf{r},t)}{\partial t} \tag{3.4}$$

Putting the last two equations together gives:

$$0 = \int_\Omega d\mathbf{r}\left[\frac{\partial n(\mathbf{r},t)}{\partial t} + \nabla\cdot\mathbf{J}(\mathbf{r},t)\right] \tag{3.5}$$

This equation must hold for any volume Ω since we didn't make any specific assumption about Ω. This means that the integrand must be 0 for every possible volume Ω. The equation of continuity 3.1 follows then from this consideration.
The macroscopic thermodynamic mechanism for mass flow is a chemical potential gradient or, equivalently, for a dilute solution, a solute concentration gradient. Hence a reasonable phenomenological relationship is:

$$\mathbf{J}(\mathbf{r},t) = -D\nabla n(\mathbf{r},t) \tag{3.6}$$

Here D is the so called *diffusion coefficient*. It has the dimensions m^2/s and generally depends on particle size, solvent and temperature. Equation 3.6 is called Fick's first law of diffusion.
Combining 3.1 and 3.6 yields:

$$\frac{\partial n(\mathbf{r},t)}{\partial t} = D\nabla^2 n(\mathbf{r},t) \tag{3.7}$$

The last equation is known as Fick's second law of diffusion.
Fick's laws were developed to describe to motion of solute molecules as a consequence of a non-uniform concentration, i.e. a non zero net flux of particle from regions with higher concentration to regions with lower concentration, in order to equalize concentration gradients. It was shown by Einstein in 1905 [13] that the general picture of Fick's law still holds for Brownian motion, where no net concentration gradient is present. In his study it was shown that the random motion of particles suspended in a fluid may be explained by considering the local concentration gradient, which is responsible for the molecular motion on a local scale.

3.1.1 Free self diffusion

Self diffusion is caused by thermal mobility of the molecules in the medium, which collide with each others and do not follow any preferential direction.
When the concentration gradient is zero, there is no net diffusive transport (net flux $\mathbf{J}(\mathbf{r},t) = 0$). However the diffusion process continues as self-diffusion: the solute is only mixed, but there is no net solute displacement from one region to other regions of the fluid. Free self diffusion is often referred to as Brownian motion. The random motion of particles in this case arises from local concentration fluctuations, and not from macroscopic concentration gradients.

Instead of considering the concentration of molecules in a given solution, it is in this case better to use the probabilistic approach [8]. The motion of particles can in fact be described by a displacement probability, that indicates how likely a given molecule is to move from one given position to another one in a given time.
To learn how the self-diffusion constant is related to microscopic dynamics, we now consider the correlation function:

$$c(\mathbf{r},t) = \langle \delta\rho(\mathbf{r},t)\delta\rho(\mathbf{0},0)\rangle \tag{3.8}$$

$c(\mathbf{r},t)$ obeys the same equation as $n(\mathbf{r},t)$, that is:

$$\frac{\partial c(\mathbf{r},t)}{\partial t} = D\nabla^2 c(\mathbf{r},t) \tag{3.9}$$

But note that $\langle \rho(\mathbf{r},t)\rho(\mathbf{0},0)\rangle$ is proportional to $P(\mathbf{r},t)$, which is the conditional probability distribution that a solute particle is at $\mathbf{r}$ at time t given that the particle was at the origin at time zero. As a consequence:

$$\frac{\partial P(\mathbf{r},t)}{\partial t} = D\nabla^2 P(\mathbf{r},t) \tag{3.10}$$

Since $P(\mathbf{r},t)$ and $c(\mathbf{r},t)$ are well defined at the molecular level, these differential equations provide the necessary connection between the self-diffusion constant D and microscopic dynamics. It has to be noted that we could also consider the probability $P(\mathbf{r}|\mathbf{r}',t)$, which is the probability for a given spin to move from $\mathbf{r}$ to $\mathbf{r}'$ in the diffusion time t.
The partial differential equation in 3.10 can be solved given the initial condition $P(\mathbf{r}|\mathbf{r}',0) = \delta(\mathbf{r}'-\mathbf{r})$. This results in a Gaussian profile:

$$P(\mathbf{r}|\mathbf{r}',t) = (4\pi Dt)^{-3/2}\exp\left(-\frac{(\mathbf{r}'-\mathbf{r})^2}{4Dt}\right) \tag{3.11}$$

Let's now consider:

$$\Delta R^2(t) = \langle |\mathbf{r}_1(t) - \mathbf{r}_1(0)|\rangle \tag{3.12}$$

that is the squared displacement of a tagged molecule in a time t.

Clearly:

$$\Delta R^2(t) = \int d\mathbf{r} r^2 P(\mathbf{r},t) \tag{3.13}$$

Thus:

$$\begin{aligned}\frac{d}{dt}\Delta R^2(t) &= \int d\mathbf{r} r^2 \frac{\partial P(\mathbf{r},t)}{\partial t} \\ &= \int d\mathbf{r} r^2 D\nabla^2 P(\mathbf{r},t) \\ &= 6D\int d\mathbf{r} P(\mathbf{r},t)\end{aligned} \tag{3.14}$$

Here the last equality is derived integrating by part twice. Since the probability distribution $P(\mathbf{r},t)$ is normalized for every time t, we have:

$$\Delta R^2(t) = 6Dt \tag{3.15}$$

which is know as *Einstein's equation of diffusion*. We carried out the calculation for the 3D case. More generally, Einstein equation can be rewritten for n dimensional case as:

$$\Delta R^2(t) = 2NDt \tag{3.16}$$

where N represents the dimensionality of the system. This equation is strictly valid only after an initial transient time, which is the time for the inertial regime to relax and the time it takes for the diffusion regime to take over. The thermal motion at the molecular level is really complicated and it has a small characteristic time (typically in the order of picoseconds). On such small timescales we cannot consider the molecular motion as the sum of several statistically independent steps. However, since the typical diffusion time we can probe (i.e. in an MRI experiment) is on the order of milliseconds, we can completely neglect the inertial behavior before the transient time and use the statistical approach previously introduced.
We can state Einstein's equation in a different way: provided that the number of molecules in the area of interest is big (this is required by the Central Limit Theorem), and provided that the molecules are free to diffuse, then the displacement probability functions assumes a gaussian-shape and its variance (the width of the bell-shaped distribution) only depends on the so-called diffusion coefficient and on the observation time (or diffusion time), as indicated by Einstein's equation. Gaussian diffusion profiles in 1 dimension as a function of the diffusion time are shown in figure 3.1.

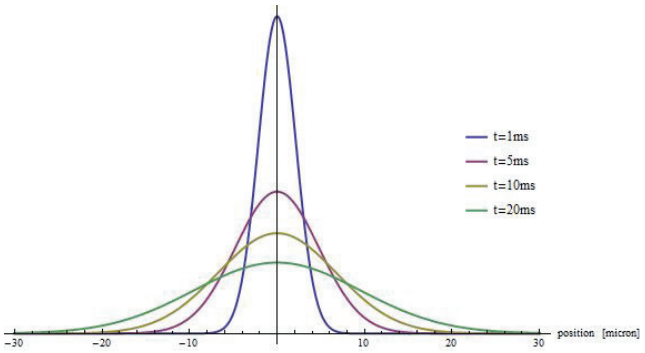

Figure 3.1: Probability density function of displacement in one dimension for different diffusion times in the situation of free diffusion. The diffusion coefficient D was set to $2.272 \times 10^{-9} m^2/s$ (diffusion coefficient of pure water at $25°C$, as reported in [24])

3.1.2 Hindered and restricted diffusion

As already mentioned, diffusion refers to random motion of fluid molecules under the action of thermal energy. This random motion is described by a displacement distribution, and that distribution indicates the probability of finding a particle at a given distance from the starting point if we allow it to move for a given diffusion time t_{diff}. For free diffusion, this distribution has a Gaussian shape. This is found by analytically solving the diffusion equation imposing no geometric boundary conditions (i.e. diffusion barriers). However, when biological tissues are studied, additional boundary conditions have to be included in the description, in order to account for the effect of permeable and semipermeable barriers and geometric microstructure properties of the tissue of interest. Determining the boundary conditions may be extremely complicated, due to the difficulties in modeling the complex interaction between water molecules and barriers and/or obstacles.
As a simple example, we could for instance imagine to enclose the molecule system within an impermeable sphere. The molecules of fluid inside the sphere will tend, if we wait long enough, to occupy all the available space inside the sphere. However we would expect in

this case a lower displacement distance, since the walls of the impermeable sphere do not allow the spins to move further. Since the spins cannot go beyond the sphere walls, the resulting displacement will still show a bell shape, but with well defined maximum values for displacement. This limit case of diffusion is called *restricted diffusion*.
An intermediate situation in between free and restricted diffusion often used in the study of biological tissues is the so called *hindered diffusion*, which refers to effects of high viscosity, presence of macromolecules, semipermeable barriers and various tortuosity effects. In this case we would expect to observe a lower displacement as a function of diffusion time. The resulting displacement probability can then still be approximated with a Gaussian, but with reduced "spread". According to 3.15 the spread of the Gaussian displacement distribution is completely determined by the diffusion coefficient D and the diffusion time interval, so in the situation where an semipermeable sphere is introduced in the medium we would expect a lower diffusion coefficient. This new diffusion coefficient, which depends on the physical and geometrical properties of the system in which self diffusion takes place, is usually indicated as *Apparent Diffusion Coefficient* (ADC), in order to discriminate it from the "true" diffusion coefficient D that characterizes free self diffusion.
The nature of the diffusion processes is strongly determined not only by the properties of the compartment in which it takes place, but also by other interconnected parameters. Between them, the diffusion time is one of the most important. The effect of diffusion time in the nature of diffusion processes is intuitively shown in figure 3.2. As can be seen, the shape of the Gaussian profile of the displacement distribution strongly depends on the diffusion time. With increasing time in fact we would expect from equation 3.11 the height of the distribution to decrease and to become broader. In the case of restricted diffusion, the displacement distribution will be constrained by a minimum and maximum value for long diffusion times, reaching a constant profile for diffusion times becoming much longer than the characteristic time scale of the system under consideration. However, if the diffusion time is too short compared to the length scale of the restriction, the displacement probability with and without restriction will look the same, since particles will practically never experience the effect of boundaries.

Another way of looking at the three phenomenological description of diffusion intro-

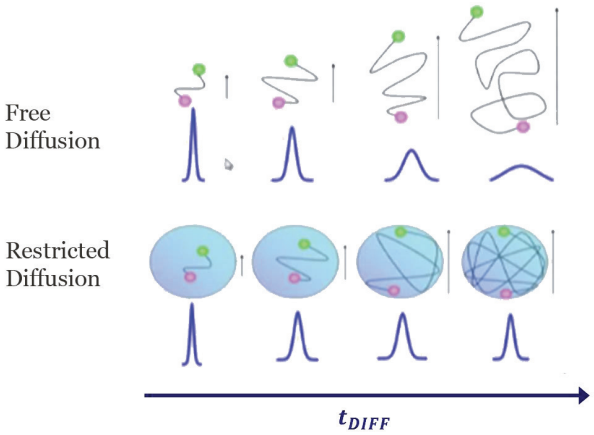

Figure 3.2: Schematic representation of diffusion displacement for free and restricted diffusion and corresponding displacement distribution. The images are ordered from left to right for increasing diffusion time.

duced is performing the so called "restriction-test", which consists of plotting the mean

displacement calculated by using Einstein's equation as a function of the square root of diffusion time (see figure 3.3). If the correlation is linear, we are in the regime or free or hindered diffusion, and the true (or apparent) diffusion coefficient can be determined by the slope of the line. On the other hand, when the diffusion is restricted, two different regimes are normally expected: for short diffusion times the mean displacement is still proportional to the square root of time, since the system is in the regime of free diffusion, while for increased diffusion time a plateau value is expected for the mean displacement, reflecting the presence of impermeable boundaries.

In order to explain the interaction of water molecules with obstacles such as macro-

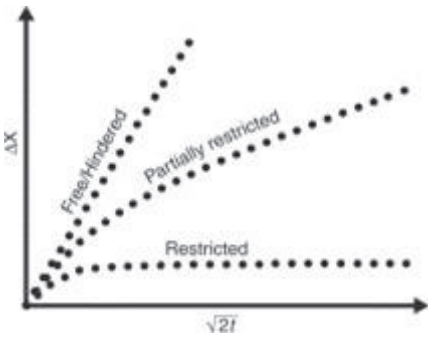

Figure 3.3: The three possible diffusion processes that can occur in biological tissues: free, hindered, and restricted. While free and hindered diffusion will show a linear relation between the mean displacement and square root of the diffusion time, partially restricted (or highly hindered) and restricted diffusion will show non-linear dependency.

molecules, which results in hindered diffusion, the concept of *tortuosity* was borrowed from solid porous media. Due to presence of obstacles, water molecules cannot travel straight, but must travel longer paths to cover a given distance. This results in an apparent decrease of the diffusion coefficient, according to:

$$ADC = \frac{D}{\lambda^2} \tag{3.17}$$

where D would be the diffusion coefficient observed in the absence of obstacles, and λ is the dimensionless tortuosity coefficient.

It is not well understood yet which are the causes of restricted/hindered diffusion in cardiac muscles, since there hasn't been any true attempt to model the diffusion process in this tissue. A schematic drawing of different diffusion processes that may take place in the heart is shown in figure 3.4 as an example.

So far we only discussed situations in which diffusion is isotropic. However if the shape of the object in which diffusion occurs is not spherical or if more obstacles are present in one direction than in another one, an anisotropic diffusivity behavior is to be expected. In this case the water in the structures will not move equally in every direction, but will have a preferential pathway. The most intuitive way of representing this kind of diffusion is an ellipsoid more or less elongated according to the degree of anisotropy. The ellipsoid formalism will be introduced in section 3.3 in connection with the diffusion eigenvectors derived from Diffusion Tensor Imaging.

MRI techniques are available to measure hindered and restricted diffusion without the need of any tracer or exogenous agent. These techniques are called Diffusion Weighted MRI (DW-MRI) and allow the visualization and quantification of the diffusion characteristics. The theoretical background of DW-MRI, together with its practical implementation

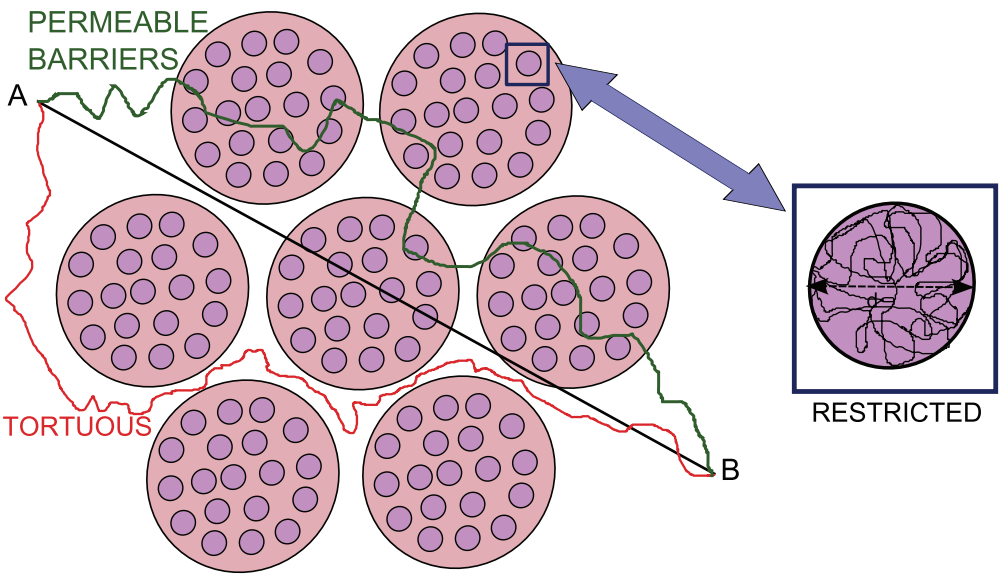

Figure 3.4: Possible effects of compartmentalization and presence of microstructures in the diffusion behavior of water in cardiac tissue.

in an MRI scanner, will be introduced in section 3.2.
In general, during the diffusion time of a DW experiment, water molecules in the tissue of interest will undergo a certain displacement, on a scale similar to the size of the cellular structure in that area. DW-MRI can then be used to probe the microstructure of the tissue and to get information about microstructures shape and orientation.
In general in biological tissues it is not possible to assume *a priori* a Gaussian profile for the diffusion and so Einstein's equation may not hold. In such tissues the diffusion may be *restricted*. The mean displacement in this case may depend on the presence of obstacles, on the diffusion time and in general on how the diffusion is measured, as already discussed. The Apparent Diffusion Coefficient is still used in this case, but a connection between it and the structure of the tissue is not easily made

3.2 Diffusion Weighted MRI

Diffusion can be detected using DW-MRI. The diffusion encoding requires two gradients to be added in a sequence to first dephase and then rephase the spins in a given region. If diffusion processes take place in that region, the rephasing will not be complete, leading to a measurable signal attenuation. In this section the Stejskal-Tanner sequence, which was the first DW-MRI experiment, will be introduced, together with the formula used to quantify the diffusion coefficient or ADC from the results, in the assumption of Gaussian profile for the diffusion. After that, the practical implementation and application of DW-MRI will be discussed.

3.2.1 Stejskal-Tanner sequence

The first diffusion weighted sequence was used by Stejskal and Tanner in 1965 [53]. This original sequence was a standard Spin-Echo sequence, with 90° and 180° RF pulses, where

two diffusion gradients with the same strength G and duration δ were applied following the 90°, symmetrically placed around the 180° pulse, with a temporal spacing between them given by Δ. This results in a magnetic labeling of the spin transverse magnetization as a function of their position. A schematic drawing of that sequence is shown in figure 3.5. This sequence is often referred to as PGSE (Pulsed Gradient Spin Echo).

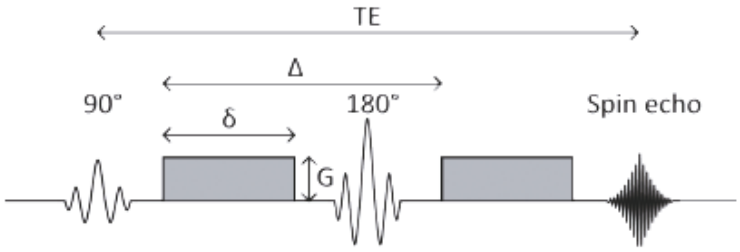

Figure 3.5: Schematic drawing of the Pulsed gradient sequence proposed by Stejskal and Tanner [53]. Two rectangular gradients (G) of equal size are placed on both sides of a 180° refocusing pulse. The parameters of the sequence are: TE = echo time, δ = duration of the pulse gradients, Δ = spatial separation between the starting point of the two gradients, G = pulse gradient magnitude. Reproduced from [16].

3.2.2 Diffusion encoding

Almost any MRI pulse sequence can be modified to become sensitive to diffusion of water molecules. One of the most used is the so called Spin Echo DW, where two diffusion sensitizing gradients are incorporated in a standard spin echo sequence. This allows to magnetically label the spins transverse magnetization as a function of their position. After the first 90° pulse the spins precess in the xy plane with frequency equal to Larmor frequency. After the phase and frequency encoding, the first diffusion gradient is applied. The application of a single encoding causes the different spins to dephase, and such dephasing is proportional to the average position of the spin during the time interval δ in which the gradient itself is applied. We can then consider the application of the first diffusion encoding gradient as a labeling of the spins according to their position along the direction of the applied gradient. After the labeling, a 180° pulse is applied, that causes the spins to rotate on the other half of the xy-plane. A second diffusion encoding gradient, identical to the first one, is then applied after the 180° pulse, in order to compensate for the first one and force the spins to rephase.
If we look at individual spins, assuming that the PFG are applied along the z-direction, the first diffusion encoding gradients introduces a phase shift ϕ_1, and the second one a phase shift ϕ_2 given by:

$$\begin{aligned} \phi_1 &= \gamma \int_0^{\gamma} G z_1 dt = \gamma G \delta z_1 \\ \phi_2 &= \gamma \int_{\Delta}^{\Delta+\delta} G z_2 dt = \gamma G \delta z_2 \end{aligned} \tag{3.18}$$

The net phase difference is then given by:

$$\phi_2 - \phi_1 = \gamma G \delta (z_2 - z_1) \tag{3.19}$$

For static spins ($z_2 = z_1$), the rephasing after the second gradient is complete, yielding a maximum echo signal intensity. However, if spins have moved during the separation time

Δ, the magnetic field experienced during the application of the first gradient would be different from the one experienced during the application of the second one, leading to a non zero phase dispersion. The resulting phase dispersion will cause signal loss in the diffusion weighted image (3.6). When diffusion is present in the area of interest then, the resulting signal after the pair of diffusion encoding gradients will be attenuated exponentially according to the Stejskal and Tanner formula

As already mentioned, other acquisition sequences derived from the standard spin echo

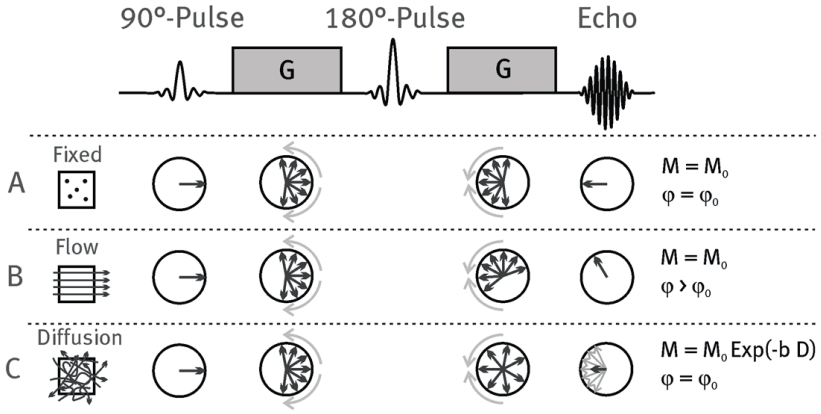

Figure 3.6: Schematic representation of dephasing for spins in a single voxel under the influence of a standard Stejskal-Tanner sequence. M_0 and ϕ_0 are respectively the net magnetization vector and the phase of magnetization at equilibrium, while M and ϕ are the corresponding values after the pair of diffusion gradients is applied. **A**) For fixed spins the dephasing due to the application of the first gradient is completely rephased after the second gradient, resulting in no difference in phase and net magnetization (signal is not attenuated) **B**) For flowing spins the dephasing due to the first gradient will not be completely rephased, since the spins are displaced during the interval between the gradients. Since the displacement due to flow will be the same for all the spins in a voxel, this will result in a net phase shift, but no difference in the magnetization value. **C**) For diffusing spins there is no preferential direction, since they move randomly. Thus each individual spin will experience a different dephasing and rephasing, leading to a zero phase shift but a measurable decrease in net magnetization. Reproduced from [16].

diffusion sequence can be used to encode diffusion. Most of them are based on the Pulsed Field Gradient technique introduced by Stejskal and Tanner. Since for Diffusion Imaging in general a lot of image acquisitions are required, often there is a need for faster acquisition techniques. This is especially valid for *in vivo* experiments, since the standard DW spin echo sequence is really slow. One of the most widely used fast diffusion sequences is PG-EPI (Pulsed Gradient Echo Planar Imaging). A schematic drawing of this sequence is shown in figure 3.7.

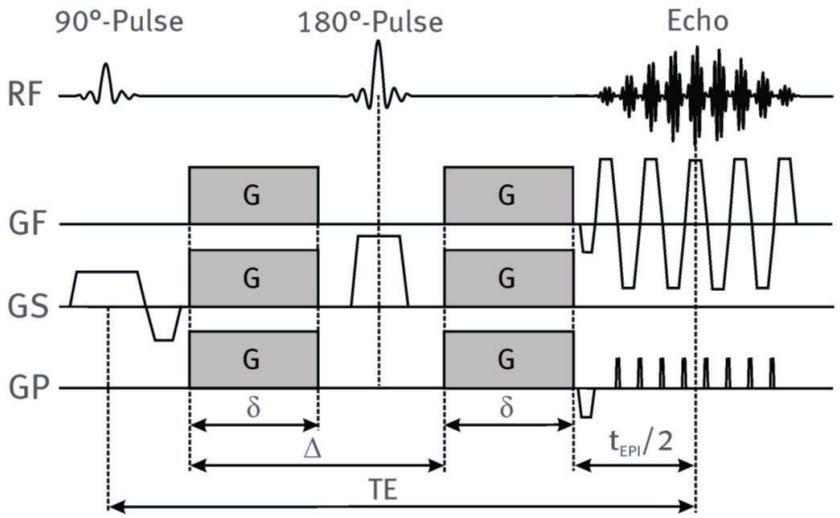

Figure 3.7: Single-shot diffusion-weighted spin echo echo planar imaging (EPI) pulse sequence. The entire k-space is filled with a single EPI readout train, resulting in a fast acquisition. Reproduced from [16].

The acquisition with the single shot echo planar imaging shown in figure 3.7 is often problematic, since the technique is really sensitive to B_0 susceptibility effects and prone to eddy currents induced distortions, in particular for high magnetic field. Moreover the T_2* signal decay during the echo train limits the spatial resolution achievable and often introduces severe blurring in the resulting images. Another issues relative to Single Shot EPI in the Diffusion imaging framework is the poor SNR caused by the long echo train required. The Diffusion Sensitizing module in fact introduces constraints about the minimal achievable echo time and this results in a medium to strong T_2 weighting of the images in the sequence. Considering the typically short characteristic T_2 time typical of muscle tissue (in the order of 30 ms at 9.4 T, which may be further decreased by fixation), the minimal echo time of a single shot EPI may strongly limit the signal in the images. In order to shorten the echo train, often EPI with segmented k-space is required. Multishot EPI is sometimes problematic for *in vivo* experiments, since the phase shifts induced by motion needs to be coherent for different segments and robust phase navigation techniques are required. Furthermore, a multi-shot EPI technique obviously requires a longer acquisition time with respect to standard single shot EPI, but if acquisition time is not an issue, as it is the case for *ex vivo* experiments, it is often preferred over single shot. In fact it is much less sensitive to susceptibility artifacts and provides a better SNR, which is usually one of the main issues in Diffusion Imaging.
In some circumstances it is useful to investigate the different diffusion behaviors as a function of diffusion time. If a standard Pulsed Field Gradients encoding sequence is used, an increase in the gradient spacing will necessary result in an increase in the minimum achievable echo-time, and consequently in a lower SNR. This sets then a practical limit to the diffusion times that can be used if the characteristic T_2 time of the tissue is short. A possible solution to this issue is the use of a Stimulated Echo sequences (STEAM). In this case the magnetization decays with T_1, which is typically much longer than T_2, allowing one to read the data out for a longer time. A disadvantage of this method is that

50% of the signal is lost. A number of simulations have been carried out in literature to determine for which sets of diffusion times the decrease in the minimum echo time can overcome the lost of signal when STEAM is used. The conclusion is that STEAM offers advantages over PFG sequence only in the case of tissues with typical T_2 below 25 ms (such as muscle). [56].

Stejskal-Tanner formula for signal attenuation

Diffusion processes in the liquid state are governed by the Bloch-Torrey equation, derived by Torrey in 1965 adding the diffusion terms to the traditional Bloch equation for magnetization [60]:

$$\frac{\partial M_+}{\partial t} = -i\omega_0 M_+ - i\gamma \mathbf{r} \cdot \mathbf{G} m_+ - \frac{M_+}{T_2} + D\nabla^2 M_+ \tag{3.20}$$

Here $M_+ = M_x + iM_y$ is the complex representation of the transverse magnetization, $\mathbf{r}$ represents the position vector, $\mathbf{G}$ is the magnetic field gradient (diffusion encoding gradient) and D is the apparent diffusion coefficient. This equation can be solved for a spin echo experiment giving as a result the well known Stejskal-Tanner formula for signal attenuation caused by diffusing spins:

$$\frac{S(G)}{S(0)} = \exp\left(-\gamma^2\delta^2G^2\left(\Delta - \frac{\delta}{3}\right)D\right) \tag{3.21}$$

where $S(0)$ is the signal obtained when no diffusion gradient is applied and $S(g)$ is the attenuated signal. A complete derivation of formula 3.21 can be found in [34].
The previous formula is usually written as:

$$\frac{S(G)}{S(0)} = \exp(-bD) \tag{3.22}$$

where $b = \gamma^2\delta^2G^2(\Delta - \delta/3)$ is called b-value and is a parameter depending on the protocol used for acquiring the diffusion weighted images. This diffusion weighting factor was first introduced by Le Bihan in 1986 [37].
Equation 3.22 is intrinsically monodimensional, since the original experiment was only able to sample the diffusion along one direction, given by the direction of the applied pair of diffusion encoding gradients.
Furthermore in the original derivation, rectangular-shaped pulses were used. This shape is not achievable in real scanners, since the gradient pulse cannot rise instantaneously from zero to its maximum value. The previous equation was corrected by [41] taking into account the non zero pulse ramp time ϵ:

$$S(G) = \exp\{-\gamma^2G^2d\delta^2[(\Delta - \delta/3) + \epsilon^3/30 - \delta\epsilon^2/6]\} \tag{3.23}$$

3.2.3 PGSE in the narrow pulse approximation

In the narrow-pulse approximation it is assumed that the duration of the two diffusion encoding gradients is much smaller than the spacing between them (i.e. $\delta << \Delta$). In this particular situation the motion of diffusing spins over the time δ can be neglected and the two gradients can be mathematically considered as two delta functions. This situation of course cannot be obtained in practice, where often the duration of the diffusion encoding gradients is in the same order of magnitude of the temporal spacing between

them. However it is interesting to study the narrow pulse approximation since it allows to show some really important mathematical relationship between the measured signal and the Probability Density Function (PDF) already introduced in the previous sections. After the first gradient pulse, a spin located at position $\mathbf{r}$ at the instant of the pulse will experience a phase shift equal to $\gamma\delta\mathbf{g}\cdot\mathbf{r}$. If during the diffusion time the labeled spin will move to position $\mathbf{r}'$, the net phase shift following the second diffusion encoding gradient will be $\gamma\delta\mathbf{g}\cdot(\mathbf{r}'-\mathbf{r})$.
If we define $E(\mathbf{g},\Delta)$ as the normalized signal at the echo center, we can write the total signal as an ensemble average of the different phase terms $\exp[i\gamma\delta\mathbf{g}\cdot(\mathbf{r}'-\mathbf{r})]$, each one weighted by the probability for a given spin to begin at position $\mathbf{r}$ and end at position $\mathbf{r}'$. This probability is given by the product of $P(\mathbf{r})$ and $P(\mathbf{r}|\mathbf{r}',t)$. They are respectively the probability for a given spin to start at position $\mathbf{r}$ and the conditional probability to move from $\mathbf{r}$ to $\mathbf{r}'$ after time t. The term $E(\mathbf{g},\Delta)$ is also called signal attenuation, and represents the ratio between the signal measured in a sequence made sensitive to diffusion and the same signal we would measure without diffusion encoding. Following the above mentioned considerations, this signal attenuation can be written as:

$$E(\mathbf{g},\Delta)=\int P(\mathbf{r})\int P(\mathbf{r}|\mathbf{r}',\Delta)\exp(-\gamma\delta\mathbf{g}\cdot[\mathbf{r}'-\mathbf{r}])d\mathbf{r}'d\mathbf{r} \tag{3.24}$$

It has to be noted here that this explicit formulation for the echo signal attenuation is strictly valid only under the narrow pulse approximation. However in practice it has been observed that introducing a non-negligible δ generally preserves the large-scale structure and orientation of the inferred PDF [43].
At this point we can define the dynamic displacement $\mathbf{R}=\mathbf{r}'-\mathbf{r}$ and define $\overline{P}(\mathbf{R},t)$ as the probability that a spin will undergo a displacement $\mathbf{R}$ over a time interval t. This distribution can be found by summing the contributions over all the possible start positions (which means integrating over the all voxel volume) and using the substitution $\mathbf{r}'=\mathbf{r}+\mathbf{R}$.

$$\overline{P}(\mathbf{R},t)=\int P(\mathbf{r})P(\mathbf{r}|\mathbf{r}+\mathbf{R},t)d\mathbf{r} \tag{3.25}$$

Equation 3.24 can then be rewritten as:

$$E(\mathbf{g},\Delta)=\int \overline{P}(\mathbf{R},t)\exp(-\gamma\delta\mathbf{g}\cdot\mathbf{R})d\mathbf{R} \tag{3.26}$$

which is clearly a Fourier transform. We found then a fundamental relationship: the signal attenuation $E(\mathbf{g},\Delta)$ and $\overline{P}(\mathbf{R},t)$, the Probability Density Function of travelling a given distance $\mathbf{R}$ in the diffusion time t, are related to each others via a Fourier transform. This fact has really important implications for Diffusion Weighted MRI.
It has to be noted here that if we insert the probability density function of free diffusion (equation 3.11) into equation 3.26, we find the well known Stejskal and Tanner equation, used for DTI. It has to be clear then that the formula is strictly valid only under the assumption of gaussian diffusion.

3.3 Diffusion Tensor Imaging

Although probing diffusion along a single direction can provide insight into many pathological conditions, this lacks information about directionality of diffusion. As already explained, we expect diffusion to be anisotropic in biological tissues, and in order to probe directionality, a 3D approach has to be used. The way this is done in practice is

by applying the diffusion encoding sequence along different non collinear directions.
In the case of an isotropic medium, the factor D present in the Stejskal and Tanner formula (3.22) is a scalar, since it does not depend on the direction along which diffusion is measured. However, in an anisotropic situation, like for instance in many biological tissues, the direction of measurement has to be taken into account. In this case the diffusion term can be replaced by a rank-2 tensor (a 3×3 matrix). The previous formula then becomes:

$$\frac{S(g)}{S(0)} = \exp(-b\mathbf{g}^T \underline{\underline{\mathbf{D}}}\mathbf{g}) \tag{3.27}$$

Here $\mathbf{D}$ is the so called *Diffusion Tensor*. This 3×3 matrix assumes the form:

$$\begin{pmatrix} D_{xx} & D_{xy} & D_{xz} \\ D_{yx} & D_{yy} & D_{yz} \\ D_{zx} & D_{zy} & D_{zz} \end{pmatrix}$$

The diagonal components D_{xx}, D_{yy} and D_{zz} represent the diffusion along three mutually orthogonal directions corresponding to the three axes of the magnet. The off-diagonal terms represent the correlation between these 3 orthogonal directions. With the introduction of the diffusion tensor formalism, equation 3.10 can be rewritten as:

$$\frac{\partial P(\mathbf{r}, t)}{\partial t} = \nabla \cdot [\underline{\underline{\mathbf{D}}} \nabla P(\mathbf{r}, t)] \tag{3.28}$$

P again represents the conditional probability distribution that a solute particle is at r at time t given that the particle was at the origin at time zero.
From physical consideration it is easy to understand that this tensor has to be symmetric ($D_{ij} = D_{ji}$), since the probability that a given molecule will move in the positive axis is equivalent to the probability of a displacement in the opposite direction.
When diffusion is isotropic, the diagonal components of the tensor are the same ($D_{xx} = D_{yy} = D_{zz} = ADC$) and the tensor assumes a diagonal form.
On the other hand, when diffusion is anisotropic, the diagonal components are in general different from each others and non zero off-diagonal terms are present. However, it can be proven that for every positive definite tensor, an orthogonal system can be defined where the tensor itself assumes a diagonal form, with all the off-diagonal terms equal to zero and the diagonal terms positive. The mathematical operation of finding this frame of reference is called diagonalization. The diagonal elements in this new system are called eigenvalues and denoted by λ_1, λ_2 and λ_3 and the principal diffusion directions are the corresponding eigenvectors $\mathbf{e}_1$, $\mathbf{e}_2$ and $\mathbf{e}_3$.

$$\begin{aligned} \underline{\underline{\mathbf{DE}}} = \underline{\underline{\mathbf{EA}}} \quad \text{where} \quad \underline{\mathbf{E}} &= (\mathbf{e}_1|\mathbf{e}_2|\mathbf{e}_3) \\ \underline{\mathbf{A}} &= \begin{vmatrix} \lambda_1 & 0 & 0 \\ 0 & \lambda_2 & 0 \\ 0 & 0 & \lambda_3 \end{vmatrix} \end{aligned} \tag{3.29}$$

A common way of representing the diffusion tensor is the diffusion ellipsoid formalism. An example of these diffusion ellipsoids for free and restricted diffusion is shown in 3.8. The term "restricted diffusion" is often used in the context of DTI as a synonym of hindered diffusion, but while the diffusion parameters are influenced by both restricted and hindered diffusion, the tensor model assumed Gassianity of the diffusion profile, so it shouldn't theoretically be used when the diffusion is purely restricted. The term restricted will still be used in some occasions in this thesis, but the reader must keep in mind that

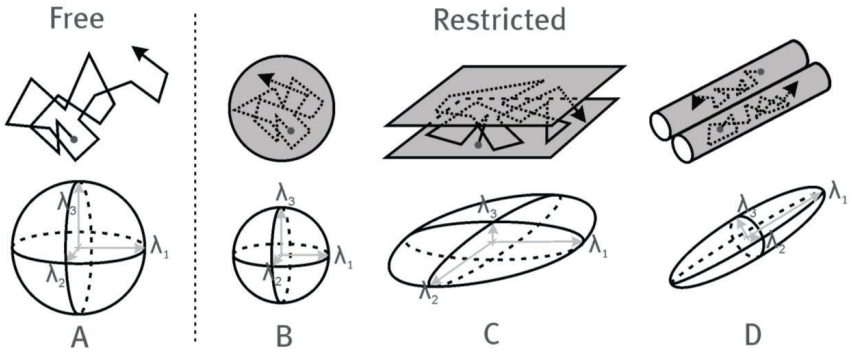

Figure 3.8: Schematic representation of free and restricted diffusion. Here the arrows represent the 3 eigenvectors ($\mathbf{e}_1$, $\mathbf{e}_2$ and $\mathbf{e}_3$), which indicate the directions of the principal axes of diffusion in a voxel, and the corresponding eigenvalues (λ_1, λ_2 and λ_2) the magnitude of the apparent diffusion coefficients along these principal axes. (A) Free isotropic diffusion, equal probability of displacement in all directions, represented by a sphere ($\lambda_1 = \lambda_2 = \lambda_3$). (B) Isotropic hindered diffusion, equal probability of displacement in all directions, represented by a smaller sphere ($\lambda_1 = \lambda_2 = \lambda_3$). (C) Anisotropic diffusion, hindered in one direction, represented by a disc ($\lambda_1 \sim \lambda_2 >> \lambda_3$). (D) Anisotropic diffusion, hindered in two directions, represented by an ellipsoid ($\lambda_1 >> \lambda_2 \sim \lambda_3$).

when it refers to the tensor model, then restricted translates into hindered diffusion.

The eigenvectors represent the principal axes of diffusion and the corresponding eigenvalues the (square of the) magnitude of the diffusion coefficients along these directions. To relate this graphical representation to the physics of diffusion, we can state the previous concepts in a different way: the radius at any given point of the diffusion ellipsoid relates to the probability of water molecules to diffuse along that direction (PDF). Since for many applications (i.e. fiber tractography) only the principal direction of diffusion, which represents the principal axis of the fiber, is of interest, the PDF is radially integrated to give the so called Orientation Distribution Function (ODF). This function only contains information about the average principal diffusion direction in the voxel.

3.3.1 Obtaining the diffusion tensor from MR signal

In order to obtain the diffusion tensor $\underline{\mathbf{D}}$, we need at least 7 measurements: 1 unweighted measurement (S_0) and 6 weighted measurements S_i, (i=1,....,n) with gradients $g_i = (x_i, y_i, z_i)$ applied in 6 different directions. The six components of the diffusion tensor can be calculated using the following relation:

$$\begin{pmatrix} D_{xx} \\ D_{yy} \\ D_{zz} \\ D_{xy} \\ D_{yz} \\ D_{xz} \end{pmatrix} = \begin{pmatrix} x_1^2 & y_1^2 & z_1^2 & 2x_1y_1 & 2y_1z_1 & 2x_1z_1 \\ \vdots & \vdots & \vdots & \vdots & \vdots & \vdots \\ x_i^2 & y_i^2 & z_i^2 & 2x_iy_i & 2y_iz_i & 2x_iz_i \\ \vdots & \vdots & \vdots & \vdots & \vdots & \vdots \\ x_n^2 & y_n^2 & z_n^2 & 2x_ny_n & 2y_nz_n & x_nz_n \end{pmatrix}^{-1} \begin{pmatrix} -\frac{1}{b_1} ln \frac{S_1}{S_0} \\ \vdots \\ -\frac{1}{b_i} ln \frac{S_i}{S_0} \\ \vdots \\ -\frac{1}{b_n} ln \frac{S_n}{S_0} \end{pmatrix}$$

Often in practice more than 6 diffusion encoding directions are used in order to increase the quality of the data. In this case the previous relationship cannot be used because the

matrix containing the diffusion parameters is not a square matrix and then cannot be inverted. There are several methods for calculating the so called pseudoinverse matrix, which allows to fit the acquired data to a rank-two tensor with 6 degrees of freedom. The most common are LLS (Linear Least Squares), WLLS (Weighted Linear Least Squares), and NLLS (Non linear Least Squares) with their constrained counterparts, which force the diffusion tensor to be positive definite. Recently also the RESTORE (Robust Estimation of Tensors by Outlier Rejection) approach has been presented in literature. A detailed description of these fitting methods is beyond the scope of this thesis. A literature review about this topic can be found in [30],[9],[17].

3.3.2 Scalar parameters from the diffusion tensor

Since the data obtained from DTI are difficult to interpret, some additional parameters were introduced to quantitatively analyze and visualize the data[5]. Some of the more common scalar parameters derived from DTI are the apparent diffusion coefficient (ADC), the fractional anisotropy (FA) and the mode of anisotropy and they are invariant under rotation and scaling.
The ADC indicates the mean diffusion in a voxel and is expressed in units of mm^2/s. In literature the ADC is often referred to as mean diffusivity.

$$ADC = \frac{trace\underline{\underline{\mathbf{D}}}}{3} = \frac{D_{xx} + D_{yy} + D_{zz}}{3} = \frac{\lambda_1 + \lambda_2 + \lambda_3}{3} \tag{3.30}$$

A second scalar measure is the fractional anisotropy, that indicates how much the profile of diffusion deviates from the isotropic case, or how much the diffusion ellipsoid deviates from a spherical shape. It is adimensional and its value is comprised between 0 (isotropic case) and 1 (completely anisotropic).

$$FA = \frac{1}{2}\sqrt{2}\sqrt{\frac{(\lambda_1 - \lambda_2)^2 + (\lambda_2 - \lambda_3)^2 + (\lambda_1 - \lambda_3)^2}{(\lambda_1)^2 + (\lambda_2)^2 + (\lambda_3)^2}} \tag{3.31}$$

Another parameter often used in DTI is the mode of anisotropy. It is defined as:

$$mode(\underline{\underline{\mathbf{D}}}) = 3\sqrt{6}det\left(\frac{\underline{\underline{\mathbf{D}}}}{norm(\underline{\underline{\mathbf{D}}})}\right) \tag{3.32}$$

The anisotropy mode is defined over the interval [-1,+1] and provides complementary information to FA. A value of -1 indicates a planar anisotropic tensor ($\lambda_1 \sim \lambda_2 >> \lambda_3$), 0 indicates an orthotropic tensor, 1 indicates a linear anisotropic tensor ($\lambda_1 >> \lambda_2 \sim \lambda_3$). Orthotropic tensors indicate a diffusive state in between linear and planar anisotropy wherein the three eigenvalues are distinct. A graphic illustration of the glyphs for a single voxel characterized by different fractional anisotropies and anisotropy modes is shown in figure 3.9.

Although derived from the DTI model, the mode of anisotropy is often used as an indicator of complex fiber organization, since a planar glyph geometry is expected is the presence of crossing fibers.

3.3.3 Fiber tractography

Fiber tractography refers to the ensemble of techniques to identify fiber pathways in a given tissue. Tractography is of fundamental importance in the study of fibers, since it

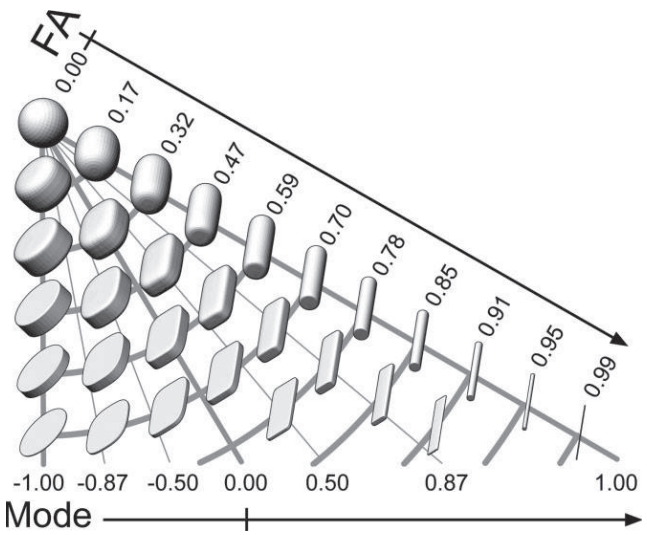

Figure 3.9: Graphical illustration of a diffusion tensor with constant norm represented with superquadratic glyphs for different values of fractional anisotropy and mode of anisotropy. Glyphs are shown for increasing FA (from top to bottom) and increasing mode (from left to right). Glyphs along constant radii are of constant fractional anisotropy, but of varying mode. This figure explicitly demonstrates that increases in FA do not necessarily indicate increasing linear anisotropy. Reproduced from [14]

is the only available tool to asses their structure and the way they are connected *in vivo* and in a non-invasive way.

The fundamental assumption of fiber tractography is that the tangent to the curve representing the fiber tract is always and everywhere parallel to the local peaks of the orientation density function (ODF) estimated from the data for that given point. The concept of ODF will be explained in details in the next chapter. In the case of DTI, however, the ODF peak is simply given by the direction of the main eigenvector (λ_1). Since the ODF is relative to a single voxel, the level of information is discretized. If continuous tract trajectory need to be estimated from the discrete ODF, then interpolation is required. Different algorithms have been presented in literature on they way the tract can be interpolated from the ODF. The two main categories of algorithms for tractography are probabilistic and deterministic .

In addition to the algorithm used, other assumptions play an important role in the way the tracts are drawn and stopped. At each stage of the iteration process, in fact, a certain number of assumption is made about the nature of the tract. Typical example of these additional assumptions are maximum curvature along the tract, maximum and minimum length and ODF peak threshold. They usually provide "stopping criteria" that don't allow the tracks to be calculated further if one of the given conditions is not met. In the case of DTI a stopping criteria based on the value of fractional anisotropy is often used. The need of providing additional parameters for the fiber tracking, requires then in general some arbitrary assumptions or a previous knowledge of tissue structure coming from imaging modalities different from DW-MRI (i.e. dissection, microscopy, histological studies, etc).

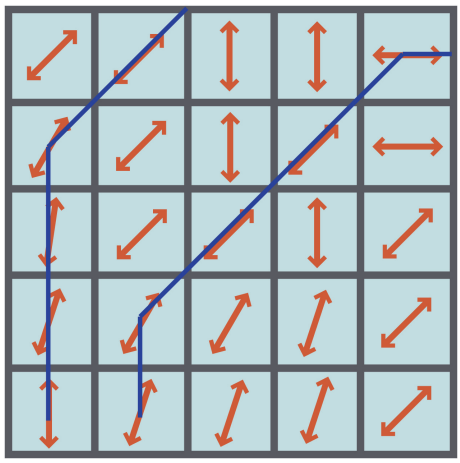

Figure 3.10: Principle of fiber tracking in 2 dimensions. The average orientation is represented for every voxel by the red arrows. The blue lines represent the fiber tracts estimated from the diffusion tensor.

3.4 DTI of the heart

Diffusion Tensor MRI has been validated as a valuable tool for rapid and non destructive analysis of the 3D myocardial structure in both normal and diseased hearts.
The primary diffusion tensor eigenvector has been directly correlated to the myocardial fiber orientation [26]. Furthermore there are some evidences that the fiber tracts form laminar sheets, and the second and third eigenvectors of the diffusion tensor have been shown to relate to the sheet direction and sheet normal direction [63][23][50].
A recent study from Kung et al. [35] showed that DTI can be used to infer the existence of two different populations of myolaminae of different orientation. By measuring the myolaminae orientations from the secondary and tertiary eigenvectors, two different angles were observed, which related to the two different orientations of myolaminae in the left ventricle. These angle showed good correspondence to each of the two myolaminae orientations observed in histology. The histological study showed that these myolaminae exist throughout the all LV, although the number of observation of double sheet population was higher in the region between the midwall and the endocardium. In this area the different myofibers population appeared to be crossing each others with an angle of approximately 90°.
It has been shown that myofibers in the subendocardium have a positive (or right-handed helix), those in the mid-myocardium are circumferential and those in the subepicardium have a negative (or left-handed helix). The transmural helix angle typically ranges from $-60°$ at the epicardium to $+60°$ at the endocardium with a smooth angular variation [22].
DTI has been often used also to study the remodeling of infarcted myocardium in different species, such as pigs [69], mice [54] and human, sheeps and rats [42] *ex vivo*. The remodeling involves both structural and functional changes and they have been shown to occur in both infarcted myocardium and adjacent and remote zone.
Some parameters for cardiac muscle derived from DTI, such as eigenvalues, mean diffusivity and fractional anisotropy are indicated in table 3.1. However, care has to be taken if one wants to compare different data, since they are not strictly a property of tissues, but also have a dependence on the acquisition parameters, such as SNR of the B_0 image,

Table 3.1: DTI-derived parameters for cardiac muscles reported in literature.

Reference	$\lambda_1 \times 10^{-3} mm^2/s$	$\lambda_2 \times 10^{-3} mm^2/s$	$\lambda_3 \times 10^{-3} mm^2/s$	ADC $\times 10^{-3} mm^2/s$	FA
[29] [a]	0.75 ± 0.13	0.60 ± 0.13	0.51 ± 0.13	0.62	0.19
[23] [b]	1.05	0.55	0.45	0.68	0.44
[?] [c]	1.70	1.25	0.95	1.30	0.28
[71] [d]				$0.92 \pm 0.05/0.81 \pm 0.05$	$0.25 \pm 0.01/0.27 \pm 0.01$
[71] [e]				$0.74 \pm 0.03/0.67 \pm 0.03$	$0.27 \pm 0.01/0.29 \pm 0.01$
[69] [f]	1.20 ± 0.15	1.0 ± 0.14	0.82 ± 0.13	1.00 ± 0.14	0.20 ± 0.03
[69] [g]	0.92 ± 0.19	0.62 ± 0.10	0.48 ± 0.09	0.67 ± 0.01	0.32 ± 0.01
[54] [h]	1.03 ± 0.03	0.70 ± 0.02	0.46 ± 0.03	0.70 ± 0.03	0.39 ± 0.02
[54] [i]	0.78 ± 0.05	0.55 ± 0.05	0.36 ± 0.02	0.56 ± 0.02	0.38 ± 0.02
[54] [j]	1.06 ± 0.01	0.70 ± 0.06	0.38 ± 0.04	0.71 ± 0.06	0.48 ± 0.04
[70] [k]	1.78 ± 0.06	0.67 ± 0.05	0.53 ± 0.07		0.33 ± 0.02

[a] Formalin fixed mouse heart
[b] Formalin fixed canine hearts. Values estimated from graphs
[c] Perfused arrested rabbit hearts. Values estimated from graphs
[d] 17 patients with recent myocardial infarction (infarct zone/remote zone)
[e] 17 patients with chronic myocardial infarction (infarct zone/remote zone)
[f] Formalin fixed porcine hearts (infarcted region)
[g] Formalin fixed porcine hearts (infarcted region)
[h] Formalin fixed mouse heart (control)
[i] Formalin fixed mouse heart (7 days after myocardial infarction)
[j] Formalin fixed mouse heart (28 days after myocardial infarction)
[k] Formalin fixed canine heart

number of diffusion encoding directions in the acquisition scheme, and b-values used [16]. The scalar anisotropy indices have mostly been assumed to be uniform throughout the cardiac wall, and often the values are presented in literature as an average over the entire wall. However some studies suggest that they have a transmural heterogeneity. In the work of Jiang et al. [29] it is shown that the fractional anisotropy in the sheep myocardium has a constant value from the epicardium to the midwall, but decreases from the midwall (region where the fibers run circumferentially) to the epicardium (see figure 3.11). This heterogeneous behavior can be caused by different diffusion properties at the microscale, such as different water fraction, and could also suggest the presence of multiple fiber population in the region going from the midwall to the endocardium.

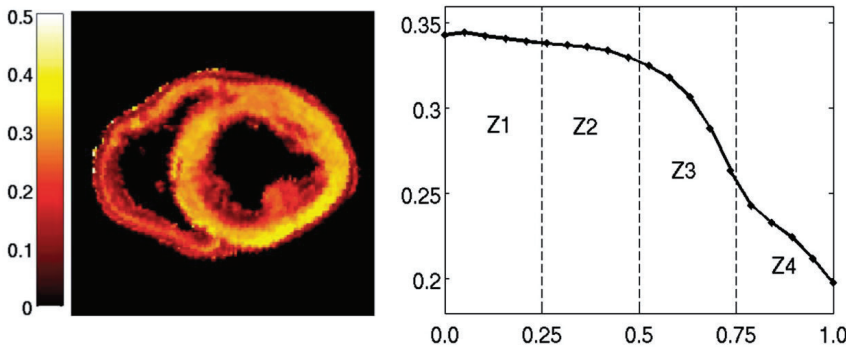

Figure 3.11: A)Color-coded fractional anisotropy map of formalin-fixed sheep heart. B)Plot of FA profile in the same slice as in figure A as a function of the normalized transmural depth. The cardiac wall is schematically divided in 4 regions, labeled Z1-Z4, starting at the epicardium. Reproduced from [29])

Also the quantification of helix angle of the cardiac myofibers has been object of several studies. The helix angle is usually defined as the angle between the short-axis plane and the local fiber orientation projected onto the local endocardial tangent plane. A schematic drawing of the helix angle is presented in figure 3.12

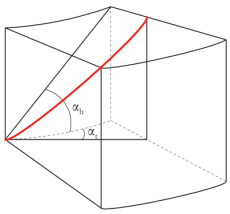

Figure 3.12: Part of the left ventricle with the definition of helix angle α_h and transverse angle α_t.

Chapter 4

Beyond DTI

DTI is a powerful imaging technique, that can provide anisotropy information, from which we can infer the structure of the tissue of interest. However the Stejskal-Tanner formula 3.22, which is the base of the DTI formalism, is only strictly valid in situations of free diffusion. In this case the PDF has a Gaussian shape and the normalized signal decay is purely mono-exponential, with the decay constant given by the Apparent Diffusion Coefficient (ADC). This simplified model of free diffusion can only approximate the real structure of biological tissues under certain conditions. Some findings [15],[55] suggest that heart muscles show a non mono-exponential behavior of diffusion, analogously to other tissues. While this behavior is typically observed for much higher b-values than normally used in clinical and research practice, it nevertheless shows that DTI is an over-simplified model of diffusion in the cardiac muscles.
DTI assumes water protons to move randomly in a single compartment in which diffusion is hindered but not restricted. However, since the previous studies showed the presence of a restricted behavior for high b-values, more sophisticated models of diffusion need to be introduced (i.e. multiple compartments of diffusion and possibly exchange between them). A short introduction about some models of diffusion will be presented in section 4.6.
Another important situation in which the DTI model is not valid, is the presence of different fiber populations within a single voxel. In general partial volume effects are extremely likely to occur, since the minimal spatial resolution achievable with DTI techniques is far larger than the typical diffusion scale. Hence in every imaged voxel several fibers with different diffusion behavior are typically present. Since the diffusion tensor can posses only a single maximum, it is therefore unable to identify multiple diffusion maxima arising from the presence of multiple fiber bundles within a single voxel. The main direction of the fiber, that is inferred from the main eigenvector of the diffusion tensor as measured in a typical DTI experiment, gives then information only about an average value of preferential direction in fibers in the voxel, and cannot be referred to the specifical spatial position of a given fiber. A simple graphical explanation of this effect is shown in figure 4.1.
This limitation has important implications in fiber tractography. It has been shown for instance that more than 60% of white matter tracts in the brain are likely to traverse regions with multiple fiber orientations at some point along their path. Also in the cardiac muscle there is evidence, from various imaging technique, of regions with crossing bundles of fibers. In such regions, the orientation extracted from the diffusion tensor (which always corresponds to the first eigenvector), is unreliable and may cause false negatives, in which tracking terminates, or false positives, in which tracking switches to an

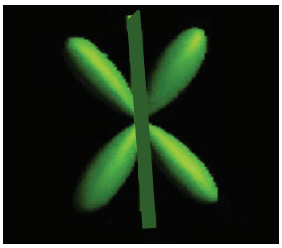

Figure 4.1: Voxel with two fiber populations intersecting at an angle of approximately 60°. The bright green line represents the estimation of fiber direction as obtained with DTI model, while the two lobes represent the real directions of the two populations crossing in that voxel.

unrelated adjacent tract. This is problematic when looking for structural information and especially in case an attempt is made to compare healthy and diseased tissues according to the different tract characteristics. Since this comparisons often rely on the difference in fiber lengths, the inability in following the real direction can easily lead to uncorrect diagnosis.
The presence of multiple fiber populations as a consequence of partial volume effects does not only have consequences in tractography, but also on the analysis of scalar indices parameters. Fractional Anisotropy (FA) is for instance often used as a marker for pathological conditions since it is supposed to reflect the degree of elongation of a fiber and often pathologies affect the physiology of cell structures. We already discussed why care has to be taken in comparing FA indexes between different scans, since it has been proven to depend on the SNR, conditions in which measurements are performed and postprocessing of the data. However, also the comparison of FA values within the same scan can lead to misinterpretations. In fact the presence of partial volume effects can decrease the apparent FA value, without any underlying tissue abnormality.

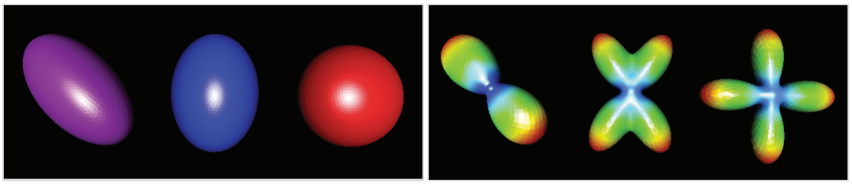

Figure 4.2: Different fiber configurations within a single voxel. From left to right: single fiber, 2 fibers crossing at a small angle and fibers crossing at 90° represented with DTI (left box) and high angular resolution techniques (right box). In the situation of two fibers intersecting exactly at 90°, the FA value may result close to zero (spherical-shaped ellipsoid) because of partial volume effects. Retrieved from *http://www.wias-berlin.de/research/ats/imaging/*

Since the 6 degree of freedom of the DTI model are not sufficient to resolve and analyse complicated structure, novel techniques based on high angular resolution approaches such as Diffusion Spectrum Imaging (DSI) or HARDI have been proposed to overcome these limitations. They can be considered as an extension of DTI. In this chapter a brief overview of these techniques will be given.

4.1 Introduction to q-space

The q-space analysis forms an interesting supplement to DTI. q-space formalism is the most natural framework to work with when diffusion data are involved, since it represents diffusion weighting as a function of the strength and direction of the diffusion encoding gradient applied during the MRI acquisition [52, 21]. DTI is a sampling of 6 points in q-space, since 6 different diffusion encoding directions are normally used. The effect of adding diffusion encoding gradients in a classical image acquisition sequence is to add additional dimensions to the sampling space [67]. In this section a short introduction to the q-space formalism will be given.
The image data acquired with MRI are usually 3D data, in the sense that for every position of 3D space is associated a single level of gray, that indicates the signal intensity at that given position $\mathbf{p}$. When diffusion encoding is added to the MR acquisition sequence, a different local displacement distribution of water molecules is obtained for every imaged voxel, giving information about the directionality and amount of diffusion taking place in that voxel. The combination of position information, together with the displacement probability gives rise to a 6D image. To put it in other words, in a normal anatomical MR image, a scalar measure is associated to each imaged voxel (different level of gray) that gives a measure of signal attenuation. The image is then 3 dimensional. When diffusion encoding is added, at each position $\mathbf{p}$ a new 3D image is added, where the molecular displacement is encoded over 3 dimensions. The resultant 6D images contains then 3 position variables and 3 spin displacement variables.
q-space is then the needed formalism to describe diffusion, like k-space is the natural formalism required to understand the formation of MR anatomical images.
For analysing the q-space, an important parameter to be introduced is the gradient wave vector or q-vector (sometimes also referred to as displacement vector):

$$\mathbf{q} = \gamma\delta\mathbf{g} \tag{4.1}$$

where γ is the proton gyromagnetic ratio for a water molecule, $\mathbf{g}$ is the applied diffusion weighting gradient and δ is the duration of such a gradient. The b-value used in DTI is related to the q-value with the relationship $b = \tau q^2$, where $\tau = \Delta - \frac{\delta}{3}$. In anatomical MRI measurements, the data are stored in the so called k-space, and a 2-dimensional inverse Fourier transform of the data can be performed to get the anatomical image. In an analogous manner, also q-space can be Fourier transformed to get the directional information about diffusion. The transform of the q-space gives a PDF (Probability Density Function) that describes the probability that water molecules in the tissue of interest will undergo a certain displacement due to diffusion in a given diffusion time. This PDF shows local maxima along the axis of fiber orientation at the single voxel level [51, 21]. In contrast with DTI technique, q-space formalism is then able to resolve different fiber populations within a voxel, exploiting the multiple local maxima of the probability density function, with an increased angular resolution. The number of directions in which the 3D diffusion function (q-space) is sampled translates into the maximum angular resolution of the technique[52].
A condition for q-space analysis is that the diffusion gradient pulses must be sufficiently narrow so that motion over their duration can be neglected. In other words the condition $\delta << \Delta$ must be fulfilled (this condition is referred to as *narrow pulse approximation*). With an NMR spectrometer and its strong gradients it is possible to achieve this condition and even cell microscopic structures and their sizes can be studied. However, considering the weak gradients in a clinical MRI scanner and the rise time needed for the gradients

to achieve their maximum values, this condition has to be violated. The consequences of this violation have already been discussed in section 3.2.3.

4.2 Multiple tensor approaches

The probability Density Function of displacement of water molecules relates to the NMR signal attenuation via a Fourier transform:

$$E(q) = \int P(\mathbf{x}|\tau) \exp(-i\mathbf{q} \cdot \mathbf{x}) d\mathbf{x} \tag{4.2}$$

When enough measurements of the signal attenuation $S(\mathbf{q})$ are acquired over a large range of $\mathbf{q}$, the PDF can be reconstructed. However often a given model for water diffusion is assumed, which allows a much faster sampling of the q-space. The zeroth-order model assumes the diffusion to be isotropic. The simplest model for the PDF $P(\mathbf{x}|t)$ that describes anisotropic diffusion is a multivariate, zero mean Gaussian distribution, with covariance $2Dt$, according to Einstein equation 3.15:

$$P(\mathbf{x}|\tau) = \frac{1}{\sqrt{(4\pi t)^3 |\mathbf{D}|}} \exp\left(\frac{-\mathbf{x}^T \mathbf{D}^{-1} \mathbf{x}}{4t}\right) \tag{4.3}$$

This is the behavior that is normally assumed in the Single Tensor Model (DTI).
In order to model the diffusion processes in a voxel with more than one fiber population, the multitensor approach has been proposed in literature. The gaussian model here is replaced by a mixture on n gaussian densities, each one characterized by a given water volume fraction f s.t. $0 \leq f \leq 1$ and $\sum_n = 1$. Each gaussian density relates to a different fiber population, which is described by a rank-2 tensor. This assumes the n population to be distinct, thus no water exchange between them. The measured signal can then be seen as a combination of the signal that would arise from a single fiber. The Multi Tensor approach belongs to the group of the so called *model based approaches*, since a priori information is needed regarding the nature of diffusion (like in DTI, diffusion is here assumed to be Gaussian within every single fiber) and the number of distinct fiber orientations present, since for every fiber population a different rank-2 tensor is needed. The multitensor analysis is made further complicated by the presence of different compartments showing different diffusion behavior (i.e. hindered and restricted) and this should be ideally included in the model.
This approach has many limitations: first of all it is really prone to artifacts and may produce unreliable data since the estimation of the number of fiber populations in a voxel is not straightforward. Furthermore it is shown to be unstable if more than two fiber populations are present[66] [1].

4.3 DSI

The analysis of fiber architecture with Diffusion Spectrum Imaging techniques is based on the same fundamental assumption used in all diffusion encoded imaging models: the level of diffusion is greater along the fiber direction[67].
DSI is a model-free methodology, in the sense that generalizes all the known diffusion techniques and doesn't need any hypothesis about the diffusion behavior, such as Gaussianity as assumed by DTI (see section 3.3), or multi-Gaussianity as assumed by the

multiple tensor approach (see section 4.2).
For an idealized pulse sequence with infinitesimally short gradient pulses, the probability density function (PDF) is simply the Fourier transform of the amount of signal attenuation as was already shown. The PDF may present several local maxima, each indicating a different fiber population. The PDF is then radially integrated to get the Orientation Distribution Function.
Different sampling schemes have been used for DSI, however the most common technique reported in literature is the one proposed by Kuo [36], with 515 different **q**-values, uniformly distributed on a regular cartesian grid inside a sphere.
From a theoretical point of view, DSI can be considered as the gold standard for diffusion imaging technique, since it is hypothesis free and its capability to resolve fiber crossing depends only on the angular resolution, i.e. on the number of diffusion weighted images acquired [67, 51, 21]. However the hardware requirements are high and its application is also severely limited by the very long acquisition time required, making this routine not feasible for patient studies. Furthermore, as it has already been remarked [64], the cartesian sampling of q-space is not efficient, because the signal is acquired even in regions where we know the SNR to be low, because it does not provide a natural framework for describing angular resolution and because the available acquisition time can be spent more efficiently in increasing the angular resolution.
In order to overcome these limitations, different acquisition schemes have been proposed in literature. One of the most common is the so called HARDI acquisition scheme, that will be introduced in the next section and that will be one of the main topics of this thesis.

4.3.1 DSI of the heart

To the best of our knowledge, only few attempts of studying the cardiac muscles with higher order approaches have been presented in literature. In [52] DSI tractography of the myocardium is performed on a rat heart, and remodeling after infarction is compared to normal fiber structure. In the control heart the double helical structure, already shown in previous studies using DTI, is observed, with smooth changes from the endocardium to the epicardium. The myofibers are seen in fact to spiral around the long axis of the left ventricle, with a left-handed helix at the subepicardium, which becomes a right-handed helix at the subendocardium. On the other hand, fiber architecture in the infarcted heart was severely perturbed. In particular residual myofibers extending from within the infarct to the border zone were observed. This residual myofibers intersect and form nodes with the transversely oriented fibers, forming a meshlike structure. This modified architecture could have important implications, since it may resist mechanical remodeling.
As previously explained, since DSI is able to resolve multiple fiber population within a single voxel, the 3D fiber structure can be reconstructed in greater detail. An example of fiber tractography for the control rat heart is shown in figure 4.3. The *ex vivo* rat heart 3 weeks after myocardial infarction showed a loss in myofibers, and reduced myofiber length. Furthermore the normal smooth evolution of myofiber orientation was lost, and replaced by myofiber strands with highly dispersed helix angles. A visual comparison of healthy and remodeled rat heart 3 weeks after myocardial infarction is shown in figure 4.4. The data from the fiber tractography were validated with histological analysis.
Another attempt of using DSI for the study of the mouse myocardium *ex vivo* can be found in [58]. In this work a fast spin echo diffusion spectrum sequence was used and diffusion glyphs for a short axis plane were calculated. A region of interest at the intersection of right ventricle and left ventricle was presented. Crossings at the region of intersection

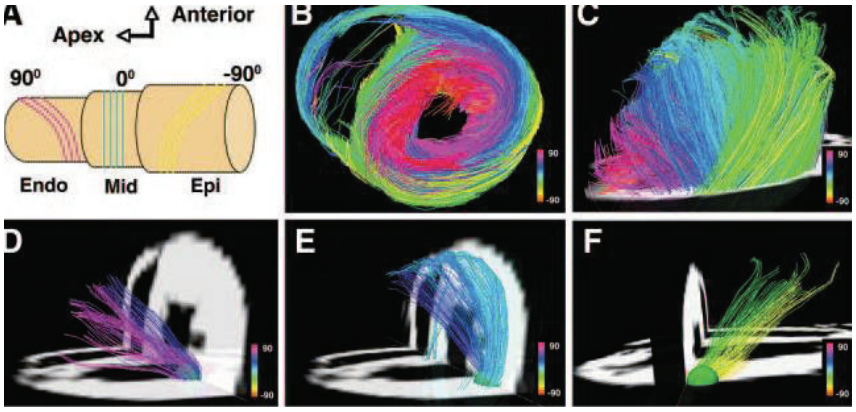

Figure 4.3: Variation of myofiber helix angle across the lateral wall. In figure D, E and F fibers intersecting a spherical region of interest are displayed. The different orientation of the helical structure could be observed, from positive at the subendocardium (D) to negative at the subepicardium (F). Zero helix angle was observed at the midmyocardium (figure E), where the fibers run circumferentially. Reproduced from [52].

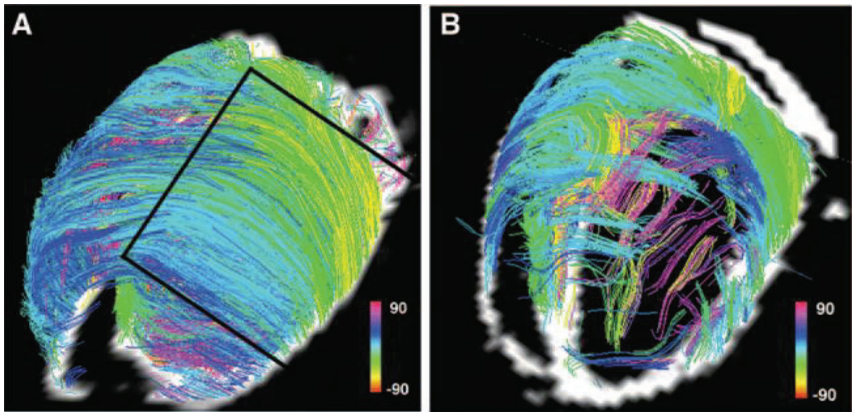

Figure 4.4: Whole volume tractograms of (A) normal and (B) infarcted rat heart. The high density of fibers, with smooth variation in the helix angle, was lost in the infarcted heart, where strands of residual myofibers extended from the infarct to the border zone. The residual myofibers were far fewer at the apex than at the base. Reproduced from [52].

with the RV could be clearly observed.

4.4 HARDI

DSI is in theory the "gold standard" for diffusion weighted imaging, since it involves a dense sampling of k-space. However this approach is time consuming and for many practical applications good results can be also obtained by undersampling the q-space over a sphere. HARDI (*High Angular Resolution Diffusion Imaging*) techniques are all based on the same principle: acquiring a large number of diffusion weighted samples with a constant q-value but along different directions. The q-space in this case is then sampled over a sphere, while in the case of DSI a cartesian sampling is required. Starting from

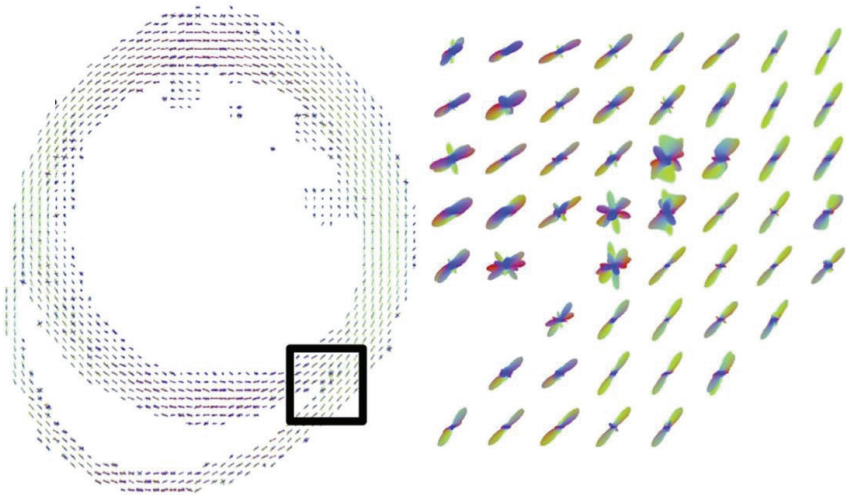

Figure 4.5: ODF for a single slice of the mouse heart obtained with DSI. Reproduced from [58].

spherical acquisition of diffusion data, the ODF (Orientation Distribution Function) can then be reconstructed with different algorithms. Two of the most known and reported techniques belonging to the HARDI family are q-ball imaging and Spherical Deconvolution (with its constrained version). These two techniques will be explained in the next sections.

4.4.1 q-ball imaging

q-ball imaging techniques was introduced by Tuch [65] in 2004. In its original formulation only one shell in q-space is required. q-ball imaging is, like DSI, directly based on the q-space formalism, but unlike DSI, its ODF is reconstructed directly from the diffusion weighted signal, without calculating the PDF (Probability Density Function) from the signal attenuation via an inverse Fourier transform. The ODF can in fact be recovered from the signal attenuation in q-space using the so called Funk-Radon transform. q-ball imaging belongs to the model-free algorithms, since does not require any particular modeling of the diffusion process inside the tissue.
The different HARDI methods differ between each others in the way they estimate the ODF and their (possible) multiple maxima, but also on the physical meaning of the relative ODF. The ODF that is normally recovered with q-ball imaging (and with DSI) is more properly called *diffusion Orientation Density Function* or dODF and is a spherical function that for every point on the sphere represents the statistical relative number of particles that have diffused along the vector joining that point with the center of the sphere. If we assume the different fibers to be aligned along the same axis, the dODF will then show a peak along that axis, indicating a greater level of diffusion along that direction. The dODF will in general be non zero in the other directions, due to the fact that diffusion also occurs, although in a smaller extent, in the direction perpendicular to the fiber direction and also to blurring arising from the estimation of the function from the data.
The q-ball reconstruction techniques uses q-vectors that have the same b-value, typically ranging from 1000 to 3000 s/mm^2. The required b-values are high, but lower than b values required for DSI [36]. The q-ball technique is much simpler and faster than DSI, but assumes that the selected b-value is optimal for the kind of tissue to be visualized

and is generally speaking really sensitive to noise [51]. However q-ball maintains many of the potential of DSI, but it's faster and easier to implement.

4.4.2 SD and CSD

The Spherical Deconvolution techniques was introduced for the first time in 2004 [61] and is currently one of the most widely used methods in literature for estimating fiber orientation in the brain from HARDI acquired data. The main underlying assumption of this method is that all the fiber bundles in the tissue of interest share the same diffusion characteristic. This means that all the differences in diffusion anisotropy are caused by partial volume effects. Thanks to this assumption, we can define the so called response function $R(\theta)$, which is the diffusion-weighted signal attenuation that would be measured from a single coherently oriented fiber population. It can be proved that the signal attenuation due to diffusion measured over the sphere is given by the convolution of the response function with the Orientation Distribution Function (ODF). The ODF can then be reconstructed from the measured data with a spherical deconvolution. The ODF calculated with the Spherical Deconvolution technique is more properly called *fiber Orientation Density Function (fODF)* and represents the relative number of fibers that are oriented along a given axis. Unlike the dODF, typical of the q-space based approach as DSI and q-ball, the fODF is theoretically not supposed to present peaks along orientations different from the main orientation of the fibers in the voxel of interest. For instance, if all the fibers in a voxel are oriented along the z-direction, we should expect the fODF to present a delta function along the z-axis and to be zero in all the other directions. This is of course not the case in practical implementation, since the ODF is typically blurred and presents different spurious peaks. For this reason, a peak threshold is often imposed in order to exclude small peaks that do not represent any underlying characteristic of the tissue.
One of the main differences between q-space imaging and SD (or CSD) is the fact that the latter are not model free, in the sense that specific assumptions are made about the diffusion profile, although the assumptions are much less stringent than the ones required for DTI. Since the average diffusion displacement is expected to be in the order of $10\mu m$ for a typical diffusion experiment, we can assume that there is no exchange between spatially distinct fiber bundles, so that the diffusion weighted signal arising from different populations can be considered to add up linearly.
In order to provide an intuitive idea of how the SD fitting works, a schematic drawing is presented in figure 4.6. Let's suppose n different fiber populations are enclosed within a

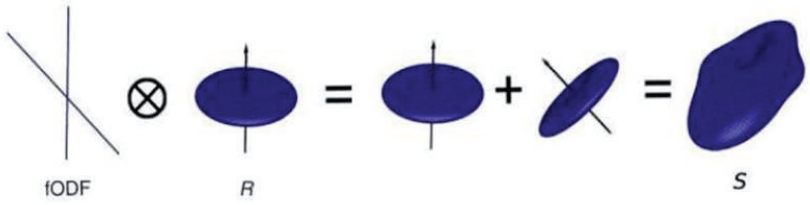

Figure 4.6: Schematic illustration of SD for a voxel containing two different fiber populations with distinct orientation

given voxel, each with volume fraction f. The measured diffusion-weighted attenuation signal $S(\theta, \phi)$ is given by the sum of the response functions for each population, weighted by their respective volume fraction and rotated in such a way that any single response

function is aligned along the direction of the respective fiber population. This can be expressed by following summation:

$$S(\theta, \phi) = \sum_i f_i \hat{A}_i R(\theta) \tag{4.4}$$

where $\hat{A}_i$ is the operator representing a rotation onto the direction (θ_i, ϕ_i). this operation can be expressed as a convolution over the unit sphere of a response function $R(\theta, \phi)$ with the fiber ODF.

$$S(\theta, \phi) = F(\theta, \phi) \otimes R(\theta) \tag{4.5}$$

A good estimation of the response function is necessary for correctly determine the ODF. We would generally expect the FA, as defined in the DTI framework, to be higher in voxels with a single fiber population. This assumption is often used for the estimation of the response function: the voxel with the highest FA is selected and assumed to represent the diffusion characteristics of a single fiber population. Although the DTI model could be used to estimate the response function, the Constrained Deconvolution method does not directly rely on the Gaussian model of diffusion. The response function, in fact, can and should be estimated directly from the data by measuring the diffusion-weighted profile in regions likely to contain a single coherently oriented fiber population. Most of the currently available techniques for the estimation of the response function start from a fractional anisotropy value, although some different approaches have been proposed to make the CSD approach more robust and completely independent on the tensor model [57].

One of the drawbacks of the spherical deconvolution based techniques, regardless of the mathematical algorithm used for the calculation of the response function from the signal decay in a voxel, is that the correct selection of the voxel to be used for the estimation of the response function requires some a priori knowledge about the structure of the tissue of interest coming from other imaging techniques, such as histology. Nevertheless, CSD is becoming more and more popular thanks to computational simplicity and speed.

The spherical deconvolution approach itself does not set an upper limit for the maximum number of fiber population that can be resolved, but this is done by the maximum harmonic order used in the calculation. The maximum harmonic order that can be estimated from the data is limited by the number of noncollinear diffusion encoding directions used to sample the q-space. In general, for fitting the data to the harmonic order $2n$, at least $(2n + 1)(n + 1)$ diffusion directions are required. We observe that for the second order

Table 4.1: Minimum number of noncollinear diffusion encoding directions required for a reliable estimation of the harmonic order n_{max}

n_{max}	# of directions
2	6
4	15
6	28
8	45
10	66
12	91

spherical harmonics, the number of directions needed is 6, as in the case of the DTI model. However it has to be observed that the spherical deconvolution operation is more sensitive to noise for higher order spherical harmonics. There is therefore a practical limit

to the maximum angular resolution that can be achieved using spherical deconvolution techniques. Although filtering can significantly reduce the noise effects, terms higher than $L_{max} = 8$ often need to be attenuated to such an extent that they no longer introduce significant improvements in the reconstructed fiber ODF. For this reason $L_{max} = 8$ is often the highest order used in practice [61]. While the best estimation for the orientational behavior of the different fiber populations is obtained for intersection occurring at 90°, the technique is often unable to resolve fiber populations whose orientations are too close. In the first version of the technique, the presence of negative side lobes was often observed, and this situation is of course nonphysical. This is mainly caused by the high level of noise typical of diffusion weighted images. In a later version this issues was however solved, by introducing a non-negativity constraint of the estimated ODF [62]. This version of the algorithm, know as Constrained Spherical Deconvolution (CSD) is nowadays the most widely used technique in literature for estimating the multiple maxima of the FOD from HARDI acquired data. CSD offers some advantages over SD: it can resolve fiber orientations separated by smaller angles than can be resolved with SD, without affecting too much the computational cost.

4.5 Diffusion Kurtosis

Diffusion Kurtosis Imaging (or DKI) refers to a relatively new diffusion imaging technique [28] which allows the quantification of how much water diffusion in biological tissues is non-Gaussian. In the simplest model, used for DTI, the PDF of water displacement is modeled to have a Gaussian shape, with width proportional to the diffusion coefficient. However, due to the complex structure of the tissue, that creates diffusion barriers and compartments, the distribution can deviate from a Gaussian and this level of deviations can be used to infer micro-characteristics of the tissue of interest.
In this section a short mathematical introduction is presented, together with practical implementation and possible added value of DKI over DTI.

4.5.1 DKI

The kurtosis is a dimensionless statistical metrics for quantifying the non-Gaussianity of an arbitrary statistical distribution. In particular, it is the normalized forth central moment of the water displacement distribution. In the case of molecular diffusion the kurtosis along a direction $\mathbf{n}$ (with $|\mathbf{n}| = 1$) is defined as:

$$K(\mathbf{n}) = \frac{<(\mathbf{r}\cdot\mathbf{n})^4>}{<(\mathbf{r}\cdot\mathbf{n})^2>^2} - 3 = \frac{\kappa_4}{\kappa_2^2} \tag{4.6}$$

where k_n are the cumulants of the distribution. In an analogous manner the diffusion tensor D along the direction $\mathbf{n}$ can be defined as:

$$D(\mathbf{n}) = \frac{1}{2t} <(\mathbf{r}\cdot\mathbf{n})^2> \tag{4.7}$$

Diffusion kurtosis is much more sensitive to tissue microstructure characteristics[68]. In fact, since it quantifies the deviation of the water diffusion profile from the Gaussian profile of unrestricted diffusion, it provides a measure the degree of hindrance and restriction.
In the case of isotropic Gaussian diffusion the kurtosis vanishes. If the distribution is more sharply peaked than a Gaussian, K is negative, while if the distribution is less sharply peaked than a Gaussian, K becomes positive. The theoretical lower bound for

K is -2. An example of isotropic displacement probability distribution with identical diffusion coefficients but different kurtosis values, is shown in figure 4.7

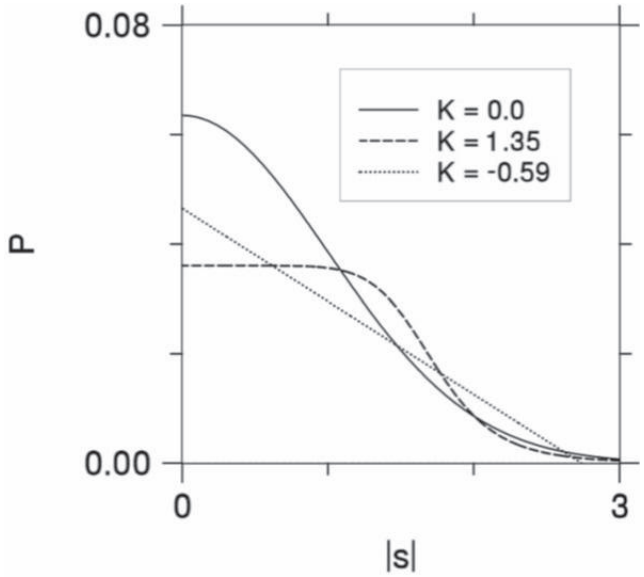

Figure 4.7: Three isotropic diffusion displacement probability distribution with the same diffusion coefficient but different kurtosis values. Adapted from [28]

Kurtosis can be determined by using a standard pulsed field gradients sequence, as the ones typically used for DTI. In general the signal attenuation in a PGSE experiment (in the narrow pulse approximation), given by:

$$\frac{S(g)}{S(0)} = \int_{-\infty}^{+\infty} e^{i\gamma\delta gr} p(r,\Delta) dr \tag{4.8}$$

can be rewritten as a summation of the cumulants of the distribution:

$$ln\frac{S(g)}{S(0)} = \sum_{p=1}^{\infty} \kappa_p \frac{(i\gamma g\delta)^p}{p!} \tag{4.9}$$

Since the diffusion displacement can be considered symmetric, all the odd order cumulants are equal to zero and the previous equation can be expanded as:

$$ln\frac{S(g)}{S(0)} = -\kappa_2\frac{(\gamma g\delta)^2}{2} + \kappa_4\frac{(\gamma g\delta)^4}{4!} - \kappa_6\frac{(\gamma g\delta)^6}{6!} + \cdots \tag{4.10}$$

When the distribution is Gaussian, the second cumulant is defined by $\kappa_2 = 2\Delta D$. By substituting this in the definition of kurtosis (eq. 4.6), we find then:

$$\kappa_4 = 4KD^2\Delta^2 \tag{4.11}$$

By formally substituting the two previous expressions for κ_2 and κ_4 and defining the b-value as $b = \gamma^2 g^2 \delta^2 \Delta$, the normalized signal attenuation can be expressed as a serie in powers of b:

$$\frac{ln[S(b)]}{\ln[S(0)]} \sim -bD + \frac{1}{6}b^2D^2K \tag{4.12}$$

For b sufficiently small the last term can be neglected and we can still think the Stejskal-Tanner equation to hold[1]. For increasing b the deviation of the signal attenuation from this simple form is supposed to become more and more pronounced.
It as been shown [28] that the kurtosis presents directional behavior as does the diffusion coefficient, in the sense that is changes according to the direction where the diffusion encoding gradients are applied. We normally refer then to Mean Kurtosis (MK), in analogy with the Mean Diffusivity, to indicate the average of the kurtosis over all possible directions (see figure 4.8).

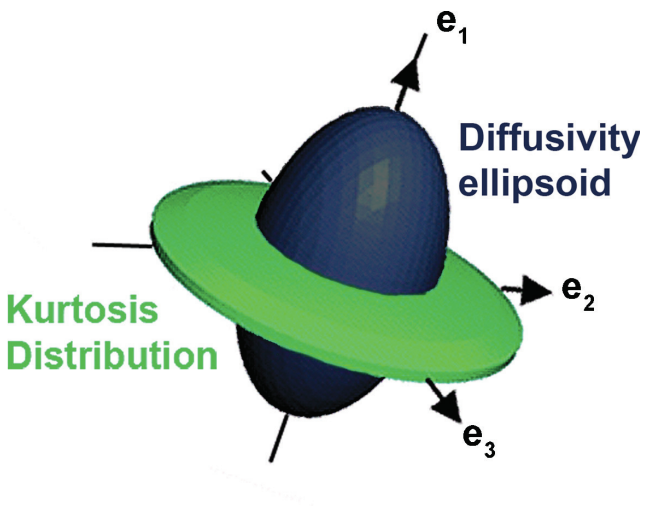

Figure 4.8: Schematic illustration of the diffusion ellipsoid (blue), representing the 3D diffusion distribution in a voxel, as calculated from the Diffusion Tensor. The three eigenvectors $\mathbf{e_1}$, $\mathbf{e_2}$ and $\mathbf{e_3}$ represent the principal direction of diffusion. The 3D kurtosis distribution, derived by the Kurtosis tensor, is represented in green and provides extra information to the Diffusion Tensor. Reproduced from [68]

The coefficient of kurtosis along the different directions can be arranged in a rang 4 tensor, with $3^4 = 81$ components, that can be reduced to 15 independent components due to symmetry. Since the diffusion tensor has 6 degrees of freedom, the combined number of degrees of freedom for kurtosis tensor and diffusion tensor is fixed to 6 + 15=21.
If a diffusion weighted MRI experiment is performed, with at least 2 different b-values along any different direction (plus a non diffusion-weighted image), K and D can then be calculated on a voxel by voxel basis by fitting the previous equation to the experimental signal decay as a function of the b-value. The b-values chosen for DKI experiment need to be bigger than the ones used in DTI (because we have to take into account the second order terms), but can be generally smaller than the typical values used in q-space imaging [27].
In order to obtain accurate estimation of the DKI parameters, the maximum b-values has to be chosen carefully. A common empirical approach to make the choice is to acquire the same image using a range of b-values, and then choose a b-value in the range where the signal decay can be approximately fit with a exponential curve, and one in the region where the non-exponential behavior becomes more pronounced. For the brain, the decay appears to be exponential up to around $2000 s/mm^2$ and normally the typical b-values used are 0, 2000 and 3000 s/mm^2. Since there are no studies about DKI in tissues other

[1]Here the definition "sufficiently small" refers to the nature of the tissue

than brain, a guideline for the correct b-values to be used has not been presented yet, and an appropriate b-value range as to be established before starting the acquisition protocol.

4.6 Models of diffusion

In the framework of DTI, molecules are considered to be moving almost freely and experience hindered diffusion (Gaussian diffusion). If this model was strictly valid, we would expect the signal decay due to the application of a diffusion encoding sequence to be exactly exponential as a function of the applied b-values. While this approximation can be considered to hold for small b values, for high b-values a clear deviation from an exponential decay can be seen[3]. An example of this behavior in a slice of the left ventricle of a pig heart is shown in figure 4.9.

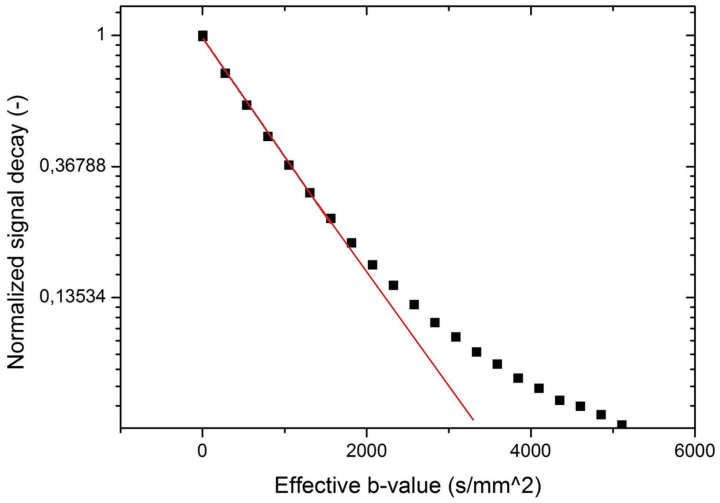

Figure 4.9: Normalized signal decay plotted in a logarithmic scale as a function of the effective b-value applied.

The simplest model that takes into account the non mono-exponential decay is the bi-exponential model. Two water pools are here considered, characterized by a fast and a slow diffusion coefficient respectively. In every compartment the diffusion is modeled to be Gaussian and there is no interaction between different compartments. In other words, every compartment can be thought as having completely non permeable barriers.
In the case of bi-compartment model, the signal decay as a function of b-value can be fitted to a bi-exponential curve [3]:

$$\frac{S}{S_0} = f_{slow}e^{-bD_{slow}} + f_{fast}e^{-bD_{fast}} \tag{4.13}$$

where f and D are the volume fractions and the diffusion coefficients associated with the fast and slow diffusion compartments, with $f_{fast}+f_{slow} = 1$. Some authors considered the fast-diffusing compartments to be related to water molecules in the extracellular space, while the slow-diffusing components was associated to intracellular space. This model, although interesting, does not account for the residence time of the molecules in the fast

and slow compartment according to the measurement time. It has been observed in fact that the values of f and D in the previous model change as a function of the diffusion time $t_d = \Delta - \frac{\delta}{3}$, suggesting that exchange occurs during the experiment between the different compartments. Furthermore, despite a good fitting of the signal attenuation with a bi-exponential model in a wide range of tissues and organs, the water volume fractions calculated did not correspond with the known ratio between intra-cellular and extra-cellular compartments [68].
A more complicated model of water diffusion, that takes into account water exchange, was introduced by Lee and Springer [38]. In this model a temporal factor is introduced, in such a way that water fractions are not only related to physical compartments of water molecules, but rather connected to the "residence time" of those molecules in each compartments during the acquisition.
Some complex multi-compartment models of diffusion have been presented in literature (such as CHARMED, AxCaliber and Ball and Stick) to estimate fiber diameter, fiber density and fiber orientations, but they mainly refer to microstructural parameter in the brain tissue. Only few studies have been presented addressing the problem of modeling diffusion behaviors in the myocardium.
In the study of Forder et al. [25] isolated perfused rat hearts were measured along 10 different diffusion encoding directions and multiple b-values for a single diffusion time ($t_{diff} = 10.5$ ms) and the data fitted to a simple bi-exponential tensor model. The diffusion tensor parameters were then estimated for each of the two compartments. The results showed an higher degree of anisotropy for the slow diffusion compartment, suggesting that this contribution may arise from the extracellular space, while the fast component may arise from intracellular space. However the possibility of the fast diffusion compartment to be related with the microvasculature of the heart cannot be completely excluded, since these microcapillaries run almost parallel to the fibers, in such a way that the fiber tracking would present the same results. Although the FA values were different for the two compartments, the directional information derived from the diffusion tensor were highly comparable. In fact the helix angle calculated from the first eigenvectors for the two different compartments didn't show differences, suggesting that the bias introduced in DTI-based tractography when the slow component of diffusion is neglected (i.e. for small b-values) is negligible.
In the study of Kim et al. [55] the dependence of diffusion time on apparent diffusion tensor parameters was investigated for fresh calf hearts. The results show an increase in λ_1 and decrease of λ_2 and λ_3 as a function of increasing diffusion time. However this study has an important limitation, which are the low b-values investigated (up to 1400 s/mm^2) which are not enough to show the non-mono-exponential decay.
To the best of our knowledge only these studies addressed the problem of a more sophisticated modelling of diffusion in the myocardium. The research in this sense is far behind than in the brain, and basically the only model used in present research is the one of DTI.

Part II

Results and discussion

In this study different diffusion MRI experiments were performed in order to get a deeper knowledge about the myofiber and laminar architecture of the heart. The acquisition parameters and the processing steps used in each experiment will be introduced in the corresponding chapters.

4.6.1 Tissue preparation

A total of 5 pig hearts obtained from a local slaughterhouse were studied. The excised hearts were rinsed with normal saline in order to remove the blood excess. The procedure was carried out within 4 hours after the animals were killed. Afterwards, the hearts were stored in 4% paraformaldehyde for at least three weeks before scanning.
24 hours before the first MRI scan, the hearts were rinsed with water to remove the paraformaldehyde excess and placed in a water bath for rehydration of the tissues. Immediately before the MRI scan, the hearts were dried carefully and placed in a well sealed plastic bag.
Additional experiments were performed on tissue samples with size of approximately $4 \times 2 \times 2$ cm cut from heart 1. The specimens were placed in an polycarbonate cylindrical container, slightly smaller than the inner diameter of the coil, which was filled with Fomblin (Solvay Solexis S.p.A. Italy) in order to prevent sample dehydration and the generation of susceptibility artifacts arising from tissue-air interfaces. In order to avoid movements during acquisition, the sample were kept in place by surrounding it with a medical gauze drenched in Fomblin.

4.6.2 Imaging

Experiment on the complete hearts were performed with a clinical 3 T MR scanner (Philips Achieva, Best, The Netherlands) and a preclinical 9.4 T scanner (Bruker BioSpin Gmbh, Germany) was used for high resolution scans of small heart specimens.

3 T

The 5 hearts were imaged on a clinical 3 T MR scanner (Philips Achieva, Best, The Netherlands). A 8-channels head coil was used for signal reception. For each complete heart 3 different experiments were performed:

- Experiment 1a: Mixing time experiment (diffusion maps acquired with different mixing times and different b-values)
- Experiment 1b: Kurtosis analysis (dataset acquired with 30 diffusion encoding directions and 4 different b-values)
- Experiment 1c: HARDI and DTI analysis (dataset acquired with 100 diffusion encoding directions and one single b-value)

The processing algorithm for HARDI analysis (Experiment 1c) was validated using a phantom of crossing fibers. The acquisition details for each experiment will be given in the corresponding sections.

9.4 T

The tissue specimens dissected from heart 1 were imaged with a 9.4 T Bruker preclinical scanner (Bruker BioSpin Gmbh, Germany). A quadrature birdcage coil with a 35 mm inner diameter was used for RF transmission and signal reception.
The additional experiments were performed in order to provide additional insight into the results obtained at 3 T and can be classified as follows:

- Experiment 2a: Mixing time experiment (diffusion maps acquired with different mixing times and different b-values)
- Experiment 2c: HARDI and DTI analysis (dataset acquired with 100 diffusion encoding directions and one single b-value)

4.6.3 Data processing

All data were preprocessed using DTITools, a toolbox developed by Martijn Froeling in Wolfram Mathematica 9. The first step was to convert the DICOM image data into Nifti format [46], a standard data format for diffusion MRI data. The data in Nifti format were then imported in DTITools. The MRI images were first denoised, using a Rician noise suppression algorithm, and then registered to the average of the non-diffusion weighted images for each dataset. b-matrix re-orientation was taken into account into the process of image registration.
Signal to Noise ratio was calculated with the difference method in two identically acquired unweighted images [49].

Chapter 5

Mixing time experiment

In this chapter the dependence of measured parameters on the applied b-value and experimental diffusion times, and its connection with underlying properties of cardiac tissue was investigated for the whole heart at 3 T and for heart specimens at 9.4 T. A simple bi-exponential model of diffusion was used to fit the signal decay.
Different ranges of b-values and diffusion times were then also used for standard DTI fitting. Most of the cardiac MRI studies presented in literature generally neglect effects of non-Gaussian diffusion in their analysis. If the diffusion would be purely free and Gaussian, the signal would have a mono-exponential decay as a function of b-value and the b-value chosen wouldn't cause any difference in DTI index quantification. However, since a deviation of signal decay from mono-exponential is expected, it is also of interest to investigate the influence of b-value in the characterization of DTI-derived parameters, which would then allow an optimization of the range of b-values used in future DTI studies.

5.1 Ex vivo heart at 3 T

5.1.1 Imaging

Experiments for studying the influence of diffusion time and b-values on diffusion characteristics were performed. The diffusion weighted images were acquired on a 3T Philips Achieva human scanner. A standard clinical 8-channels head coil was used. Water diffusion was probed using a stimulated echo sequence (STEAM), as shown in figure 5.1.
A multishot echo planar imaging readout was used in order to reduce T_2 losses and spatial distortions typical of singleshot EPI.
The acquisition matrix was 64×64 for a FOV of 128×128 mm^2 with 2 mm slice thickness, yielding a spatial resolution of $2 \times 2 \times 2$ mm^3. In order to improve SNR, each acquisition was averaged 4 times. 9 short axis slices with 5 mm spacing were selected. 8 datasets were acquired with varying mixing time, keeping all the other parameters constant. The repetition time (TR) was set to 3500 ms, which was the minimum achievable value allowed by the acquisition of the dataset with the longest mixing time (TM=300 ms). The echo time (TE) was also set to its minimum achievable value, 55 ms, which was imposed by the acquisition with the shortest mixing time (TM=30 ms). SENSE factor 2 reduction and SPIR fat suppression were used.
For constant mixing time, the multishell acquisition (14 different b-values) was obtained by changing the value of the gradient strength. The gradient strengths required for achieving the same b-value decreased with increasing mixing time.

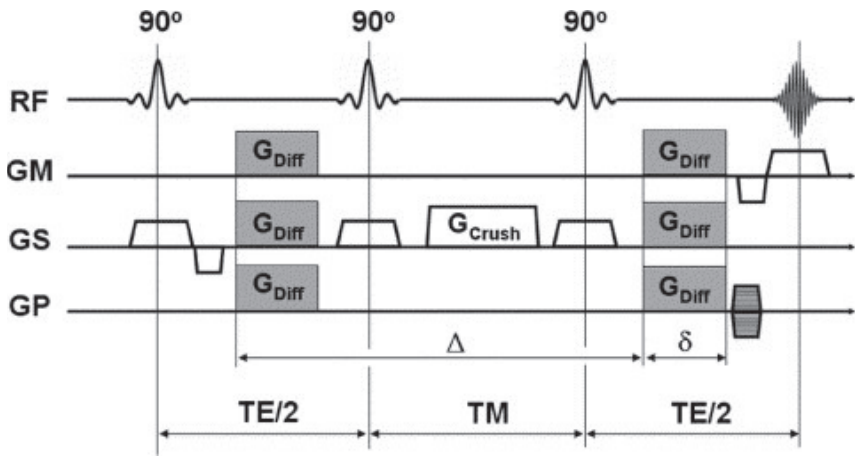

Figure 5.1: Schematic drawing of a stimulated echo diffusion weighted sequence (STEAM). The first diffusion-encoding gradient is placed between the first and the second 90° pulse and the second one after the third 90° pulse. The characteristic Echo Time (TE) and the mixing time (TM) are indicated. The diffusion time is given by $TE/2 + TM - \delta/3$. Reproduced from [4]

For each experiment the diffusion time was varied by keeping TE fixed while changing the mixing time. The duration of the pulsed gradient δ was set to 15.99 ms. The 8 different datasets were acquired with mixing time (TM) of 30, 50, 70, 110, 150, 200, 250 and 300 ms resulting in a diffusion time (t_{diff}) of approximately 53.26, 73.26, 93.26 133.26, 173.26, 223.26, 273.26, 323.26 ms respectively ($t_{diff} \sim \frac{TE}{2} + TM - \frac{\delta}{3}$).
The b-values for each experiment were 250, 500, 750, 1000, 1250, 1500, 1750, 2000, 2250, 2500, 2750, 3000, 3250 and 3500 s/mm^2. Diffusion encoding module was applied along 8 non-collinear directions calculated with the electrostatic repulsion algorithm in such a way to include the x,y and z directions in the scanner frame of reference. In addition to that, for each acquisition of the 8 diffusion encoded images, a non-weighted image was acquired. Each dataset consisted then of 14 B_0 images and 112 diffusion weighted images. A summary of the acquisition parameters used is presented in table 5.1.

Table 5.1: Acquisition parameters for the mixing time STEAM experiment at 3 T. For each mixing time, the minimum gradient strength (corresponding to a b-value of 250 s/mm^2) and the maximum gradient strength (corresponding to a b-value of 3500 s/mm^2) are included.

$TM(ms)$	$t_{diff}(ms)$	$\mathbf{g}_{min}$ (mT/m)	$\mathbf{g}_{max}$(mT/m)
30	53.26 ms	3.94	59.94
50	73.26 ms	3.65	51.11
70	93.26 ms	3.23	45.30
110	133.26 ms	2.70	37.89
150	173.26 ms	2.37	33.23
200	223.26 ms	2.09	29.28
250	273.26 ms	1.75	26.46
300	323.26 ms	1.73	24.33

The total acquisition time for each dataset was $\sim$ 58 minutes, resulting in a total scan

time of ~ 8 hours.
The acquisition of the 8 dataset was randomized in time (the data were acquired in this order: $TM = 30, 70, 150, 50, 250, 200, 300, 110$ ms). This was done to make sure that changes in ADC were not caused by an increase in the temperature of the sample due to RF heating or an other time-dependent drift in the scanner signal acquisition pipeline, which could cause a systematic shift of ADC towards higher or lower values for increasing scan time if the acquisitions were not randomized.

5.1.2 Data processing

Before processing the data, the b-matrix was corrected for the effects of imaging gradients using an algorithm written in Mathematica. This was done in order to evaluate the influence of cross-terms in the effective b-values.
A second preprocessing step was to register all the images for all the datasets to the first image in the dataset acquired for $TM = 30$ ms. In fact the images within each dataset didn't show any evident distortion, thanks to the use of multishot readout, but a systematic shift of the images in the phase direction was present.
In the datasets acquired for the mixing time experiment, the algorithm of noise suppression was not applied.

Bi-exponential fitting

For bi-exponential fitting, the registered images were then joined in a single dataset, and the signal was measured in ROIs in which the fiber orientations were known.
Along each direction, the Apparent Diffusion Coefficients (ADC) were calculated by fitting the measured attenuation of the signal to the slow-exchange limit two compartments model (eq. 5.1):

$$\frac{S}{S_0} = f \exp(-bD_{fast}) + (1 - f) \exp(-bD_{slow}) \tag{5.1}$$

where S and S_0 are the signal intensities in the presence and absence of diffusion sensitizing gradients, D_{fast} and D_{slow} are the ADC of the two possible water populations and b indicates the true b-value obtained after correction of the b-matrix. The data were fitted using the LM (Levenberg-Marquardt) routine provided by Origin 8.5.1 (OriginLab Corporation., Northampton, MA) in order to determine S_0, f, D_{fast} and D_{slow}.

Mono-exponential fitting of different shells

The dataset previously used for bi-exponential fitting was also used for standard single b-value DTI fitting, in order to study the influence of different b-values on the DTI-derived diffusion properties.
Single tensor measurement was performed for each shell with two b-values: the first one was zero and the second one was 250, 500, 750, 1000, 1250, 1500, 1750, 2000, 2250, 2750, 3000, 3250 and 3500 s/mm^2 respectively (the b-values effective used in the calculation were corrected taking into account the cross terms as previously mentioned, and do not exactly correspond to the theoretical b-values indicated here. However for simplicity from now on all the shells will be denoted by their theoretical b-value). Each tensor was estimated with a conventional DTI model ($S(b)/S(0) = e^{-bD}$), using a WLLS fitting

algorithm. The DTI indices (λ_1, λ_2, λ_3, MD and FA) were calculated on a pixel-by-pixel basis for each of the 9 slices. The values were then averaged over the complete cardiac wall and over all the slices. All the average values for the DTI parameters are expressed as mean±standard deviation (SD).

5.2 Ex vivo heart at 9.4 T

In order to investigate the diffusion properties at shorter mixing times than the ones previously used, specimens were cut from the heart and scanned at higher field strength (9.4 T).

5.2.1 Imaging

A similar acquisition protocols to the one at 3 T was used at 9.4 T. A standard STEAM sequence was used with multishot EPI readout. The acquisition matrix was 100×80 for a FOV of $5 \times 4\ cm^2$ with 0.5 mm slice thickness, yielding a spatial resolution of $0.5 \times 0.5 \times 0.5$ mm^3. Each acquisition was averaged 3 times. 8 datasets were acquired with changing diffusion time (t_{diff}=13.5, 23.5, 33.5, 43.5, 53.5, 63.5 and 73.5 ms), keeping all the other parameters constant. Diffusion was encoded along three perpendicular directions (x, y and z). The repetition time (TR) was set to 20000 ms and the echo time (TE) was set to its minimum achievable value, 18.74 ms.
For constant diffusion time, the multishell acquisition (15 different b-values) was obtained by changing the value of the gradient strength. The theoretical b-values used were 250, 500, 1000, 1250, 1500, 2000, 2500, 3000, 3500, 4000, 4500, 5000, 5500 and 6000 s/mm^2. The gradient duration was δ=4.5 ms and the gradient separation was 15, 25, 35, 45, 55, 65 and 75 ms respectively.
For each experiment at constant diffusion time, the acquisition time was 2.5 hours, resulting in a total acquisition time of 17.5 hours.

5.2.2 Data processing

The images acquired were registered to the non-diffusion weighted image acquired for diffusion time of 13.5 ms. The b-matrix correction in phase of post processing was not required, since the effective b-values were already calculated by the software of the scanner.
The data were fitted to a bi-exponential model, as explained for the data acquired at 3T, from which two different diffusion coefficients were estimated. From these diffusion coefficients the mean displacement was calculated for each diffusion time by using Einstein's equation.
All the data presented in the Results section refer to the same acquisition of a specimen of the left ventricular free wall.

5.3 Results

The results of b-values correction for the acquisition at 3 T, taking into account the imaging gradients shows a significant offset between the theoretical and the effective b-values. Table 5.2 shows the effective b-values corresponding to theoretical b-value of 0 s/mm^2

and 3500 s/mm^2 in the direction in which the offset is bigger (slice direction).

Table 5.2: Effective b_0 and b_{max} at 3T corresponding to the direction in which the offset is bigger (slice direction)

TM	t_{diff}	Effective b_0	Effective b_{max}
30 ms	53.26 ms	6.38 s/mm^2	3664.41 s/mm^2
50 ms	73.26 ms	9.99 s/mm^2	3746.77 s/mm^2
70 ms	93.26 ms	13.60 s/mm^2	3815.48 s/mm^2
110 ms	133.26 ms	20.81 s/mm^2	3929.84 s/mm^2
150 ms	173.26 ms	28.03 s/mm^2	4025.89 s/mm^2
200 ms	223.26 ms	37.05 s/mm^2	4130.38 s/mm^2
250 ms	273.26 ms	46.07 s/mm^2	4223.31 s/mm^2
300 ms	323.26 ms	55.09 s/mm^2	4308.09 s/mm^2

5.3.1 Bi-exponential fitting

Figure 5.2 shows the normalized signal intensity decay of a region of interest located in the area of papillary muscles for the three perpendicular directions x, y and z. Each curve is normalized by the signal intensity S_0 determined by bi-exponential fitting.

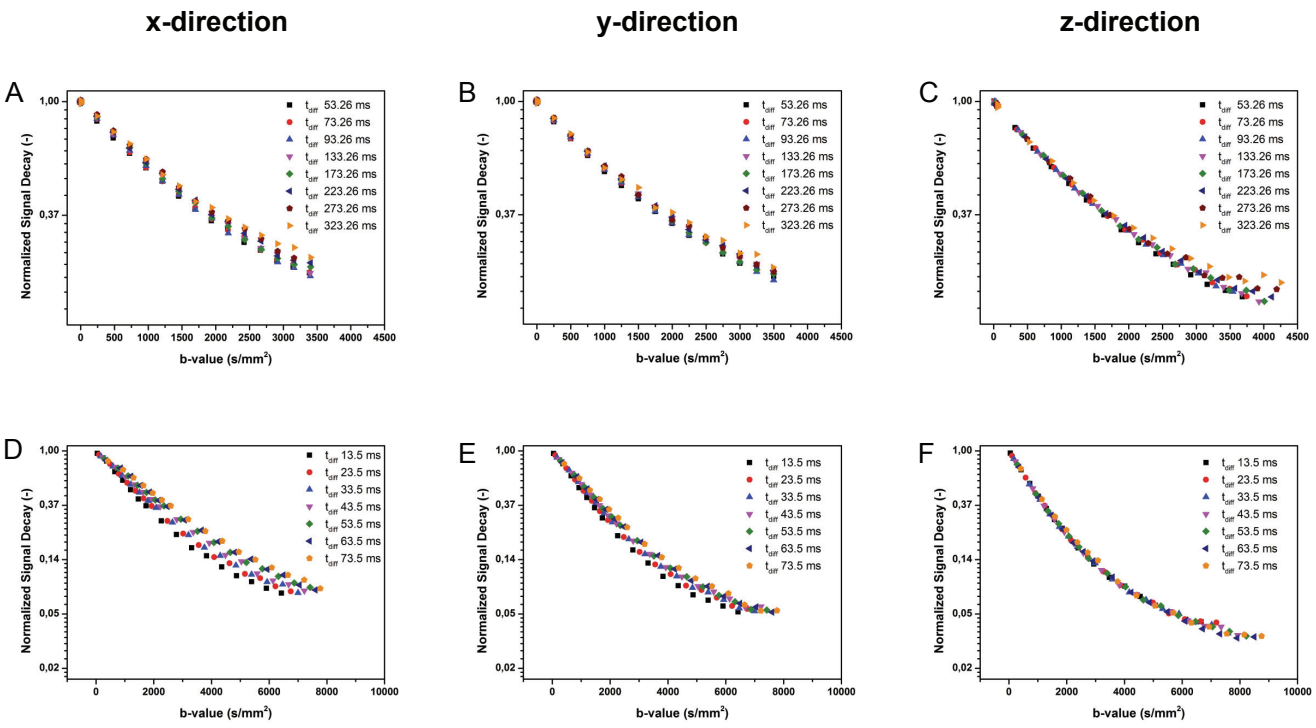

Figure 5.2: Normalized signal decay in a ROI in the region of papillary muscles. **A)** to **C)** Data measured at 3 T along x, y and z directions respectively. **D)** to **F)** Data measured at 9.4 T along x,y and z directions respectively.

In the ROI analyzed, containing papillary muscles, the principal direction of the fibers was approximately parallel to the z-azis.
A departure from mono-exponential behavior is evident for all diffusion encoding directions and for both 3 T and 9.4 T, indicating a substantial deviation from a Gaussian diffusion profile. Clear dependence of the measures signal attenuation on the diffusion time can be observed, with a general decrease in signal decay for increasing diffusion times. The general signal decay behavior is also observed to depend on the direction in which diffusion is encoded. In fact the deviation from a mono-exponential slope is more pronounced in the direction parallel to the principal direction of diffusion in the ROI (z-direction in case of papillary muscles) when compared to the radial direction.
For the directions perpendicular to the main fiber orientation, the deviation from a mono-exponential decay is small for the data acquired at 3 T, due to the relatively small b-values used in the investigation. At 9.4 T, where the more powerful gradient system allows the use of higher b-values, the deviation becomes more evident.
The separation of the curves obtained for different diffusion times is seen to be generally bigger for x and y directions than for z directions. Furthermore the variation of signal at constant b-value is smaller at 3 T, where longer mixing times are used.
The water fraction of the fast component of diffusion, indicated by f in eq. 5.1, is presented in table 5.3.

The water fractions obtained show a small trend of increase in x and y directions as a function of diffusion time. The water fraction calculated along the z-direction does not show any specific correlation with diffusion time, and the results obtained are substantially small when compared to water fractions in the radial direction.

Table 5.3: Water fraction relative to the fast component of diffusion, determined by fitting the experimental signal decay to a bi-compartment model. Results are presented separately for the 3 direction of diffusion (x, y and z) as a function of diffusion time.

t_{diff} (ms)	f_x (%)	f_y (%)	f_z (%)
13.5	94.1±5	95.2±2	89.2±2
23.5	94.2±5	94.4±2	86.8±1
33.5	94.5±5	95.4±2	85.0±1
43.5	95.0±6	95.2±2	87.3±2
53.5	94.2±6	95.0±2	84.9±1
63.5	96.0±6	95.5±2	85.4±1
73.5	96.0±6	95.6±2	84.4±2

In order to evaluate the effects of restrictions of diffusion, the restriction test was performed for the three orthogonal directions for the dataset acquired at 9.4 T (figure 5.3). The mean displacement was calculated using Einstein's equation from the diffusion coefficients previously calculated by fitting the signal decay to a bi-exponential model.
The data show the presence of two compartments of diffusion for encoding gradients applied along the axial directions of fibers (z-direction). The fast component in this case has a linear increase as a function of diffusion time, while the slow component has a regime of free diffusion for short diffusion times, and reaches then a constant value of displacement for long diffusion times. On the other hand, in the radial direction a dominant component is shown, which is restricted (or highly hindered). A second component is present in the radial directions, which is characterized by constant low displacement as a function of diffusion time. It has to be observed that this displacement, although small, is not equal

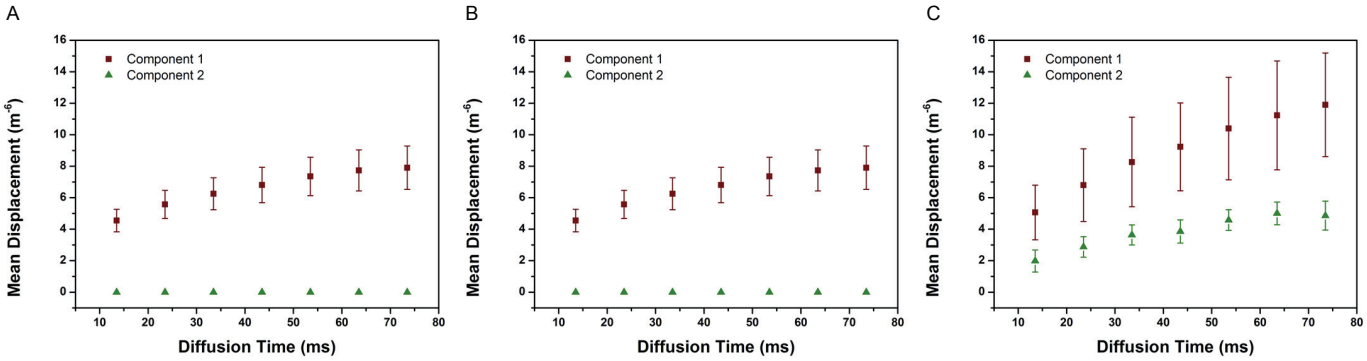

Figure 5.3: Restriction test indicating the mean displacement as a function of diffusion time along **A)** x, **B)** y and **C)** z direction respectively

to zero.

5.3.2 Mono-exponential fitting of different shells

After bi-exponential fitting, the data acquired at 3 T for the complete heart were analyzed with a tensor model and DTI parameters were estimated. The color coded FA maps obtained using the zero b-value and the 14 different shells (DTI model) are shown in figure 5.4 for the mixing time of 50 ms of a single slice. The myocardial fiber orientation inferred from the color map looks comparable for all b-values above 500 s/mm^2 and no apparent differences are shown. On the other hand the color map obtained for b=250 s/mm^2 shows a much higher irregularity in the color coded FA map and some regions in the left ventricle wall do not display color encoding for fiber orientation that seems anatomically correct.

Figure 5.5 shows the color coded FA maps obtained for constant b-value (b=1000 s/mm^2) and changing mixing time. Even though the SNR is significantly decreasing for increasing mixing times, the general overall fiber orientation indicated by the colors is preserved.

The variations of DTI indices with b-value and mixing time are presented in figure 5.6. The results indicate mean value over the 9 short axis view slices and over all the voxels across the cardiac wall. Different colors corresponding to the same shell indicate the DTI parameter obtained for constant theoretical b-value and changing mixing time.
The first eigenvalue shows a gradual decrease with increasing b-value for all the different mixing times. At constant b-value, the first eigenvalue increases with increasing mixing time. The change in ADC along the principal direction of diffusion as a function of diffusion time increases for increasing b-value. The change in ADC, calculated as λ_{max}-λ_{min}, is shown in table 5.4. Here the first two shells (b=250 s/mm^2 and b=500 s/mm^2) were not included, since the low b-values used are probably not suitable for an accurate diffusion contrast *ex vivo*.
For low b-values, the difference in λ_1 as a function of mixing time is negligible, and is seen to increase at a constant rate for increasing mixing time (see table 5.4).

The second eigenvalue shows a linear decrease as a function of b-value and the change in ADC as a function of b-value is less pronounced for the second eigenvalue than for the

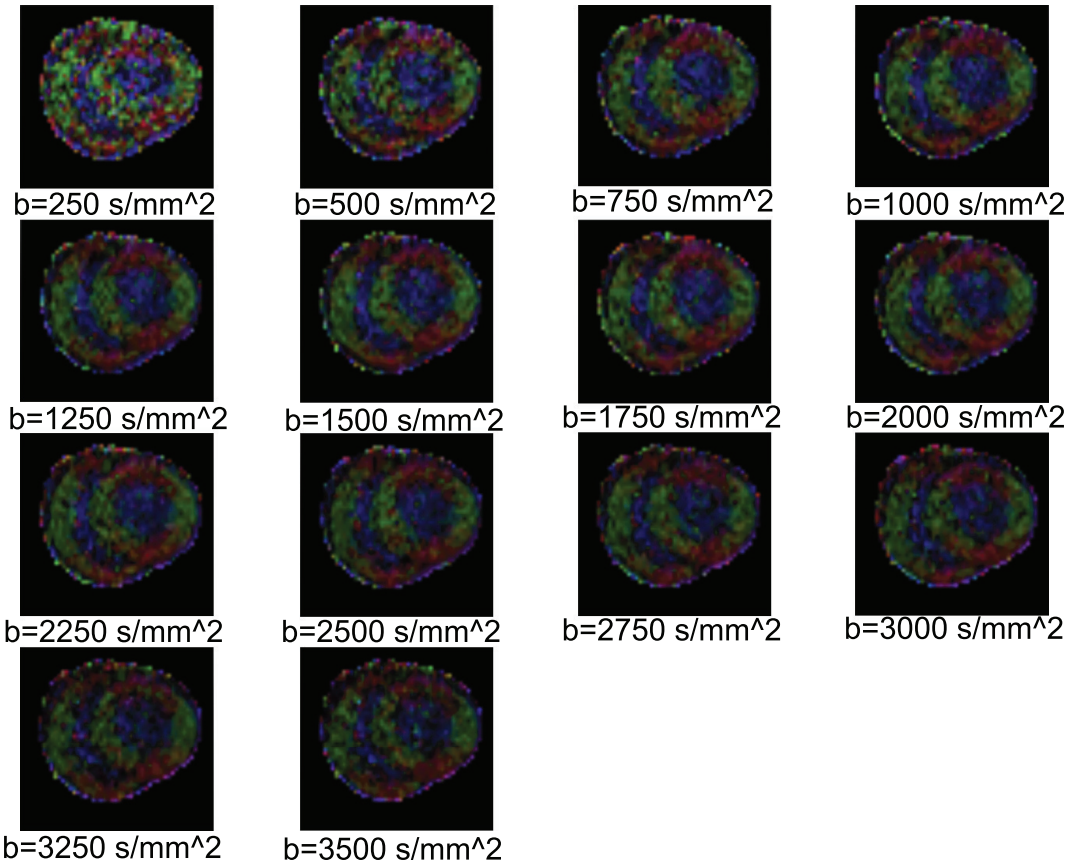

Figure 5.4: Color coded FA maps obtained from DTI fitting of different shell for the mixing time TM=50 ms. The colors indicate the direction of the fibers, determined from the first eigenvalue of the respective tensor. In the standard color convention used here red, green and blue represent fibers running left-right, up-down and in plane- out of plane respectively.

first one (see table 5.4).
The third eigenvalue for low mixing times shows an initial small decrease as a function of b, after which a plateau value is reached. On the other hand, at high mixing times the value is observed to be the same over the whole range of b-values.
The MD shows a decrease as a function of the applied b-value, with a trend similar to λ_1. FA also shows a general decrease as a function of b-value. The FA value is higher for longer mixing times at constant b-value but the difference between different mixing times becomes negligible for b-values greater that 3000 s/mm^2. For the shortest mixing time (TM=30 ms) the FA shows only a very small decrease as a function of b, while the decrease rate becomes more and more pronounced for increasing mixing times.

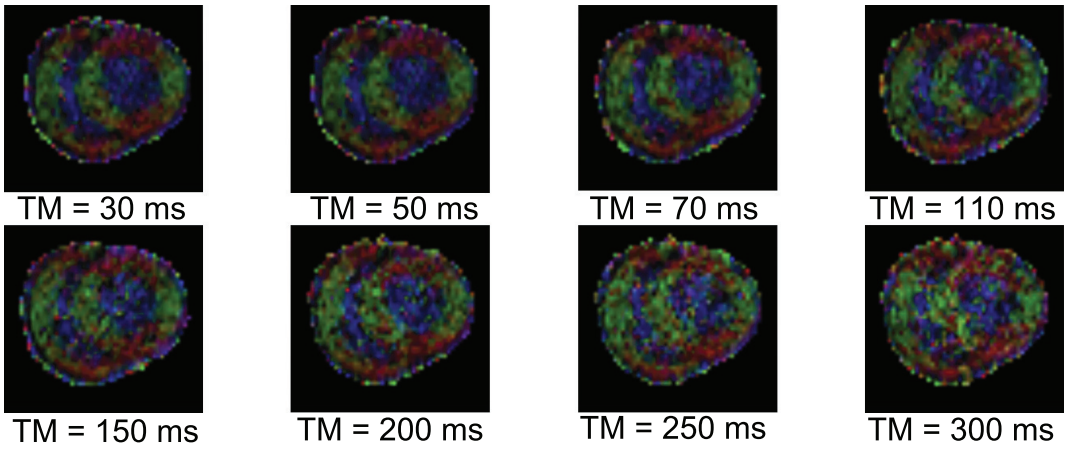

Figure 5.5: Color coded FA maps obtained from DTI fitting of a single shell (b=1000 s/mm^2) for changing mixing times. The colors indicate the direction of the fibers, determined from the first eigenvalue of the respective tensor. In the standard color convention used here red, green and blue represent fibers running left-right, up-down and in plane-out of plane respectively.

Table 5.4: Variation of λ_1, λ_2, λ_3, MD and FA with diffusion time as a function of the applied b-values ($\lambda_{max} - \lambda_{min}$), where the maximum value corresponds to a mixing time of 30 ms, and the minimum value corresponds to a mixing time of 300 ms. $\Delta\lambda_1$, $\Delta\lambda_2$, $\Delta\lambda_3$ and ΔMD are expressed in mm^2/s.

b-value (s/mm^2)	$\Delta\lambda_1 \times 10^{-3}$	$\Delta\lambda_2 \times 10^{-3}$	$\Delta\lambda_3 \times 10^{-3}$	$\Delta MD \times 10^{-3}$	ΔFA
750	0.042	0.0802	0.144	0.0855	-0.118
1000	0.056	0.081	0.137	0.088	-0.099
1250	0.071	0.085	0.125	0.100	-0.088
1500	0.077	0.084	0.116	0.100	-0.079
1750	0.081	0.080	0.110	0.096	-0.066
2000	0.093	0.089	0.111	0.099	-0.064
2250	0.094	0.088	0.103	0.099	-0.050
2500	0.102	0.088	0.098	0.097	-0.047
2750	0.109	0.085	0.091	0.098	-0.033
3000	0.107	0.089	0.091	0.096	-0.030
3250	0.110	0.086	0.094	0.098	-0.036
3500	0.106	0.088	0.089	0.100	-0.024

5.4 Discussion

In this chapter, the effect of different diffusion times and different b-values on the parameters derived from the diffusion tensor model was investigated. The signal decay as a function of the applied b-value was also analyzed by using a bi-exponential model describing two compartments in slow exchange.

In the phase of data processing, it was observed that the differences between the input and the effective b-values were non negligible, therefore the corrected b-matrix was used in the calculation. B-matrix correction for data acquired at 3 T was required since the gradients used for imaging in diffusion MRI add diffusion weighting and the so called

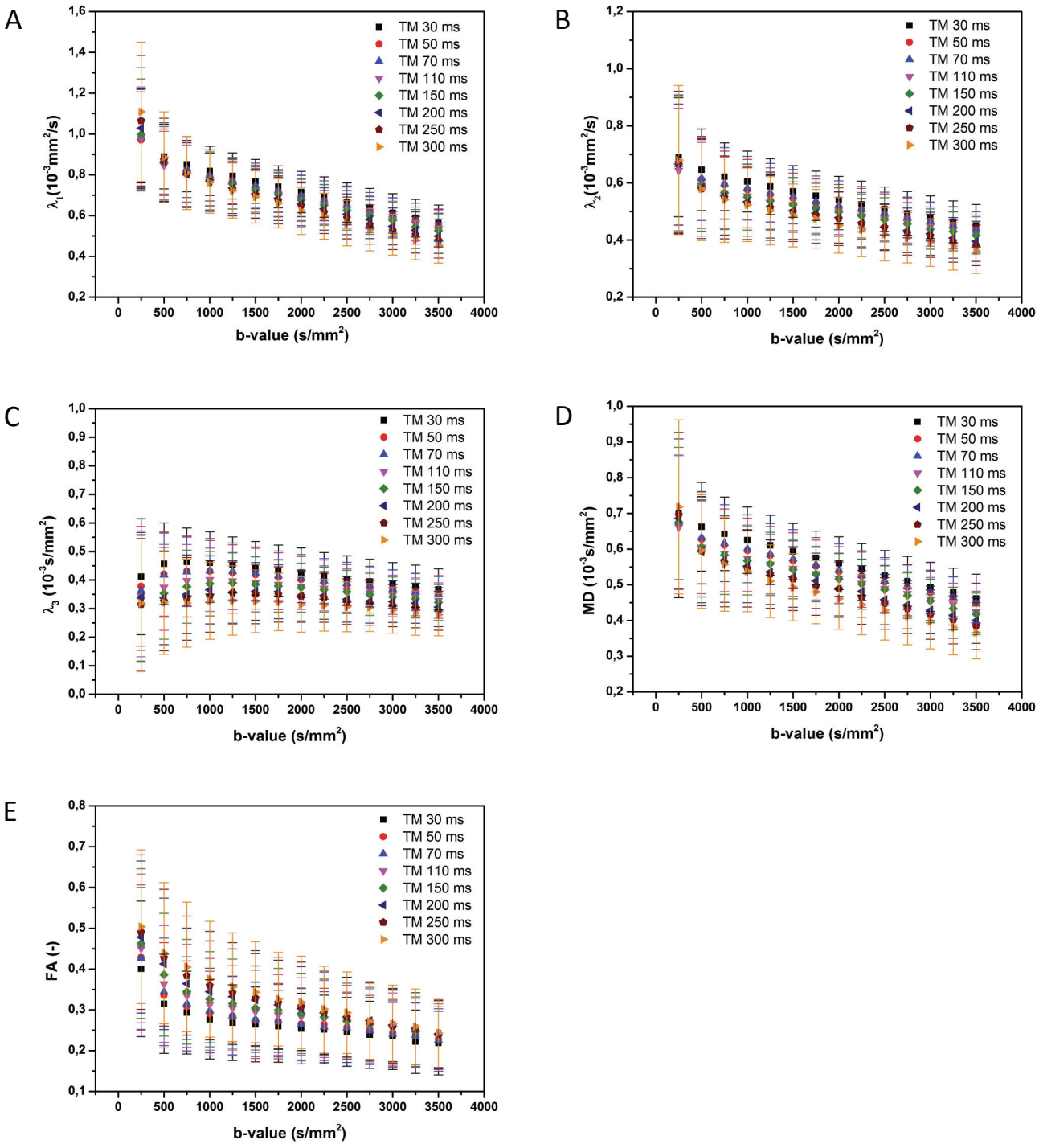

Figure 5.6: Diffusion tensor parameters calculated from DTI fitting for different b-values for mixing times (TM) of 30, 50, 70, 110, 150, 200, 250 and 300 ms. **A)**First eigenvalue. **B)**Second eigenvalue. **C)**Third eigenvalue. **D)**Mean Diffusivity. **E)**Fractional anisotropy.

"cross-terms" in the b-matrix. The most significant contributions are usually from the crusher and slice-selection gradients. In PGSE, their contribution to the diffusion weighting is non-zero as well, but usually negligible in practice. On the other hand, in STEAM that contribution is typically much more significant and the difference between the theoretical and the effective b-matrix increases for increasing diffusion time. This could lead, if the effect is not compensated for, to overestimation (typically along the slice direction) or underestimation of the ADC and significant bias in the estimation of the diffusion imaging derived parameters, as already shown for simulations and fixed monkey brain data [2].

Usually one of the most common applications of DTI is fiber tractography, therefore it is of interest to know whether different diffusion times and different b-values could affect the directionality of the tracked fibers. Interestingly, as shown in figure 5.4 and 5.5, the general orientation behavior of myocytes derived from the diffusion tensor model does not depend on the b-value used and on the diffusion time of the experiment. The only exceptions are the images obtained for b=250 s/mm^2, in which color coded FA maps show the inability to identify the correct fiber orientation in some regions within the left ventricle wall. This is probably due to the fact that such a low b-value cannot correctly encode diffusion in the *ex vivo* fixed heart. Although the presented diffusion maps do not provide quantitative indication about fiber angles, they nevertheless indicate that the b-value and the diffusion time do not have a strong influence in determining the fiber orientation in DTI model. Fiber angle evaluation was not performed because the used spatial resolution ($2 \times 2 \times 2\ mm^3$) was too low to provide enough voxels across the cardiac wall, but quantitative analysis of helix angle can be found in chapter 6.

Since diffusion times and b-values have little influence in the direction estimation of the first eigenvalue, for the solely purpose of myocytes tractography obtained from DTI it could be probably more favourable to use a PGSE sequence, in order to keep the signal higher (the use of STEAM causes in fact a loss of 50% of the signal compared to PGSE). Intermediate diffusion times can then be preferred over high diffusion times, in such a way to keep the TE of the experiment short. On the other hand, for some other higher order approaches, such has HARDI, it can be beneficial to increase the apparent fractional anisotropy of the tissue, since this would lead to a fiber estimation less susceptible to noise. In this case then the STEAM acquisition approach could be preferred over standard PGSE.

The decrease of the DTI-derived parameters as a function of b-values (figure 5.6) gives us further evidence that the signal loss in cardiac tissue is not only caused by Gaussian diffusion. The general decrease of λ_1 and λ_2 as a function of b-value experimentally observed was already reported for rabbit cardiac tissue *ex vivo* in [72] at constant diffusion time. This behavior is usually explained in literature with the presence of a "fast" and a "slow" diffusion pool. For shells acquired at low b-value, the fast component dominates the overall diffusion process, resulting in a bigger value for the ADC. For increasing b-value, the slow component gets more emphasized, leading to a decrease in apparent diffusivity. The effect of stronger diffusion encoding gradients (which result in higher b-values) is to dephase more and more the water component that is moving faster, leading to a progressive attenuation of the signal coming from this component. The slow component is hardly detectable for low b-values, but becomes prominent the more the signal from the fast component gets attenuated. This explains the general drop in the DTI eigenvalues as a function of b-values.

It is interesting to note that the differences between the maximum and minimum value for λ_1, obtained for TM=30 ms and TM=300 ms respectively, depend on the experimental b-value. In pure Gaussian diffusion regime, we would't expect the diffusion coefficient to strongly depend on the diffusion time, although a small effect is to be expected as a consequence of lower SNR for increasing experimental diffusion time. This regime of almost free diffusion can be observed for λ_1 at low b-values, in which the different ADCs present a small change as a function of diffusion time. After this regime of almost free diffusion, $\Delta\lambda_1$ is observed to substantially increase with increasing b-value. This shows at first the presence of two different regimes of diffusion along the radial direction, which may be caused by water exchange between the diffusion compartments, and a different permeability through the membranes that would obstruct the motion of molecules.

Different behaviors in terms of change in ADC as a function of diffusion time were observed for the radial and axial component, suggesting a more pronounced effect of boundaries and restrictions in the direction parallel to the fiber orientation that in the one perpendicular to it. In fact for the first eigenvalue an increased $\Delta\lambda$ is observed for increasing b-value, while for the second and third eigenvalues this quantity has a much smaller variation with b-value and can be seen as a first approximation to be constant. Another difference between the radial and axial component of diffusion, is the different deviation from mono-exponential decay in the axial direction, observed both at 3 T and 9.4 T (figure 5.2), in which the signal decay along the axial direction of fibers is observed to have a much more pronounced deviation from a linear slope (the graph is plotted in logarithmic scale) than along the two radial directions.

It has to be observed that in the curves of signal decay as a function of b-value, the amplitude of the signal-versus-b curves increases for prolonged diffusion time. This behavior has been already simulated for brain diffusion [45] and attributed to the fact that restricted diffusion dominates. In fact, in the same set of simulations it was observed that the amplitude of the curves was decreased for increasing mixing times when the effect of exchange was dominant. When comparing the curves obtained along the radial and axial directions, for the latter a great change in the curve slope is observed as a function of the diffusion time, indicating that along the radial direction the effect of restriction is more pronounced. On the other hand, along the radial direction the general trend is confirmed, but with much lower dispersion between the curves. This could be an indication of a combination of highly hindered (or restricted diffusion) and water exchange between different compartments along the axis parallel to the cell.

The combination of the previous finding suggests the presence of two components of diffusion in the direction parallel to the axis of the cell. This observation, together with the unchanged color-coded maps of the first eigenvalue shown in figure 5.4 and 5.5, would suggest that the fast and slow component of diffusion are aligned and coexist along the muscle cell. Although a precise correlation of the components with biological structures is not easily made, this could be explained by considering that water diffuses almost freely in the cell between the actin and myosin filaments for short lengthscales compared to the size of sarcomeres, which is normally estimated to be approximately 2 μm, and is of the same order of magnitude of the experimental value found for the displacement within the restricted component in the axial direction ($\sim 4\mu m$). For increased diffusion times, the water molecules experience the obstacle provided by the z-disc, which greatly reduce

the water mobility. In this case, instead of talking about "fast" and "slow" diffusion compartment and exchange between them, it would be more appropriate to talk about time-dependent diffusion: for short diffusion times the diffusion has a Gaussian profile, and the non Gaussianity becomes evident only for diffusion times substantially bigger that the typical size of a sarcomere.
The Gaussian behavior of diffusion in this case can also be observed in figure 5.3c, in which for the fastest component a linear correlation is shown between displacement and diffusion time up to 70 ms.
On the other hand, for the radial component of diffusion, the ADC calculated from the diffusion tensor model is shown to depend on the diffusion time for all b-values, suggesting that, for the investigated range of mixing times of the experiment at 3T, the water is almost constantly in regime of slow (or restricted) diffusion. A free (fast) component of diffusion can however be expected for shorter diffusion times than the ones used in the experiment at 3 T, as indirectly suggested by the constant small rate of change in the $\Delta\lambda_2$ and $\Delta\lambda_3$ (see table 5.4).

In order to probe the displacement of water along the radial direction in fast diffusion regime, which is less influenced by boundaries and restrictions, the use of shorter mixing times was required. For this reason the restriction test was performed on the dataset acquired at 9.4 T for diffusion times ranging from 13.5 to 73.5 ms (figure 5.3). Here the presence of a partially restricted dominant component of diffusion in radial direction is shown. If we look at the first component, diffusion displacement increases linearly as a function of time up to approximately 43.5 ms, indicating almost free diffusion for short timescales. Since the minimum diffusion time used in the experiment at 3T was $\sim$ 53 ms, this explains why little dependence on diffusion time was shown for the signal decay. This hypothesis is further strengthened by the observation that in the plot of normalized signal decay as a function of b-value at 3 T (see figure 5.2) the curves corresponding to different mixing times show almost no dispersion, while great dispersion is observed for the signal decay at 9.4 T.

If we look at the restriction test plotted for the radial direction (figure 5.3), after a transient time in which diffusion is almost free, a constant value for displacement is reached, which could be comparable to cellular diameter size. The association of restricted diffusion along the radial direction with the intracellular space is further strengthened by the evidence of a second component of diffusion in the radial direction, that although non-dominant is not characterized by zero displacement. Since the water fraction for this non-dominant component is estimated to be 5$\pm$1%, we can think of it as water diffusion in the extracellular space, and the rest (restricted component or highly hindered) to be associated with the intracellular space.

It could be interesting to decrease the mixing time even further in order to probe diffusion at the nuclear scale. However this can be difficult to investigate practically in a clinical system, due to hardware limitations. Extremely short diffusion times cannot be achieved at the moment with a standard PGSE sequence (Pulsed Gradient Spin Echo) in a clinical setting, due to the high gradient strengths required. The use of a preclinical system with more powerful gradients allows us to study shorter diffusion times, but still on a bigger length scale than the one typical of cellular structure in the radial direction, suggesting that these diffusion times cannot be reached with PGSE of STEAM. On the other hand, OGSE (Oscillating Gradients Spin Echo) diffusion encoding has been proved

to be able to provide diffusion times one order of magnitude shorter than with PGSE [73]. In this way DW-MRI measurements can be made much less sensitive to large scale restriction effects.

In relation to the effect of b-value on the tensor parameters, it has to be mentioned that DTI indices in muscles are susceptible to noise, as shown in [17]. The values of λ_1, λ_2, λ_3, MD and FA can be misestimated due to the effect of experimental noise and significantly deviate from their "true" value. However it was also shown that the error in the estimation becomes negligible for SNR of the non diffusion-weighted images above 20. In this study, the SNR of the non diffusion weighted images calculated with the "difference method" was 35 ± 5. Therefore the errors introduced by noise should have little to no influence in the general trend of DTI parameters previously described.

This study showed that important properties at different lenghtscales can be investigated with the use of multiple shells and different mixing times, and this could be applied in the future to provide a better understanding of cardiac anatomy and physiology, also in relation to diseases. On the other hand, although a multiple b-value approach could be beneficial in *ex vivo* experiment to better discriminate diffusion properties of different compartments, it can be difficult to apply *in vivo*, due to acquisition time requirements. Standard DTI is then more suitable, but one has to know which diffusion properties are of interest before performing diffusion MRI experiments and tune the b-value and diffusion time accordingly.

As a final consideration, it has to be noted that diffusion properties observed in this experiment may not hold in the *in vivo* case. Although a general decrease was found for all DTI-parameters as a function of b-value, these findings may not directly apply to the *in vivo* heart. In *in vivo* hearts in fact a third component of diffusion is to be expected, beside the "slow" and the "fast". This third component, also called pseudodiffusion component, arises from the effects of perfusion and is enhanced for low b-values. The analysis of the perfusion effects and the discrimination of perfusion from true water diffusion is usually made in-vivo by using the IVIM (Intravoxel Incoherent Motion) model ([7] and [12]), which describes the signal decay as the sum of two mono-exponential decay terms, each characterized by its own diffusion constant and its own water volume fraction. b-value optimization in this case would be more complicated since the diffusion parameters would also be influenced by the perfusion (or pseudo-diffusion) component. High b-values studies have not yet been performed in the *in vivo* beating heart, mainly because of the high cost to be paid in terms of TE increase and consequent signal loss. However, a complete study of diffusion in the myocardium should include both very low and high b-values, in order to probe both microflow and microstructural complexity.

5.5 Conclusions

Non mono-exponential diffusion behavior in myocardium was confirmed, both by bi-exponential fitting and indirectly by DTI fitting of the diffusion MRI data. In particular the presence of two components of diffusion was more evident for the principal direction of diffusion than for the directions perpendicular to it. Dependence of the signal decay on diffusion time was observed, with general decrease of ADC for both fast and slow component as a function of diffusion time. The clear presence of two components

in the axial direction was explained by considering both fast and diffusion components to coexist within the cell and to be more or less enhanced according to the time scale of the diffusion experiment. On the other hand, several evidences suggest that the radial component of diffusion for diffusion times used in clinical and research practice is always restricted within the cell. Taken together, these findings may provide useful information for acquisition optimization in the future.

Chapter 6

Kurtosis and Multishell analysis

In this chapter Diffusion Kurtosis Imaging (DKI) is applied in the study of the *ex vivo* porcine heart. Since kurtosis is a measure of the degree to which water molecules diffusion in biological tissues is non Gaussian, it could provide a more specific measure of tissue structure than conventional methods based on the diffusion tensor.
In the second part of this chapter, multhishell DTI fitting was performed in order to evaluate the regional differences in diffusion parameters across the cardiac wall and between right and left ventricle.

6.1 DKI

6.1.1 Imaging

For kurtosis analysis, the hearts were scanned along 30 non-collinear diffusion encoding directions with different b-values (b=1000, 1500, 2000 s/mm^2). In each dataset 12 non-diffusion weighted images were also recorded. Diffusion along each direction was encoded with a twice refocused spin echo sequence in order to reduce image distortions due to eddy currents (Δ_1=64.22 ms, δ_1= 15 ms, Δ_2= 19.30 ms and δ_2=19.13 ms). Along any given direction the different b-values were obtained by varying the strength of the diffusion encoding gradients and keeping the diffusion time constant. The acquisition matrix was 144×144 and the resulting voxel size was $0.97 \times 0.97 \times 2$ mm^3. The number of slices was varied for each dataset, between 61 and 73, in order to cover the entire long axis of the heart with the smallest possible number of slices. The timing parameters were TE=88 ms and TR=5700 ms. Multishot EPI readout (EPI factor=13) was used in order to minimize image distortions and shorten TE (compared to singleshot EPI). The minimum achievable TE was determined by the maximum b-values (b=2000 s/mm^2). A factor 2 SENSE reduction and SPIR fat suppression was used. In order to increase the SNR, NSA was set to 5. The total acquisition time for each dataset was $\sim$10 hours.

6.1.2 Data processing

After denoising and image registration, the kurtosis tensors for each dataset were calculated using ExploreDTI [39]. Data were evaluated by visual inspection of diffusion weighted images and residuals from the tensor fitting calculation.
The rank-4 kurtosis tensor was determined by fitting the signal intensity on a voxel-by-

voxel basis to the equation:

$$\frac{S(b)}{S(0)} = \exp\left(-bD_{APP} + \frac{1}{6}b^2 D_{APP}^2 K_{APP}\right) \tag{6.1}$$

From this tensor the Apparent Diffusion Coefficients (D_{APP}) and Apparent Kurtosis Coefficient (K_{APP}) were determined for both axial and radial direction.
The data were also fitted to a standard rank-2 diffusion tensor, from which axial diffusivity (λ_1) and radial diffusivity ($\frac{\lambda_2+\lambda_3}{2}$) were estimated.
Each map was masked based on a lower and upper threshold for FA values, in order to remove the background noise.
In order to evaluate statistical differences between diffusion parameters in the right and left ventricle, they were segmented in 5 short axis slices and for 4 different datasets acquired with the same acquisition parameters. Data are reported as mean±SD (over five slices and 4 datasets). The data were tested for statistically significant differences with one-way ANOVA, where $p < 0.05$ was considered significant. Statistical analysis was performed with Origin 8.5.1 (OriginLab Corporation., Northampton, MA).

6.1.3 Results

All datasets were evaluated for artifacts and were considered of good quality for DKI analysis. The residuals for DTI fitting were constant for the same shell and increasing for increasing b-values of the shell, indicating appropriate data fitting. Analysis of outliers didn't show any evident error in any of the diffusion weighted images.
The average values for kurtosis and D_{app} (derived from the kurtosis tensor) and the parameters derived from the diffusion tensor are plotted in figure 6.1 for a representative dataset.

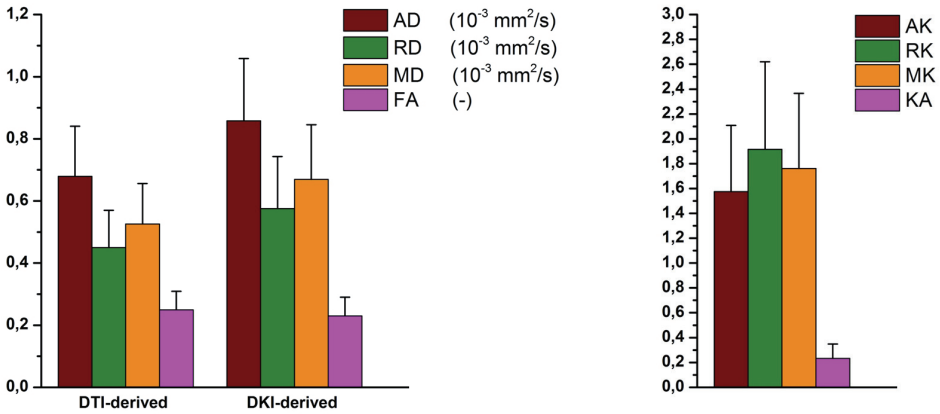

Figure 6.1: **Left** DKI- and DTI-derived parameters for the axial diffusivity, radial diffusivity, mean diffusivity and fractional anisotropy. **Right** Axial kurtosis, radial kurtosis, mean kurtosis and kurtosis anisotropy derived from the kurtosis tensor.

The diffusion parameters derived from the kurtosis tensor are observed to be higher than the corresponding values estimated from mono-exponential DTI fitting. The change

in the axial direction is 18%, while the change in the axial direction is 13%. This similar rate of increase results in negligible differences in the two values of FA.
The second graph of figure 6.1 shows that the kurtosis in the diffusion profile is significantly different from zero along all directions. In particular, the kurtosis along the radial direction is observed to be higher than the kurtosis along the axis of the fibers.
In order to visualize the regional differences of kurtosis and diffusion coefficients in the heart, kurtosis maps for 2 representative datasets are shown in figure 6.2 and compared to the diffusion maps. The diffusion maps here represent the ADC, as calculated from the standard DTI tensor.

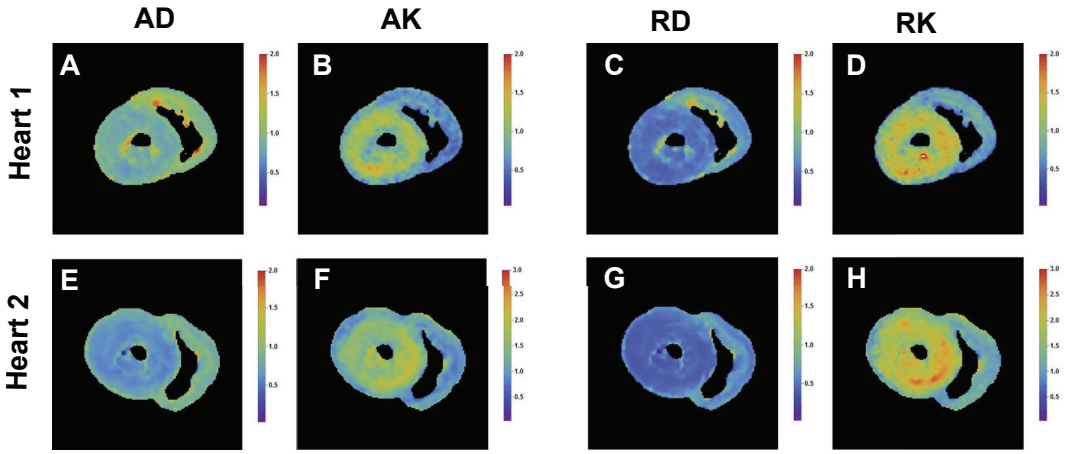

Figure 6.2: Diffusion and kurtosis maps calculated for two different dataset. **A)** and **E)** Axial diffusivity ($\times 10^{-3} mm^2/s$). **B)** and **F)** Axial kurtosis (-). **C)** and **G)** Radial diffusivity ($\times 10^{-3} mm^2/s$). **D)** and **H)** Radial kurtosis (-).

The diffusion maps for axial diffusivity and radial diffusivity in the short axis view do not show regional differences across the left ventricle wall and really small differences are observed between right and left ventricle. On the other hand, kurtosis maps for both radial and axial components show a large contrast between the right and the left ventricle. For each data set and each slice, the kurtosis in the right ventricle was lower than in the left ventricle. When comparing the axial kurtosis and the radial kurtosis, the latter shows an average bigger value, indicating that the deviation from gaussian diffusion for the combination of acquisition parameters used is more pronounced perpendicular to the fiber direction than parallel to it.
The average values for the left and right ventricle over 4 datasets and 5 slices for apparent diffusivity and apparent kurtosis are presented in figure 6.3.

A significant difference is present between kurtosis parameters in the left and right ventricle, both for axial and radial direction. Significant difference is also observed between the axial and radial kurtosis. When kurtosis is calculated along the radial direction of fibers, larger differences between the right and left ventricle are present than in the axial direction.
However, no significant changes were observed in the calculated diffusion coefficient, in which the only significant difference is found between the axial and radial diffusivity.

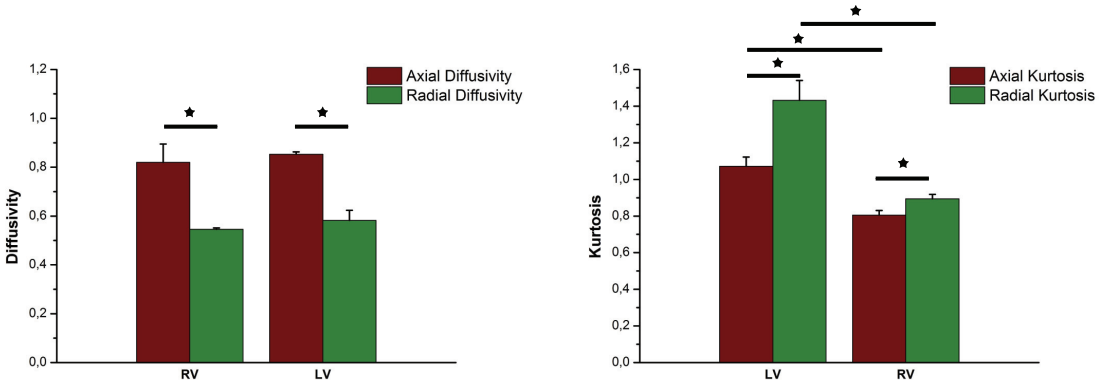

Figure 6.3: Diffusion and kurtosis parameters calculated in ROIs containing the segmentation of right and left ventricle. **Left** Axial and Radial Diffusivity ($\times 10^{-3} mm^2/s$) **Right** Axial and radial kurtosis. $\star$=p<0.05.

6.2 Two-Component Diffusion Tensor Analysis

6.2.1 Data processing

The same datasets used for kurtosis fitting were also used for two-component diffusion tensor analysis. After the denoising and registration steps, single tensor measurements were performed for diffusion weighted images corresponding to two b-values, namely 0 vs 1000, 0 vs 1500, 0 vs 2000 and 1500 vs 2000 s/mm^2 respectively. A fifth tensor was computed by fitting all diffusion weighted images (b=0, 1000, 1500 and 2000 s/mm^2) to a single mono-exponential model (ME). Each tensor was estimated with a conventional DTI model ($S(b)/S(0) = e^{-bD}$), using a WLLS fitting algorithm. The tensor calculation was performed using DTITools. The DTI indices (λ_1, λ_2, λ_3, MD and FA) were calculated on a pixel-by-pixel basis for each tensor and shown in a diffusion map for a characteristic dataset.
In order to quantify the changes in diffusion parameters, they were averaged over the complete heart, with the exception of the area of heart valves. All the average values for the DTI parameters presented here are expressed as mean($\pm$standard deviation) over all pixels in one representative dataset.
For each tensor the helix angle was calculated from the first eigenvector. The helix angle in a given point P is defined as the angle between the local circumferential direction and the projection of the fiber orientation (first eigenvector) on the plane parallel to the wall.

6.2.2 Results

Figure 6.4 shows the DTI parameters (λ_1, λ_2, λ_3, mean diffusivity and fractional anisotropy) maps calculated for different shells in a representative dataset.
All DTI indices derived from 0 vs non zero b-values are observed to gradually decrease with increasing b-value, as shown already in chapter 5.
Within the first 3 shells, in each map the right and left ventricle have an almost uniform value, but contrast is provided between them. All the parameters (excluding FA) show a decrease with increasing b-value. Larger changes are however observed in the left ventricle than in the right ventricle. By visual inspection of the diffusion maps for λ_1, λ_2 and λ_3,

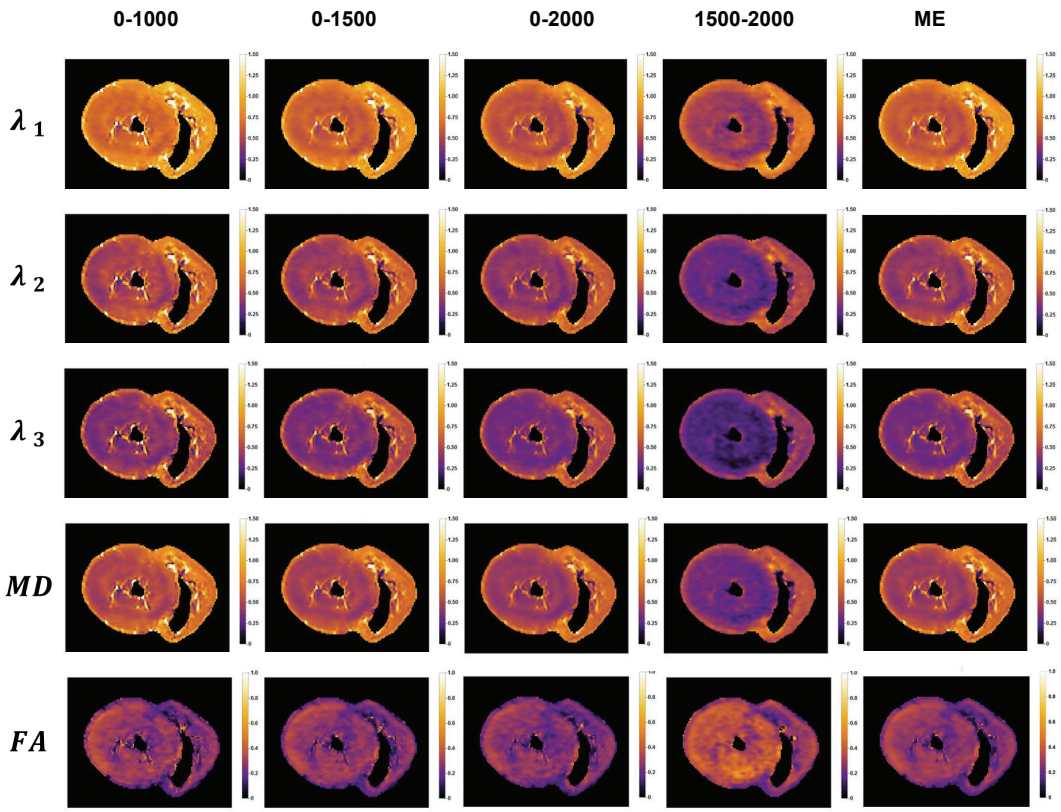

Figure 6.4: Diffusion tensor parameter (λ_1, λ_2, λ_3, Mean diffusivity and Fractional anisotropy) maps calculated from DTI fitting for 4 different shells (b=0-1000 s/mm^2, b=0-1500 s/mm^2, b=0-2000 s/mm^2, b=1500-2000 s/mm^2).

the right ventricle appears to be almost insensitive to the change in b-value, although a small decrease is observed. This causes the contrast between left and right ventricle to increase for increasing b-value. Diffusion contrast between right and left ventricle is more evident in the radial direction (λ_2 and λ_3) than in the axial direction.
FA maps show no significant regional differences between left and right ventricle. For each heart however, a region of increased FA for the shell 0-1000 was observed at the endocardium in the free wall. FA value is observed to decrease with increasing b-value, however the changes are really small.
The forth column of figure 6.4 shows maps calculated by fitting only the shell 1500-2000. Substantial decrease of all ADC values with respect to the first 3 shells was observed, combined with an increase in contrast between left and right ventricle. In this shell the average FA values results bigger than in the shell 0 vs non zero b-value.
The diffusion maps obtained for mono-exponential fitting are almost identical to the corresponding maps obtained for the shell 0-1500.
The previous observations were quantified by plotting an histogram of diffusion parameters for different shells. The error bars indicate standard deviation calculated over the complete heart (complete slice package).

The parameters derived from mono-exponential fitting of multiple shells are nearly identical to the parameters derived for the second shell (b=0-1500 s/mm^2). The fourth

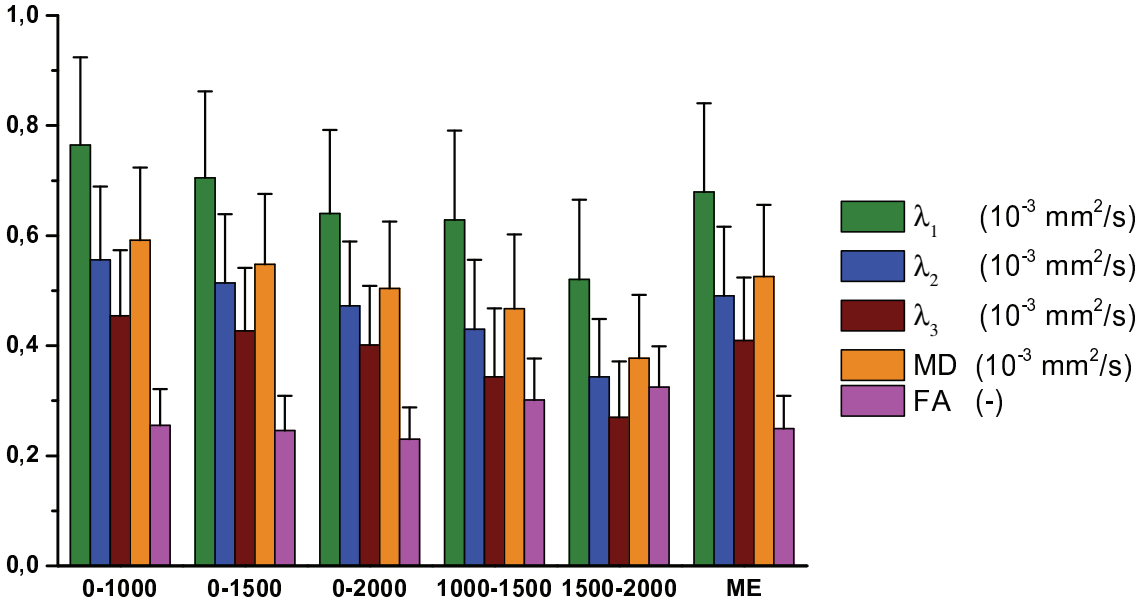

Figure 6.5: Diffusion tensor parameters calculated from DTI fitting for different shells (b=0-1000 s/mm^2, b=0-1500 s/mm^2, b=0-2000 s/mm^2, b=1500-2000 s/mm^2 and mono-exponential (ME) fitting.)

shell (b=1500-20000 s/mm^2) shows a general trend of decrease for the 3 eigenvectors and the mean diffusivity when compared to the 3 single shell parameters. However FA shows a significant increase with respect to the FA calculated for the other tensors.

For each tensor, helix angles were calculated. A map of helix angles for the same slice calculated from different tensors is shown in figure 6.6, together with a plot of helix angle distribution as a function of normalized transmural depth calculated in the septal region. In general all helix angle maps show a smooth change in orientation from inclination angle of $\sim -50°$ at epicardium to $\sim +80°$ at endocardium. The change in orientation is uniform across all wall regions and in different short axis slices (not shown).
The helix angle maps derived from different tensors do not show important differences between fiber orientation estimated at different shells. The plot of helix angle as a function of the normalized transmural depth in the septum shows that the helix angle profile determination is not affected by the choice of b-values used in the calculation.

6.3 Discussion

From the DKI maps it is possible to observe that a deviation from a Gaussian shape, quantified by the kurtosis of diffusion displacement profile, is present in all directions. This indicates that even at relatively low b-values the approximation of free diffusion is substantially incorrect.
The diffusion parameters derived from the kurtosis tensor are larger than those derived

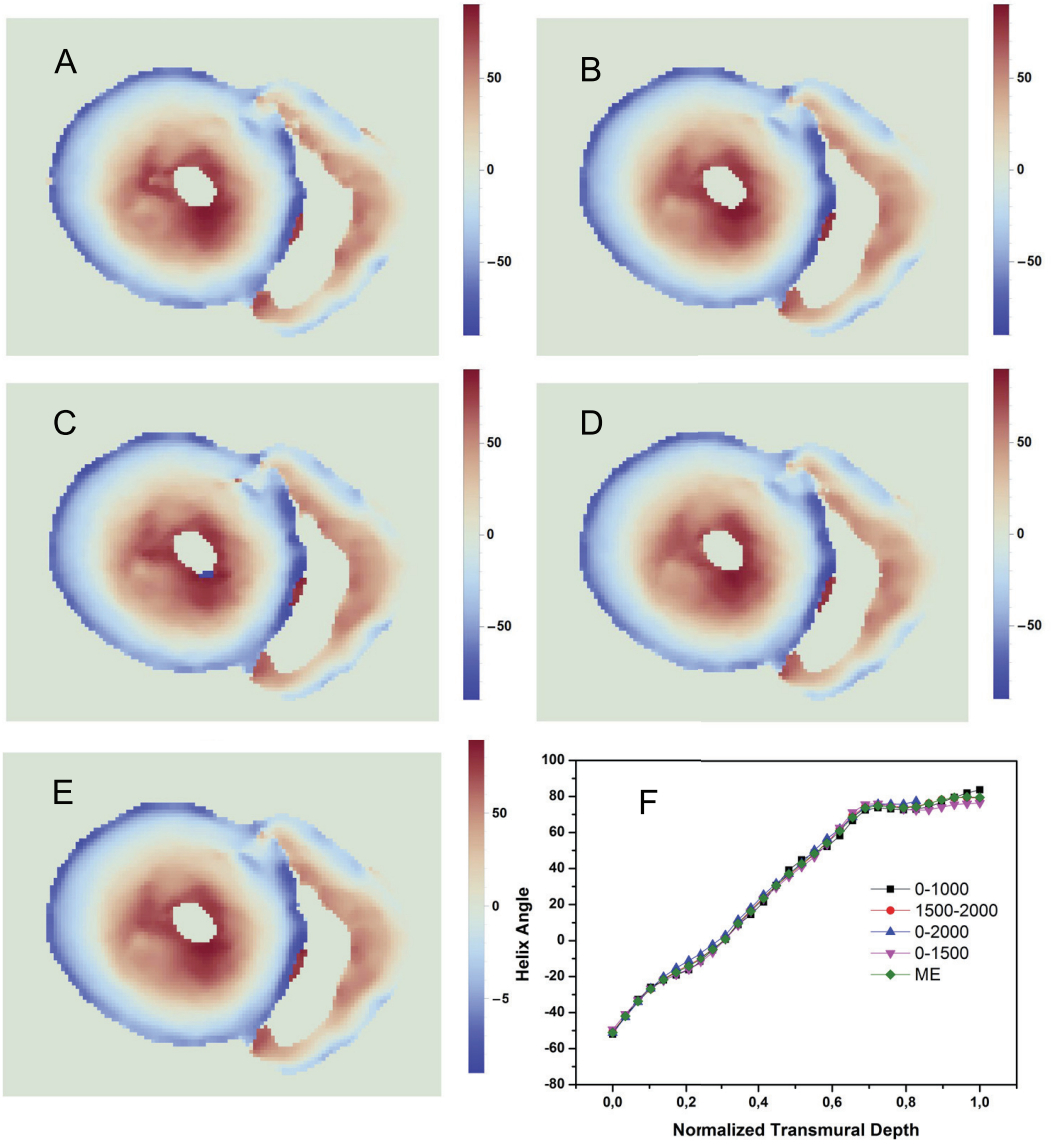

Figure 6.6: Helix angle derived from the first eigenvector of different tensors. **A)** to **E)** helix angle map for a slice in the mid-ventricular region calculated from DTI fitting for different shells (b=0-1000 s/mm^2, b=0-1500 s/mm^2, b=0-2000 s/mm^2, b=1500-2000 s/mm^2 and mono-exponential fitting). **F)** Scatter plot of the helix angle as a function of the normalized transmural depth in the septal region.

from DTI tensor. The difference in the values indicates that directional diffusivity derived from the mono-exponential DTI fitting reflects the combined effect of Gaussian and non-Gaussian diffusion displacement.

The deviation of the diffusion displacement profile from a Gaussian shape is more pronounced in the radial direction than in the axial direction of fiber orientation. In particular, by looking at the maps of kurtosis along a given direction, contrast can be appreciated between the left and the right ventricle, which is not observed in the eigenvalues

maps. The difference in kurtosis between the right and the left ventricle also shows that the ADC provides little indication of the specific biophysical mechanism contributing to signal decay in a diffusion MRI experiment. From this point of view, kurtosis can be a better tool to investigate cardiac tissue microstructure, since it provides more insight into small length-scales and is a relatively robust method when compared to bi-exponential fitting [33].

The differences in kurtosis between right and left ventricle could be explained by a decreased cellularity level in the right ventricle with respect to the left one. It is in fact reasonable that the right ventricle is characterized by an increased cellularity, since the resistance to the outflowing blood provided by the systemic circulation is much larger than the one from the respiratory circulation. However the differences in diffusion kurtosis profiles can be both explained with an increase in cellular volume (bigger cells) or an increase in the ratio between cellular and extracellular volume. The latter hypothesis could be experimentally verified by investigating the possible multi-exponential T_2-decay in the tissue. In fact, if the ratio between intracellular and extracellular space is decreased in the right ventricle, a more pronounced multi-exponential T_2 decay is to be expected. This experiment was however not performed. As an indication for future research, UTE mapping could be performed and compared to the kurtosis maps in order to investigate the correlation between compartmentalization of diffusion and T_2 decay.

The general bigger kurtosis value along the radial direction is in agreement with results of chapter 5. In fact it was already speculated that the diffusion along the radial direction is always restricted for b-values and diffusion times achievable with a clinical scanner, while the axial direction shows more the effects of high hindrance or restriction as a function of increasing mixing time. The high positive value of kurtosis along the radial direction can be then considered as an indication of restricted diffusion. On the other hand for the axial direction, where restricted and hindered diffusion coexist, a smaller deviation from a Gaussian slope is to be expected, and this is indeed observed in experimental data.

It is important to stress that the kurtosis coefficients, like the diffusion coefficients, are apparent, in the sense that they depend on the experimental diffusion time and b-values used. A general decrease of kurtosis along a given direction is to be expected for increasing diffusion times, reflecting the different diffusion regimes at different time scales. Also the b-value is expected to play an influence. Thus it could be interesting to perform DKI experiments in which both the experimental b-value and diffusion time are changed and study their influence on derived kurtosis parameters.

Like the diffusion coefficients, also the kurtosis coefficients can be misestimated as a consequence of imaging noise. To the best of my knowledge no studies have been performed in order to asses the role of changing SNR in the accuracy of kurtosis estimation. Although the SNR calculated from the non-diffusion weighted images after denoising resulted to be 72 ± 6, which is a high value in the framework of muscle DTI, the presence of a bias in kurtosis determination due to noise cannot be completely excluded.

A limitation of the kurtosis analysis approach used in this section is the assumption that radial kurtosis is a good measure of kurtosis in the two directions perpendicular to the axis of the cell. This was done following the approach commonly used in DKI of the brain, in which kurtosis values along the second and third eigenvectors are not presented

separately, but only as an average over the plane spanned by the two vectors (radial kurtosis). In this way differences between K_2 and K_3 are neglected. This assumption can be well justified in brain imaging since the second and third eigenvectors do not correlate to any specific cellular structure. In this case it can also be reasonable to assume that analyzing kurtosis along these two distinct directions does not provide extra information. On the other hand, in cardiac DTI it was already shown that the second eigenvector correlates with the direction parallel to myolaminar sheets, while the third one indicates the direction perpendicular to myolaminae. Due to the different information indicated by λ_2 and λ_3 in cardiac muscles, it can probably be more meaningful to study K_1 and K_2 separately.

The tensor analysis of data acquired with different b-values and constant diffusion time showed a clear dependence of the parameters derived from the tensors on the combination of b-values used in the calculation.
The general trend of decrease of all the DTI-derived parameters as a function of b-value is a clear indication of non mono-exponential decay and can be explained by the presence of a "slow" and a "fast" component of diffusion, as already discussed in chapter 5. Since the non mono-exponential signal decay as a function of the applied diffusion encoding is normally only visible at intermediate b-values ($\sim 1000\ s/mm^2$, depending on the diffusion time of the DW experiment) we can consider the signal attenuation between b=0 s/mm^2 and b=1000 s/mm^2 to reflect the fast diffusion component, and the signal attenuation between b=1500 s/mm^2 and b=2000 s/mm^2 to reflect the slow component of diffusion. This probably is a meaningful assumption, since if we compare figure 6.1 and 6.5, the apparent diffusion coefficients calculated from the kurtosis tensor are almost equal to the parameters calculated from the DTI fitting in the first shell. When comparing the diffusion parameters obtained from the first and forth tensor, a decrease of approximately 30% is observed for the diffusion coefficient along the fiber direction (first eigenvalue), while the radial diffusivity decreased by approximately 40%. This causes a substantial increase of the anisotropy level (27%) in the slow component when compared to the fast component. This is in disagreement with typical diffusion behavior described by the "ball and stick" model in brain tissue, in which the fast component (usually attributed to intra-axonal water) is strongly anisotropic, while the slow component (extracellular space) is almost isotropic [6]. Another important effect to notice is the similarity of the ADC parameters between the 0-1500 shell and the mono-exponential fitting (ME) of the data, indicating that the slow dephasing component is not taken into account when DTI fitting is performed for moderate b-value, such those applied in clinical research. However it could be interesting to focus investigation on the effect of probing slow component of diffusion, since its increased FA value with respect to the fast component could be beneficial for fiber tractography using higher order approaches (such as HARDI).
Another interesting aspect to analyze about the "fast" and "slow" component of diffusion as described by DTI fitting of the shells 0-1000 and 1500-2000 is the contrast present in the latter shell between right and left ventricle along the radial direction. If we hypothesize that in the range 1500/2000 s/mm^2 the spins belonging to the fast component are completely dephased, the smaller value of diffusion coefficient along the radial direction in the left ventricle could be seen to arise from water diffusing inside the cell and experiencing the restriction effects of z-discs. If the ratio between the extracellular and intracellular space is negligible in the left ventricle, all water displacement measured can be thought confined inside the cell. On the other hand, in the right ventricle, where the extracellular space volume is more significant, diffusion can occur both along the cell and in the extracellular matrix and the measured signal decay would reflect the combination of the two

phenomena. Since it is reasonable to hypothesize that diffusion in the extracellular space is less restricted than within the cell, this could be an explanation of the average increase in λ_1 in the right ventricle when compared to the left ventricle. The same reasoning can hold true for the radial components of diffusion as well.

In the maps of helix angles calculated from the principal eigenvectors of the five different tensors, no differences are shown between different b-value ranges. The fibers here are seen to have a smooth change in orientation from epicardium to endocardium, within an angular range of approximately 130 degrees, as already shown in previous DTI and histological studies. This confirms the hypothesis that the water molecules in the different compartments have an anisotropic displacement and that the principal direction of diffusion is parallel for both hindered and restricted diffusion behavior, as already suggested by the color-coded FA maps presented in chapter 5 for changing mixing times and b-values. The directions of fibers derived from the tensor model is then, within the investigated range, not dependent on the choice of diffusion encoding strength experimentally applied.

In conclusion, it was observed that the apparent fast and slow diffusion measurement by conventional DTI probe different microstructure information of cardiac tissue. The DTI-derived indices are shown to be dependent on the b-values used, suggesting that the optimal DTI acquisition protocol should be tuned according to the physiological target of the study.

6.4 Conclusions

In this chapter, an experimental protocol for Diffusion Kurtosis Imaging of the *ex-vivo* porcine heart was presented for the first time. Cardiac DKI looked to be feasible in a clinical scanner and to provide complementary information to the standard DTI model of diffusion. Significant contrast between the two ventricles was observed in all kurtosis maps, which was explained considering the differences in microstructure parameters between the left and the right ventricle.
Multitensor approach provided a further indication of the compartmentalization of water along the fiber direction, showing that DTI derived parameters strongly depend on the b-value range used in acquisition and that the diffusion experiment can be designed in order to probe the diffusion regime of interest.
Helix angle maps showed that the different compartments of diffusion along the cardiac cells are aligned, and that fiber tractography is not directly affected by the choice of experimental b-values.

Chapter 7

HARDI and DTI

In this section HARDI acquisition and reconstruction are implemented for the study of the *ex vivo* porcine heart. Reconstruction techniques (CSD and q-ball) are validated for a phantom of crossing fibers.

7.1 Phantom of crossing fibers

In order to assess the role of the different reconstruction algorithms in the quality of the resulting image and their ability to image crossing fibers within a voxel, a custom-made phantom of crossing wires was used. The interdigitating wires, crossing at an angle of approximately 60°, were enveloped in a rubber shell and placed in a plastic syringe completely filled with water [48].

7.1.1 Imaging

The MRI experiment on the phantom was conducted on a 9.4 T Bruker horizontal-bore MRI scanner. The syringe containing the phantom was inserted in a birdcage quadrature coil with the main axis of the syringe parallel to the coil axis. A standard 2D multislice spin echo DW sequence was used to acquire the images ($40 \times 40 \times 40$ mm FOV, TE=27.433 ms and TR=1355 ms) for the DTI and HARDI reconstruction. The image resolution was chosen to be isotropic (0.4 mm voxel size in x, y and z directions). The unipolar diffusion sensitizing gradients were placed symmetrically around the 180° radiofrequency pulse. Diffusion encoding was performed along 100 non-collinear directions equally spaced over the surface of a sphere. The b-value was set to $1400 s/mm^2$ (Δ=11 ms, δ=5ms). Furthermore 10 non-diffusion weighted images were also acquired for each dataset. The acquisition time for a single shell dataset was $\sim$ 15 hours
A T_1-weighted multislice sequence was also used, with double resolution to be used as a reference.

7.1.2 Data processing

The data were first pre-processed using DTITools. A Rician-noise suppression algorithm was applied to the images. By looping through the DW images at high frame rate, no evident signal dropouts and geometric distortions were found, so the computationally expensive and time consuming algorithm for image registration was not applied.
After the pre-processing step the data were exported to ExploreDTI[39] for DTI and HARDI calculation and fiber tractography.

The tensor was calculated from the data using a WLLS (Weighted Linear Least Squares) algorithm. In order to check the quality of the fitting to the diffusion tensor model, residuals were calculated. Since the residuals were observed to be low and the residuals map to be uniform, the data and their fitting were considered of good quality.
After tensor calculation, for each voxel the eigenvalues (λ_1, λ_2 and λ_3), mean diffusivity (MD) and fractional anisotropy (FA) were calculated.
For the CSD approach, the maximum harmonic degrees (L_{max}) of the estimated fibers were 2, 4, 6, 8 and 10. The response function was estimated from a ROI of 100 pixels drawn in one of the arms of the cross, where a single fiber population is known to be present ($FA = 0.56 \pm 0.05$). The FOD peak threshold was empirically determined in order to exclude the possibility of voxels with multiple fiber populations outside the central area of the phantom where fibers are crossing. The value of the peak threshold was set to 0.25 for L_{max} up to 8, and to 0.35 for $L_{max} = 10$. The QBI analysis was based on the spherical harmonics formalism and the value used was $L_{max} = 8$.
For the fiber tracking, seed points where spaced evenly with a 0.5 mm isotropic distribution. The predefined minimum and maximum tract length were 20 and 40 mm respectively. The tracts were stopped when a curvature of more than 20° was reached per 0.2 mm integration step. For DTI-based tractography fiber tracts were forced to continue for FA between 0.4 and 0.6.

7.1.3 Results

High-resolution T_1-weighted images of the phantom showed distinct intersecting wires orientation. The four regions of interest used for fiber tractography are indicated in figure 7.1.
In figure 7.2 a region of interest (ROI) located within the crossing fibre region is shown.

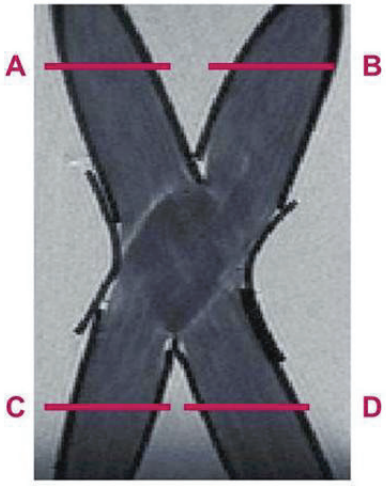

Figure 7.1: T_1 weighted image of the phantom of crossing fibers used as a reference. 4 regions of interest drawn in two axial slices of the phantom are indicated. Each ROI corresponds to a different arm of the cross.

For each method, the fODF (in the case of spherical deconvolution) or dODF (in the case of QBI) were estimated for each voxel in the ROI. The glyphs corresponding to the fODF were drawn for different L_{max}s by keeping all the estimation parameters constant and

changing the maximum spherical harmonics order. For each voxel the first eigenvector, estimated from DTI model, was also drawn. The first eigenvector of the diffusion tensor is parallel to the reconstructed glyphs in case of single fiber population (red glyphs) and approximately parallel to the sum of the two main peaks direction for multiple maxima ODF (green glyphs).

If we compare the glyphs drawn in figure 7.2 and the T_1 weighted image acquired along

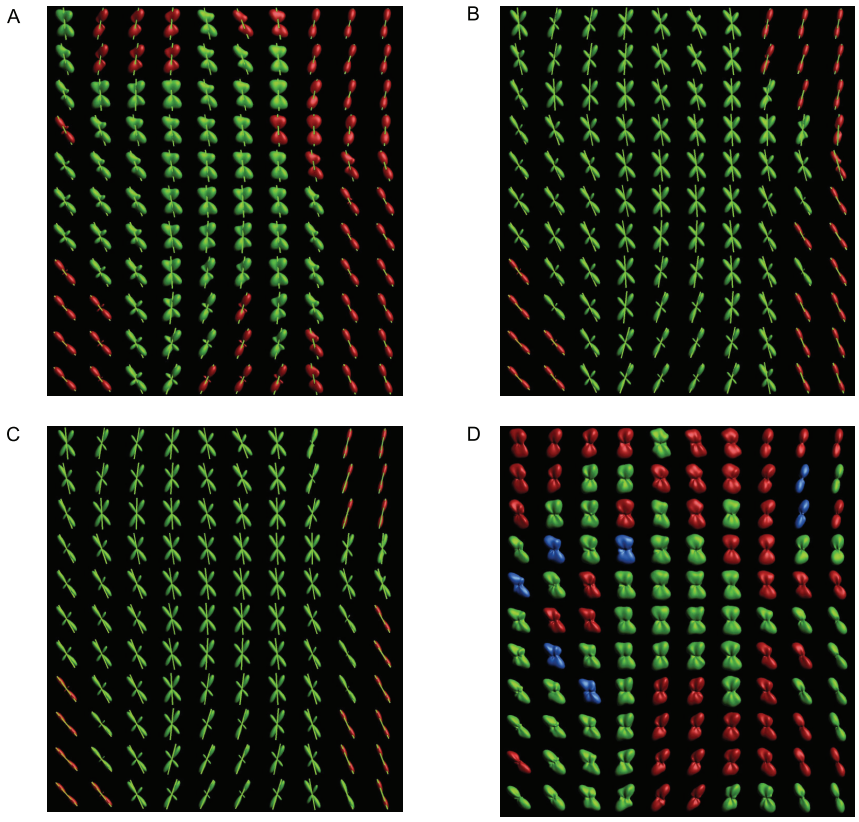

Figure 7.2: Region of crossing fiber of the phantom acquired for b=1400s/mm^2 reconstructed using CSD with different harmonics orders and QBI. Color coding in red, green and blue represents single fiber population, double fiber population and three fiber population respectively. The green lines superimposed to HARDI glyphs represent the direction of the first eigenvector as derived from DTI fitting of the dataset. **A)** CSD L_{max}=4. **B)** CSD L_{max}=6. **C)** CSD L_{max}=8. **D)** QBI L_{max}=6.

the same imaging plane, CSD reconstruction showed stellate patterns of ODF with their main orientation almost parallel to the known orientation of the crossing wires. In DTI, the first eigenvectors of the diffusion tensors is parallel to the wires in region of single fiber population. In the regions of crossing fibers, however, the first eigenvectors failed to align with either one of the intersecting capillaries.

The angular resolution of the ODF is shown to increase with the spherical harmonic order used. With L_{max}=6 the two peeks corresponding to the two fiber orientations can be already identified as distinct. The effect of increasing the harmonic order is to provide more sharply peaked maxima, both in regions of crossings and in regions of single fiber population. The data reconstructed with QBI are able to provide two local maxima which look comparable to the results obtained with CSD fitting, but the overall angular

resolution is low.
The results of fiber tractography of the complete phantom for the same dataset are shown in figure 7.3. Here 4 inclusive regions of interest were drawn and tracts were coded with different colors, according to the inclusive ROIs used.

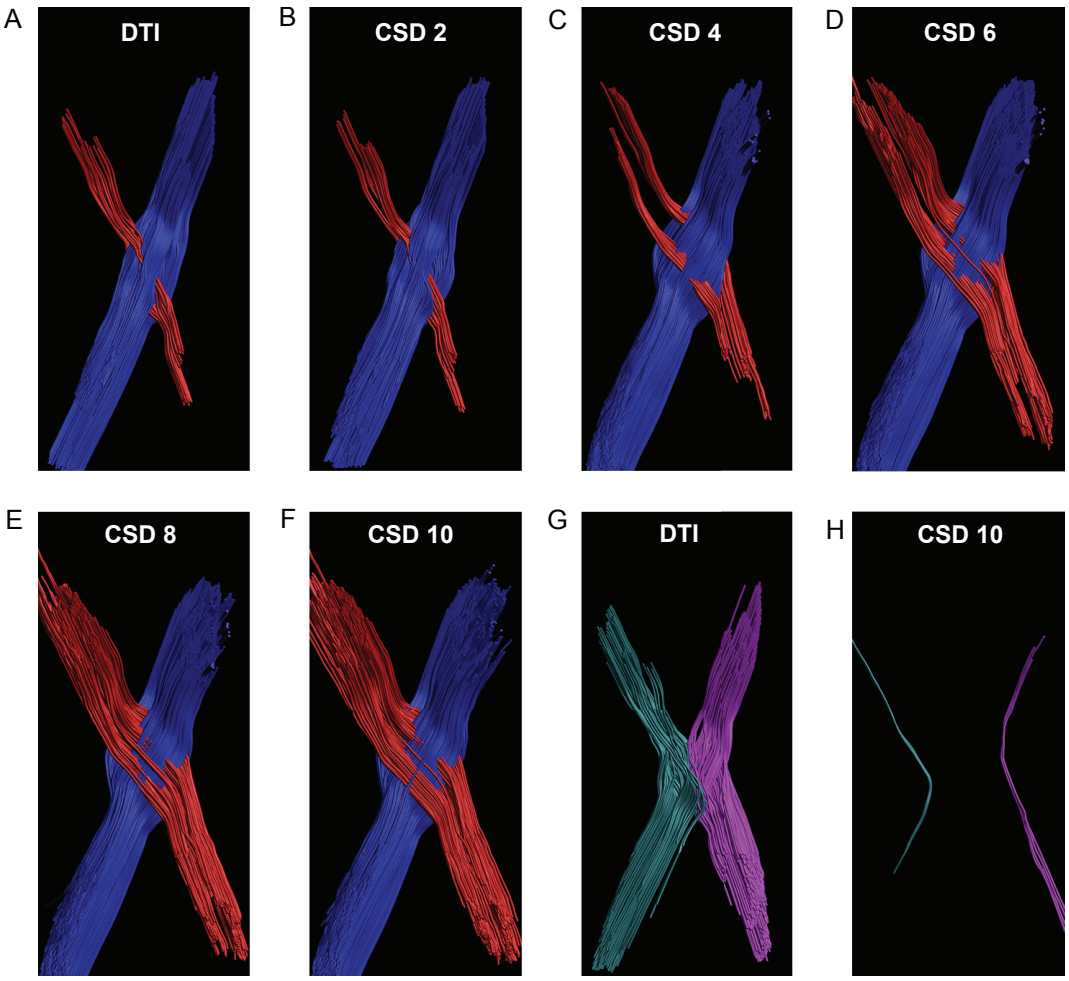

Figure 7.3: Fiber tracking of the complete phantom using DTI and CSD method for different spherical harmonics orders. **A)** to **F)** Red and blue represent fibers passing through the regions of interest A-D and B-C respectively. **A)** DTI. **B)** CSD L_{max}=2. **C)** CSD L_{max}=4. **D)** CSD L_{max}=6. **E)** CSD L_{max}=8. **F)** CSD L_{max}=10. In **G)** and **H)** light blue and purple represent fibers passing through the regions of interest A-C and B-D respectively. **G)** DTI. **H)** CSD L_{max}=10.

The number of tracts identified as crossing fibers is seen to increase for increasing harmonic order up to L_{max}=8 (fig:7.3A-F). Results obtained for L_{max}=10 are highly comparable to the ones obtained for L_{max}=8 both in terms of number of tracked fibers and visual appearance. In sub-figure G it can be observed that DTI fails to correctly describe the fiber orientation, and the reconstructed tracts are seen to be "kissing" but not intersecting each others. On the other hand, for CSD L_{max}=10 (sub-figure H) only few fibers are incorrectly identified as kissing, and all the tracts are seen to cross each others in the

central region of the phantom.

7.1.4 Discussion and conclusion

The CSD reconstruction algorithm was validated for a phantom of crossing fibers and fiber tractography was performed. The imaging parameters used looked to be suitable for HARDI reconstruction.
In the glyphs map of the central area of the phantom, QBI was observed to provide worse angular resolution than CSD for the same spherical harmonic order. For this reason QBI was not used for tractography and for HARDI reconstruction of the heart.
The CSD analysis of the data showed the presence of crossing fibers in the central area of the phantom, which were not correctly visualised by using a simple DTI data fitting. The angular resolution of the CSD glyphs obtained for the higher b-values was strongly dependent on the spherical harmonics order used, as is to be expected. The results obtained for L_{max}=10 were almost identical to results for L_{max}=8, but the peak selection threshold had to be set to an higher value in order to exclude spurious peaks in the reconstructed ODF. Since the increase in computation and acquisition time when going from L_{max}=8 to L_{max}=10 does not seem to be justified, this spherical harmonics order was not used for myocardium fiber tracking.
The images reconstructed with DTI and CSD L_{max}=2 present few tracts passing through ROI A and D. This is not to be expected, because the orientation distribution function reconstructed with both algorithms does not allow the presence of multiple maxima. However, since this spurious tracts bundle is observed to be the same for both reconstruction algorithms, it can be caused by non uniform arrangements of wires in the phantom and actually corresponds to an existing fiber configuration.

7.2 Ex vivo heart at 3 T

In this study the benefits of HARDI acquisitions protocols were investigated, and CSD and DTI tractography were performed.
The 5 complete porcine hearts were scanned at 3 T in order to identify the presence and location of regions of crossing fibers.

7.2.1 Imaging

The diffusion imaging acquisition was performed using a fat-suppressed multishot spin echo EPI sequence. Multishot EPI readout was used because it offers a good compromise between the T_2 losses and spatial distortion of single-shot EPI and the excessive scan time of a conventional spin echo acquisition. A variable number of slices without gaps oriented along the short axis view was used for the different scans, keeping the spatial resolution constant ($1 \times 1 \times 2\ mm^3$) in the phase, frequency and slice direction. Twice refocused diffusion encoding gradients were placed symmetrically around the 180° pulse to produce a b-value of 1000 s/mm^2. (Δ_1=53.60 ms, δ_1=11.47 ms, Δ_2=15.76 ms and δ_2=15.60 ms). Diffusion was encoded along a high number of non-collinear directions equally spaced over the surface of a sphere. The number of diffusion encoding directions was 70 (with 11 B_0 images) for the first heart and 100 (with 11 B_0 images) for heart number 2, 3, 4, and 5. The EPI factor was kept constant, while the number of signal averages was changed between 4 and 6 for the different scans in order to keep the acquisition time constant ($\sim$ 9.5 hours). Other acquisition parameters were TR/TE=5775/73.5 ms.

7.2.2 Data processing

The b-values used in the calculation of the diffusion parameters were 0 s/mm^2 for the non-diffusion weighted images and 1000 s/mm^2 for the diffusion weighted images (input values), since the contribution of crossing terms in the effective b-values was considered to be negligible for the acquisition parameters used.
For each dataset the diffusion tensor was calculated by using a WLLS algorithm. From the diffusion tensor, the three eigenvalues and the FA value were determined.
DTI and CSD fitting was performed for the complete heart. The maximum spherical harmonic order used for estimating the fiber orientation distribution function was L_{max}=6. For the estimation of the response function, it was assumed that the epicardium region of the free wall only shows single fiber population. For each dataset FA values were averaged in a ROI within this region and used for the estimation of the correct response function to be used for deconvolution. The peak threshold was fixed to 0.25. This value was empirically determined in order to exclude the possibility of spurious peaks due to noise within the cardiac chambers.
Fiber tractography was performed in some ROIs using both DTI and CSD. For both techniques, tracts were drawn with step size of 0.5 mm and were stopped when the curvature reached 20° per integration step. For FA based tractography, the tracts continued for FA between 0.1 and 0.5. Different minimum and maximum tract lengths were imposed. Since these parameters were changed for different images, they will be indicated in the results section for each figure.

7.2.3 Results

Visual inspection of the data showed good overall quality and no artifacts. In one dataset outliers were identified for images diffusion weighted along 7 encoding directions. These images were discarded before applying the denoising and the registration algorithm.
FA maps derived from the diffusion tensor showed a common pattern of enhanced FA in the region of the lateral wall, as can be observed in figure 7.4. This was empirically considered as an indication of the presence of single fiber population in that area. Therefore the response function for the CSD calculation was estimated from FA values in this area.

From the color coded maps a smooth change in fiber orientation can be seen within each heart, and similar color patterns can be appreciated for the different hearts.
CSD fitting was performed on the same datasets using $L_{max} = 6$. Glyphs representing the ODF are shown in figure 7.5 for the three different hearts presented in the previous picture. Glyphs are color coded according to the number of peaks of the corresponding ODF.

The images obtained for the different hearts show, within the inter-subject variability, similar patterns in terms of presence and locations of single fiber populations. Long axis views for the different hearts show clearly the presence of two populations of fibers crossing in the region of the free wall. In the short-axis views, double fiber population are generally present in the left ventricle, and in particular at the endocardium and in the midwall region. The epicardial region of the left ventricle and the right ventricle are observed to have only single fiber populations. Within the same heart, no significant differences in the distribution of the voxels characterized by crossing fibers is observed in the short axis view at different base-to-apex locations.
Fiber tractography was performed for the heart indicated by number 3 in figure 7.5.
Figure 7.6 shows fiber tractography in the mid ventricular slice. The maximum and min-

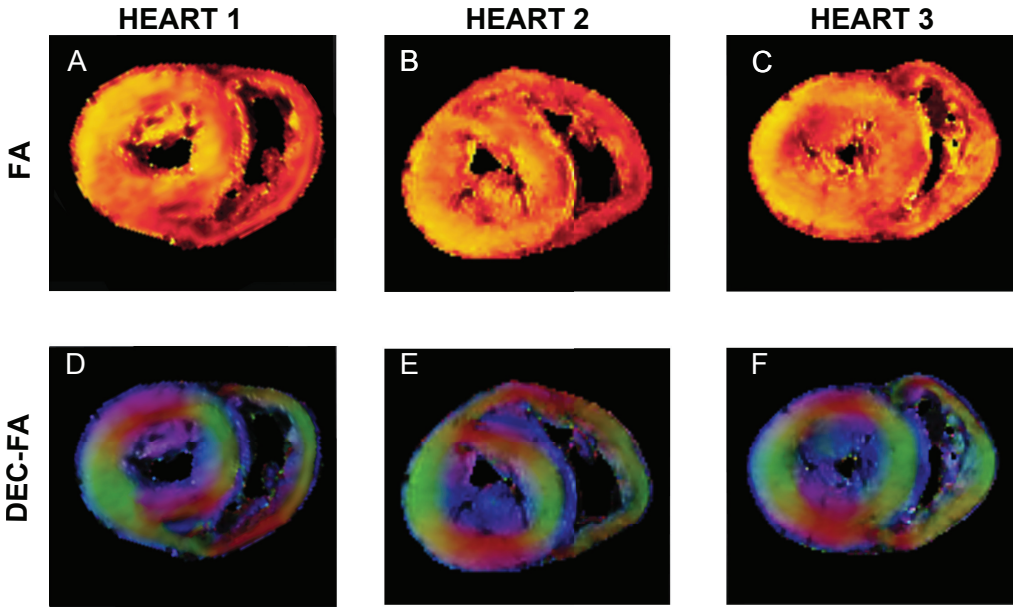

Figure 7.4: **A)** to **C)** FA maps and **D)** to **F)**color coded FA maps for three different hearts. Color coded maps indicate the orientation of the first eigenvector according to the standard color convention, where blue indicates in plane-out of plane, red indicates left-right direction and green indicates top-bottom direction.

imum tract lengths were fixed to 5 and 6 mm respectively. Images of fiber tractography obtained for CSD and DTI do not show significant differences in terms of fiber orientation. In both reconstructions the helical structure can be observed, with fibers running counterclockwise at the epicardium, almost in plane at the midwall and clockwise at the endocardium. Small differences can be observed in the epicardial region of the inferior wall.
In order to better appreciate the differences between DTI and CSD data fitting, magnifications of fiber tracts in these two regions is presented (see figure 7.7).
Green glyphs in the image represent voxels in which the ODF reconstructed with CSD present multiple maxima. As can be observed, fibers tracked with CSD present a second population of fibers at the endocardium, which is crossing the main population and that is not detected by using a DTI based approach.

7.3 Ex vivo heart at 9.4 T

In order to gain more insight into the fiber structure of the heart, additional experiments were performed on small heart specimens with higher resolution with a 9.4 T pre-clinical scanner.

7.3.1 Imaging

The MRI experiment on small heart specimens cut from heart 1 were conducted on a 9.4 T Bruker horizontal-bore MRI scanner. A standard 2D multislice multishot EPI sequence (6 segments) was used to acquire the images. The FOV was set to 30×40 mm^2, with a

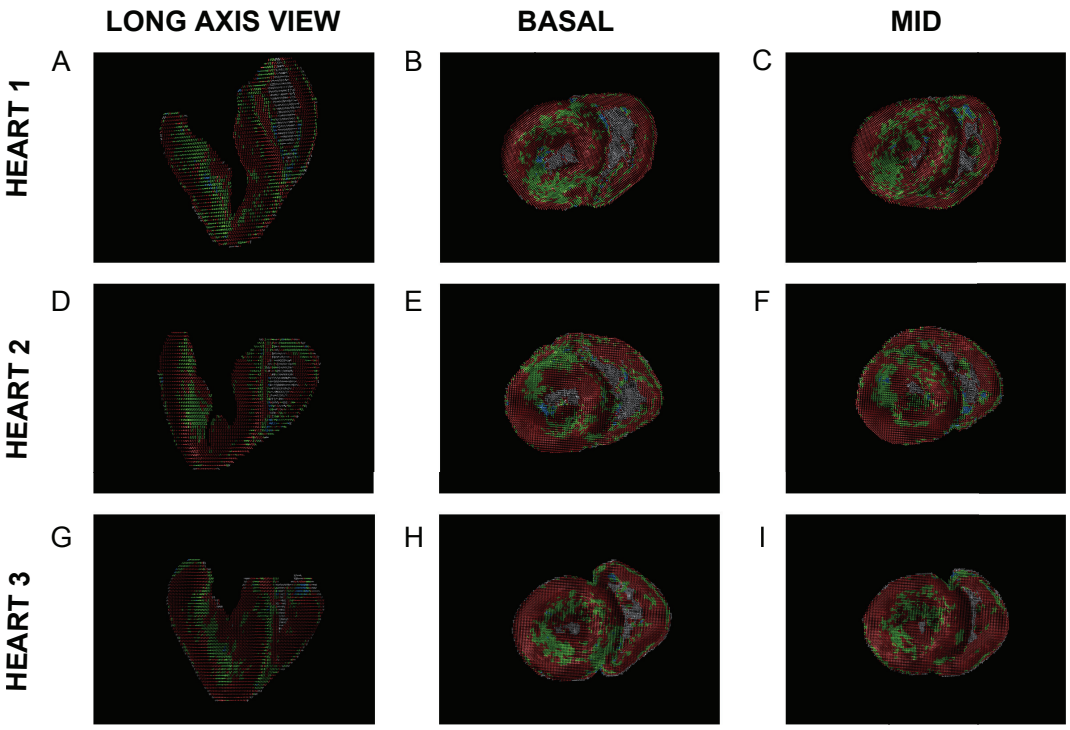

Figure 7.5: CSD glyphs calculated with L_{max}=6. Green glyphs and red glyphs represent double fiber and single fiber voxels respectively. Glyphs are presented for three different hearts in different slices. **A)**, **D)** and **G)** Long axis view. **B)**, **E)** and **H)** Basal slice. **C)**, **F)** and **I)** Mid-ventricular slice.

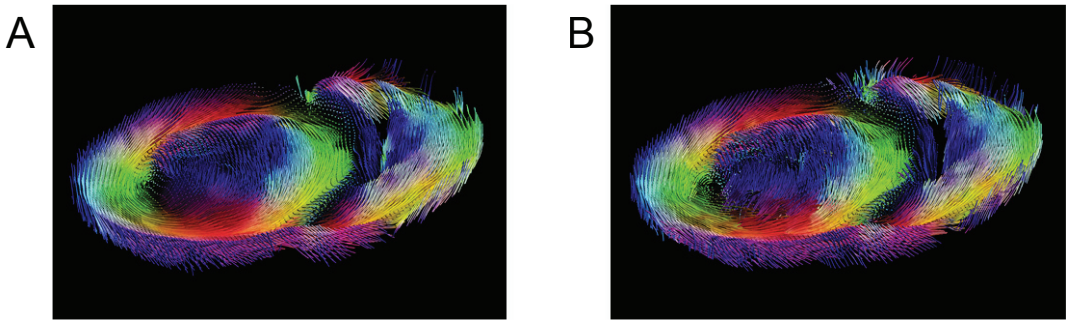

Figure 7.6: Fiber tractography of a mid ventricular slice of heart 3. **A)** DTI based tractography. **C)** CSD L_{max}=6 based tractography. Tracts are color coded according to the standard color convention.

matrix size of 60×80. A variable number of slices, without gaps, was acquired in order to cover the complete volume of the sample. The imaging parameters yielded a isotropic voxel resolution of 0.5×0.5×0.5 mm^2. A diffusion encoding module was applied using a standard Steijskal-Tanner sequence (Δ=8.5 ms and δ=4.5 ms), along 100 non-collinear directions equally spaced over the surface of a sphere. The b-value was set to 1500 s/mm^2. Other imaging parameters were TE=18.67 ms, TR=12500 ms and NSA=4. In addition to the 100 diffusion images, 16 non-diffusion weighted images were also acquired for each slice. The acquisition time for a single shell dataset was $\sim$ 9 hours

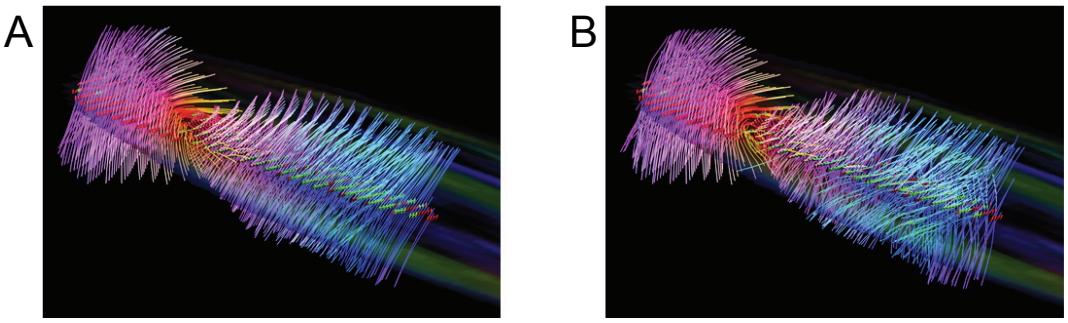

Figure 7.7: Fiber tractography in a ROI located in the inferior wall region of the mid ventricular slice of heart 3. **A)** DTI based tractography. **C)** CSD L_{max}=6 based tractography. Tracts are color coded according to the standard color convention.

7.3.2 Data processing

After denoising and image registration in Mathematica, the images were exported to ExploreDTI for HARDI calculation and fiber tractography. For HARDI based tractography, only the CSD approach was used, since q-ball didn't show satisfactory results in the phantom of crossing fibers (see section 7.1). DTI fitting was performed using a WLLS algorithm.
For each tissue sample, a ROI going from endocardium to epicardium in the short axis view was selected. For CSD and DTI fiber tractography seed point were spaced with 0.5 mm resolution. The predefined maximum and minimum value for fiber length was set to 10 and 15 mm respectively, and the tracts were stopped when a curvature grater than 20° per 1 mm integration step was reached. For DTI the tracts continued for FA values between 0.15 and 0.4. For CSD approach the response function was estimated for each dataset in a region of interest at the subepicardium. Since the subepicardial region in each dataset presented a higher FA value than in other locations, this was empirically considered as an indication of single fiber population in that area. The maximum spherical harmonics order used were 2, 4, 6 and 8. The peak threshold was empirically determined for each dataset in order to exclude spurious peaks. Fiber tracts and glyphs obtained using DTI and CSD with different spherical harmonics order were compared for each ROI.
The results presented in this section refer to a single scan of a sample of tissue cut from heart 1 in the region of inferior wall. For this specific dataset the FA value for estimation of the response function was set to 0.35 and the peak threshold was set to 0.25.

7.3.3 Results

The diffusion acquisition was evaluated for artifact and was considered of good quality. The residues maps of DTI fitting were uniform in all 3 image planes (x, y and z) and no outliers were shown. The SNR for the non diffusion weighted images was 35±4.
Analogously to the data acquired at 3 T, the epicardial region presented regions of enhanced anisotropy. Figure 7.8 shows FA and color coded FA maps of a block of tissue cut from inferior wall in its short axis and long axis view. Yellow areas represent regions in

which the FA value is larger than the mean value±standard deviation of FA values across the complete sample.

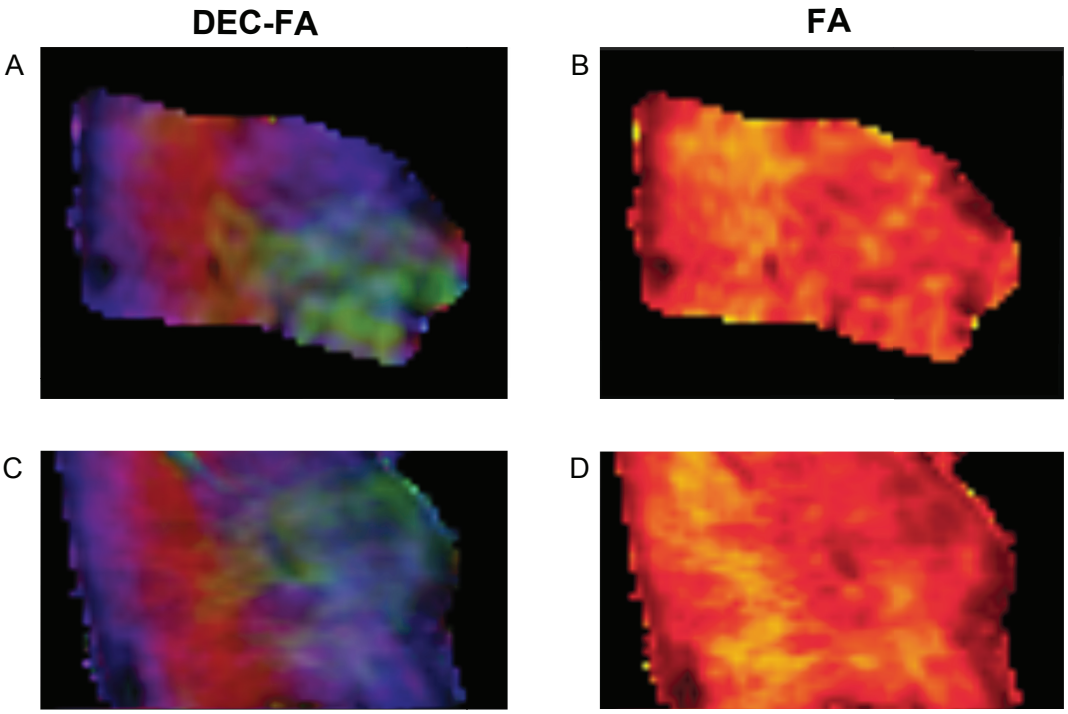

Figure 7.8: FA maps and color coded FA maps of a specimen of the inferior wall. **A)** and **B)** Short axis view. **C)** and **D)** Long axis view.

In order to investigate the differences between DTI and CSD at the level of a single voxel in regions in which single fiber population and double fiber population are expected, attention was focused on two small regions of interest located at the subendocardium and subepicardium respectively. In each voxel CSD and DTI glyphs were drawn. DTI glyphs are color coded according to their principal direction (red: up-down, green: left-right and blue: in-out). CSD glyphs were color coded in red for single fiber crossing the voxel, in green for 2 fibers and blue for three or more fibers. For each CSD glyph, the corresponding DTI glyph was also drown as a line for more immediate comparison of orientation (see figure 7.9).

In the epicardial region, where a single fiber population is expected, CSD and DTI provide similar results in terms of orientation and the well known helical orientation of fibers can be inferred. All the glyphs show in fact a smooth change in orientation from left handed helix to a more planar geometry in the midwall. The effects of increasing the spherical harmonics order is a progressive change from a "fat" glyphs towards a more elongated structure. Increasing the L_{max} has also the effect to increase the effect of noise, as can be seen form the two green glyphs in figure 7.9I.
On the other hand, in the endocardium region only DTI and CSD with L_{max}=2 provide similar results. For L_{max}=4 the angular spacing between two different peaks becomes evident and some of the glyphs are identified to represent a double fiber population. For L_{max}=6 and L_{max}=8 the glyphs show the presence of double fiber population in each

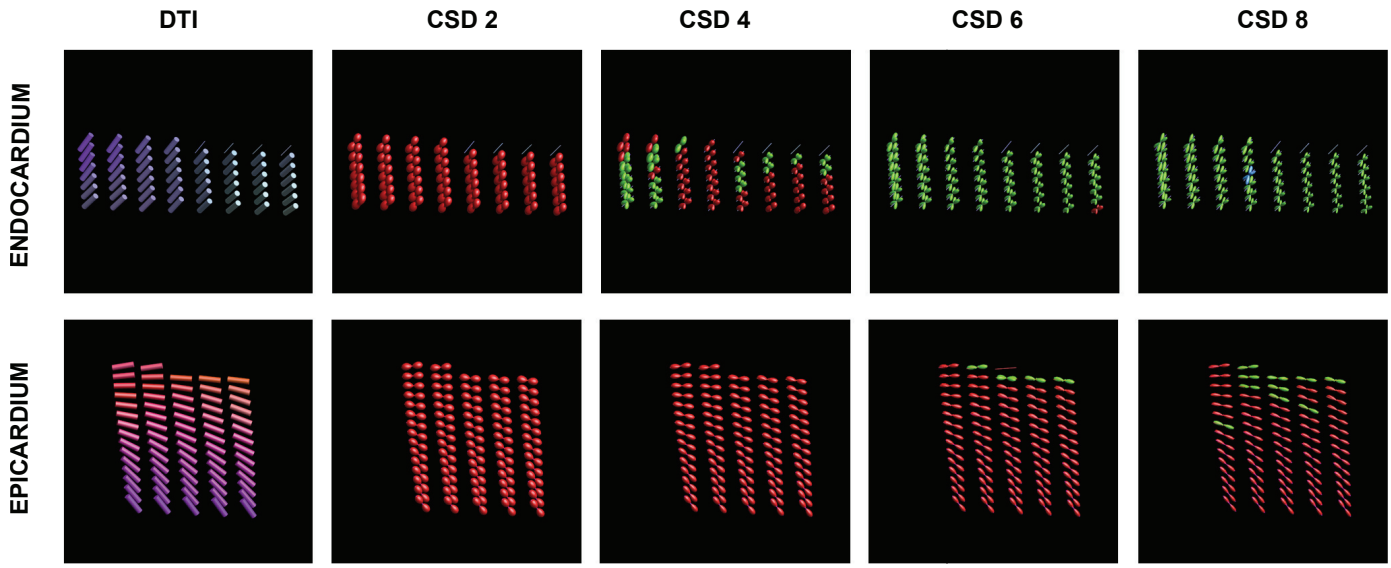

Figure 7.9: DTI and CSD glyphs in two different regions of interest located at the subepicardium and subendocardiun. **A)** and **F)** DTI cylinder glyphs. **B)** and **G)** CSD glyphs for L_{max}=2. **C)** and **H)** CSD glyphs for L_{max}=4. **D)** and **I)** CSD glyphs for L_{max}=6. **E)** and **L)** CSD glyphs for L_{max}=8.

voxels and the results between them are highly comparable. In both cases, the DTI glyphs appears to be located in between the two CSD peaks.
The results of fiber tractography with DTI and CSD (L_{max}=6 and L_{max}=8) for the region of interest going from epicardium to endocardium is shown in figure 7.10.
For DTI based tractography, the double helical organization of fibers can be observed in

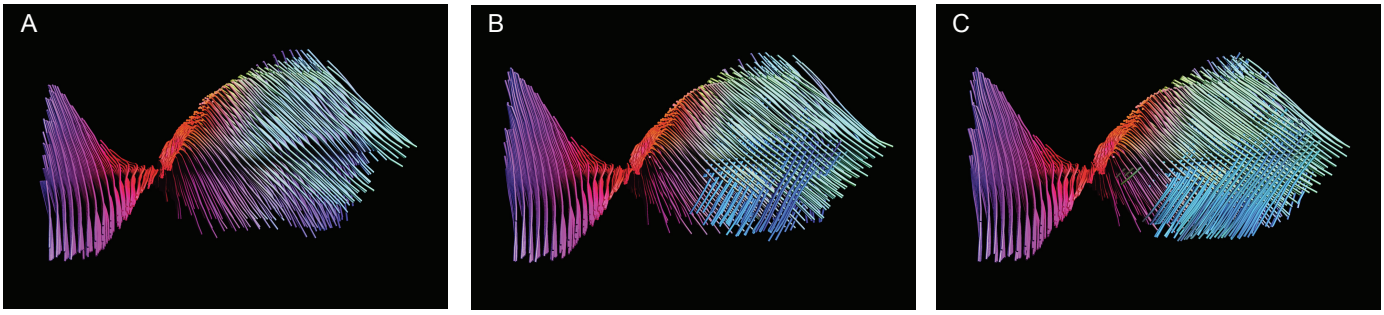

Figure 7.10: Fiber tracking in a region of interest in the inferior wall. **A)** DTI reconstruction. **B)** CSD L_{max}=6. **C)** CSD L_{max}=8.

great details, and all the fibers present a smooth change in orientation from endocardium to epicardium. On the other hand, for CSD-based tractography, a second population of fibers is observed in addition to the main population depicted by DTI. This second population of fibers crosses the main population with an angle of approximately 90°, creating a mesh-like structure. Regions of crossing are localized in the endocardial region, up to the midwall. In the epicardial region the results obtained from CSD and DTI are in agreement and both indicate the presence of a single fiber population. The results obtained for L_{max}=6 and L_{max}=8 look highly comparable in terms of number of tracked

fibers and angular spacing between them.

7.4 Discussion

In this section the implementation of Constrained Spherical Deconvolution in diffusion MRI of the *ex vivo* pig heart was presented. It was shown that the technique is able to resolve myocardial fiber architecture in the intact pig heart with a great level of details. The results obtained at 9.4 T from the same dataset for DTI and HARDI reconstruction algorithm in terms of fiber tracking were almost identical in the epicardial region of the LV, for every spherical harmonics order used. On the other hand, substantial differences were observed in the subendocardium region, in which double fiber population crossing at approximately 90° were tracked using the CSD approach.

For the data acquired at 9.4 T, the analysis of the Orientation Distribution Function, represented by the glyphs, shows that the order 2 and 4 spherical harmonics are unable to identify the location of crossing. For the order 2 this is indeed expected since the model has only 6 degrees of freedom (the same as DTI) and cannot show multiple maxima. For the higher spherical harmonics 6 and 8, the results looked extremely similar both at the single voxel level and in the fiber tractography. This would suggest that order 6 has to be preferred in this case, since it has less degrees of freedom and consequently the process on deconvolution is less susceptible to experimental noise. Furthermore, if less parameters have to be fitted, it could also be possible to encode diffusion along a reduced number of directions, and spend the acquisition time more conveniently on more image averages, in order to increase the SNR.

For the data acquired at 3 T for the complete hearts, the reconstructed CSD glyphs show the presence of double fiber population across the left ventricle wall in the region going from subendocardium to midwall. This is in agreement with the results shown for the small heart specimen acquired at 9.4 T. Fiber tractography performed in the region of inferior wall at 3 T and 9.4 T show comparable results, in fact in the left ventricle wall the presence of a secondary fiber population crossing the main population and creating a meshlike structure was observed for both acquisitions. However, the level of details in the reconstructed tracts and the tract density shows somehow worse results when compared to the results for the small heart specimen. In fact, while the main fiber population as depicted by DTI can be easily tracked using a CSD approach, the crossing tracts are observed to be much shorter. The differences in the density of tracked fibers can be attributed to the different spatial resolution used for the different scans and to the lower SNR of the data acquired at 3 T. In addition to that, another factor could explain the differences in the quality of the reconstructed tracts: the voxels of the data acquired at 3 T for the complete heart were not isotropic ($1\times1\times2\ mm^3$), while the resolution obtained at 9.4 T was $0.5\times0.5\times0.5\ mm^3$. In fact it has already been discussed that the use of isotropic voxel in fiber tractography is beneficial, in particular when HARDI and higher order techniques are applied and that non isotropic voxel resolution can introduce a bias in the tracked fibers using CSD approaches [32].

On the point of view of the MRI methods, the relatively high spatial resolution obtained allowed a good estimation of the fiber orientation for tractography and the characteristic helical structure of the myocytes was observed in great details. However this was done at expenses of acquisition time. This study however showed the feasibility of

CSD DW-MRI tracking of the *ex vivo* heart using a clinical system with relatively low b-value. The choice of b-value was based on empirical observation, and was mainly based on finding a tradeoff between a short TE and a strong enough diffusion encoding. The empirical b-value optimisation in this study was carried out by changing the gradient strength, leaving the diffusion time unchanged. However, since it was shown in chapter 5 that the FA value is bigger for longer diffusion time at constant b-value, an increase in mixing time could be beneficial in order to enhance differences in anisotropy level between single fiber and multiple fiber voxels.

On the point of view of the data processing, CSD method looked suitable for a good estimation of the fiber orientation distribution function and the crossings observed (both in terms of CSD glyphs and fiber tracts) correlate well with previous histological studies [35] and contrast enhanced MRI [18]. QBI reconstruction was not performed since it was shown for the phantom of crossing fibers that QBI performs worse than CSD for the same data. However it has to be observed that, while QBI is a relatively model free approach, CSD estimation is based on the assumption that changes in the observed FA scalar index in different locations of the heart are only caused by partial volume effects and that all the fibers share the same diffusion and structure characteristics. Different FA values were indeed observed as a function of transmural depth in the left ventricle both for small specimens at 9.4 T and for the complete heart at 3 T, as already reported by Jiang [29] for fixed sheep heart. In this study the enhanced FA in the subepicardial region of free wall was connected with the presence of a single fiber population. The absence of myolaminae in the subepicardial region of the free wall was already reported for the rat heart using confocal microscopy [47], so the hypotesis that the enhanced FA values in this area can connect with the presence of a single fiber population can be reasonable. Although this assumption may not hold true, the increased FA values in the epicardial region reflects true characteristics of the tissue and it is not only due to noise effects. It has already been discussed in fact that noise can cause higher artificial FA, and that the bias between the true and experimental value due to noise increases for lower true FA values [31]. In this case, the mid-myocardium and some epicardial regions exhibit lower FA value, and these regions should be theoretically more sensitive to the effect of noise. The region specific differences observed experimentally for FA across the wall are then likely a lower estimation of real FA differences and can be considered as a representation of the real tissue properties.
In general, this effect of enhanced FA in the epicardial region, could be explained by the existence of "complex" tissue structure, such as bifurcating myolaminae structures in the subendocardium, which would then allow the use of the CSD algorithm for processing the data. On the other hand, the decrease in FA at the endocardium can also reflect differences in myocyte organization in terms of different volumes between intracellular and extracellular space and or/differences in myocytes cross sections between endocardium and epicardium. The different workload of the internal part of cardiac wall compared to the external part could justify in fact the presence of an increased cellular density and/or with increased cross radius. A complete histological knowledge that would allow to explain the changes of FA with the presence of complex tissue structure or structural differences or a combination of both is however still lacking. Further research is needed in that sense to better evaluate the compatibility between the general cardiac structure and the assumptions underlying the CSD method.

Another important consideration is that the response function (RF) has a strong in-

fluence in the deconvolution process and then in determining the correct number of fibers crossing the voxel of interest, and this is particularly true when high order spherical harmonics are used. The RF is currently estimated through defining a FA value, below which the voxel contains double fiber population. An inaccurate calibration of the response function (RF), can lead to the detection of spurious fODF peaks which could than cause false positive in fiber tractography. In addiction to that, certain voxel could present low FA values, due to presence of membranes or other restriction effects, and the latter effect is especially present when high b-values are applied. The response function then heavily relies on the DTI model in general and on previous knowledge of the tissue of interest. Further research is needed in that sense in order to make the deconvolution process more robust and less dependent on user defined settings. Recursive approaches for the estimation of the response function, like the one proposed in [57] could be promising in that sense.

7.5 Conclusion

In this study CSD analysis and fiber tracking of the *ex vivo* pig heart were performed for the first time. The results show that CSD estimation is possible for diffusion MRI data acquired *ex vivo* using a clinical scanner with limited gradient strength. Furthermore it was also shown that the CSD fiber reconstruction offers an added value over conventional DTI, since it allows to identify crossing fiber structures that DTI fails to correctly describe. For high resolution data acquired at 9.4 T a mesh like pattern of crossing fiber was successfully identified in the subendocardium, in agreement with previous study performed using different imaging techniques. In the midwall and epicardium region the well know double helical fiber structure was observed in great detail due to the high spatial and angular resolution used.
Further work is needed in terms of optimization of acquisition parameters, such as number of directions and b-value used, and in a more robust deconvolution and response function estimation techniques. Nevertheless, the preliminary results obtained show that CSD may be suitable to obtain a better 3D characterization of the heart and get more insight into fiber and laminar anatomy.

Chapter 8

General conclusions and future work

In this work different Diffusion Weighted MRI acquisitions and different processing techniques were successfully applied to the study of the *ex vivo* porcine heart.
Different diffusion MRI approaches were used, providing information both at the local scale and on the gross anatomy in order to get a deeper understanding of cardiac (micro)structure. While technical discussions and some suggestions for future work were already discussed in the related experimental chapters, it is appropriate to make some general considerations.
Experimental results obtained at changing diffusion times and b-values showed that diffusion in cardiac tissue is more complicated than as simply described by the DTI model. It is in fact speculated that restriction effects and compartmentalization of water can play a role in the overall measured diffusion profile. Future work is needed in order to increase the range of investigated b-values and mixing times, and to try to incorporate the findings in a global model, that could allow to predict diffusion behaviors in normal cardiac tissue and also to better appreciate differences due to diseases and pathological conditions.
Since the *in vivo* implementation of most of the approaches presented in this thesis is not possible yet, further research has to focus *ex vivo* in order to establish under which assumptions and experimental conditions the Gaussian profile of diffusion described by DTI is a good approximation of the real diffusion profile. These investigations have to include different shells of b-values and different experimental diffusion times. Ideally the proposed model should also be used for numerical simulations.
Experiments also suggested that the dynamic of diffusion along the cells and perpendicular to them has a different behavior. While the effect of restrictions is more pronounced along the radial direction, as it was expected, also the axial component of diffusion is shown to depend on diffusion time and b-values used. Modelling of diffusion in cardiac tissue has to include this behavior, which for instance has never been observed in DW-MRI of white matter of the brain.
With regard to the evidence of restriction along the main direction of cardiac cell, it is of interest to investigate this behavior further. This could in fact be relevant for fiber tractography, that usually makes use only of the diffusion in radial direction. Further research should focus on optimization of acquisition and different fiber reconstruction techniques such as CSD (as preliminarily shown in this thesis) and multiple tensor approaches.
Although further studies will be required, fiber tractography with Diffusion MRI can be an extremely valuable tool in order to validate mechanical and electric conduction models of the heart, and higher order DW-MRI approaches can provide, under the correct assumptions, additional information to understand cardiac function and modelling.

Bibliography

[1] D. C. Alexander, G. J. Barker, and S. R. Arridge. Detection and Modeling of Non-Gaussian Apparent Diffusion Coefficient Profiles in Human Brain Data. *Magnetic Resonance in Medicine*, 48:331–340, 2002.

[2] D. C. Alexander and T. B. Dyrby. Compensation for bias from unwanted gradient contributions in STEAM diffusion MRI. In *20th Annual Meeting of Intl Soc Mag Reson Med*, page 1884, Melbourne, Australia, 2012.

[3] Y. Assaf and Y. Cohen. Non-Mono-Exponential Attenuation of Water and N-Acetyl Aspartate Signals due to Diffusion in Brain Tissue. *Journal of Magnetic Resonance*, 131:69–85, 1998.

[4] R. Bammer. Basic principles of diffusion-weighted imaging. *European Journal of Radiology*, 45:169–184, 2003.

[5] P. J. Basser and C. Pierpaoli. Microstructural and Physiological Features of Tissues Elucidated by Quantitative Diffusion Tensor MRI. *Journal of Magnetic Resonance*, 111:209–219, 1996.

[6] T. E. Behrens, M. W. Woolrich, M. Jenkinson, H. Johansen-Berg, R. G. Nunes, S. Clare, P. M. Matthews, J. M. Brady, and S. M. Smith. Characterization ad Propagation of Uncertainty in Diffusion-Weighted MR Imaging. *Magnetic Resonance in Medicine*, 50:1077–1088, 2003.

[7] V. Callot, E. Bennet, U. K. M. Decking, R. Balaban, and H. Wen. In Vivo Study of Microcirculation in Canine Myocardium Using the IVIM Method. *Magnetic Resonance in Medicine*, 50(3):531–540, 2003.

[8] D. Chandler. *Introduction to Modern Statistical Mechanics*. Oxford University Press, 1987.

[9] L. C. Chang, D. K. Jones, and C. Pierpaoli. RESTORE: Robust Estimation of Tensors by Outlier Rejection. *Magnetic Resonance in Medicine*, 53:1088–1095, 2005.

[10] J. Chen, W. Liu, H. Zhang, L. Lacy, X. Yang, S.-K. Song, S. A. Wickline, and X. Yu. Regional ventricular wall thickening reflects changes in cardiac fiber and sheet structure during contraction: quantification with diffusion tensor MRI. *Am J Physiol Heart Circ Physiol*, 289:H1898–H1907, 2005.

[11] C. Coghlan and J. Hoffman. Leonardo da Vinci's flights of the mind must continue: cardiac architecture and the fundamental relation of form and function revisited. *European Journal of Cardio-thoracic Surgery*, 29S:S4–S17, 2006.

[12] B. M. Delattre, M. Viallon, H. Wei, Y. Zhu, V. M. Pai, H. Wen, and P. Croisille. Intravoxel Incoherent Motion applied to Cardiac diffusion weighted MRI using breathhold acquisition in healthy volunteers. *Journal of Cardiovascular Magnetic Resonance*, 14 (Suppl 1):P261, 2012.

[13] A. Einstein. On the motion required by the molecular kinetic theory of heat of small particles suspended in a stationary liquid. *Annalen der Physik*, 17:549, 1905.

[14] D. B. Ennis and G. Kindlmann. Orthogonal Tensor Invariants and the Analysis of Diffusion Tensor Magnetic Resonance Imaging. *Magnetic Resonance in Medicine*, 55:136–146, 2006.

[15] J. R. Forder, J. D. Bui, D. L. Buckley, and S. J. Blackband. MR imaging of water measurement of compartmental water diffusion in perfused heart slices. *Am J Physiol Heart Circ Physiol*, 281(3):1280–1285, 2003.

[16] M. Froeling. *DTI of human skeletal muscle. From simulation to clinical implementation.* PhD thesis, Biomedical NMR, Department of Biomedical Engeneering, Eindhoven University of Technology, October 2012.

[17] M. Froeling, A. J. Nederveen, K. Nicolay, and G. J. Strijkers. DTI of human skeletal muscle: the effects of diffusion encoding parameters, signal-to-noise ratio and T2 on tensor indices and fiber tracts. *NMR in Biomed*, 2013.

[18] S. H. Gilbert, D. Benoist, A. P. Benson, E. White, S. F. Tanner, A. V. Holden, H. Dobrzynski, O. Bernus, and A. Radjenovic. Visualization and quantification of whole rat heart laminar structure using high-spatial resolution contrast-enhanced MRI. *Am J Physiol Heart Circ Physiol*, 302:H287–H298, 2012.

[19] S. H. Gilbert, A. P. Benson, and A. V. Holden. Regional localisation of left ventricular sheet structure: integration with current models of cardiac fibre, sheet and band structure. *European Journal of Cardio-thoracic Surgery*, 17:231–249, 2007.

[20] R. P. Grant. Notes on the Muscular Architecture of the Left Ventricle. *Circulation*, 32:301–308, 1965.

[21] P. Hagmann, L. Jonasson, P. Maeder, J.-P. Thiran, V. J. Weeden, and R. Meuli. Understanding Diffusion MR Imaging Techniques: From Scalar Diffusion-weighted Imaging to Diffusion Tensor Imaging and Beyond. *RadioGraphics*, 26:S205–S223, 2006.

[22] P. Helm, M. F. Beg, M. I. Miller, and R. R. Winslow. Measuring and mapping Cardiac Fiber and Laminar Architecture Using Diffusion Tensor MRI Imaging. *Ann. N. Y. Acad. Sci.*, 1047:296–307, 2005.

[23] P. A. Helm, H.-J. Tseng, L. Younes, E. R. McVeigh, and R. L. Winslow. Ex Vivo 3D Diffusion Tensor Imaging and Quantification of Cardiac Laminar Structure. *Magnetic Resonance in Medicine*, 54:850–859, 2005.

[24] M. Holz, S. R. Heil, and A. Sacco. Temperature-dependent self-diffusion coefficient of water and six selected molecular liquids for calibration in accurate 1H NMR PFG measurements. *Phys. Chem. Chem. Phys.*, 2:4740–4742, 2000.

[25] E. W. Hsu, D. L. Buckley, J. D. Bui, S. J. Blackband, and J. R. Forder. Two-Component Diffusion Tensor MRI of Isolated Perfused Hearts. *Magnetic Resonance in Medicine*, 45:1039–1045, 2001.

[26] E. W. Hsu, A. L. Muzikant, M. S. A, P. R. C, and C. S. Henriquez. Magnetic resonance myocardial fiber-orientation mapping with direct histological correlation. *Am J Physiol Heart Circ Physiol*, 274:H1627–H1634, 1998.

[27] J. H. Jensen and J. A. Helpern. MRI Quantification of Non-Gaussin Water Diffusion by Kurtosis Analysis. *NMR Biomed*, 23(7):698–710, 2010.

[28] J. H. Jensen, J. A. Helpern, A. Romani, H. Lu, and K. Kaczynski. Diffusional Kurtosis Imaging: The Quantification of Non-Gaussian water Diffusion by means of Magnetic Resonance Imaging. *Magnetic Resonance in Medicine*, 53:1432–1440, 2005.

[29] Y. Jiang, K. Pandya, O. Smithies, and E. W. Hsu. Three-Dimensional Diffusion Tensor Microscopy of Fixed Mouse Hearts . *Magnetic Resonance in Medicine*, 52:453–460, 2004.

[30] D. K. Jones. *Diffusion MRI: Theory, Methods and Application.* Oxford University Press, 2010.

[31] D. K. Jones and M. Cercignani. Twenty-five Pitfalls in the Analysis of Diffusion MRI Data. *NMR Biomed*, 23:803–820, 2010.

[32] D. K. Jones, T. R. Knösche, and R. Turner. White matter integrity, fiber count, and other fallacies: The do's and don'ts of diffusion MRI. *NeuroImage*, 73:239–254, 2013.

[33] V. G. Kiselev and K. A. Il'yasov. Is the "Biexponential Diffusion" Biexponential? *Magnetic Resonance in Medicine*, 57:464–469, 2007.

[34] P. W. Kuchel, G. Page, K. Nagashima, S. Velan, V. Vijayaragavan, V. Nagarajan, and K. H. Chuang. Steiskal-Tanner Equation Derived in Full. *Concepts in Magnetic Resonance Part A*, 40A(5):205–214, 2012.

[35] G. L. Kung, T. C. Nguyen, A. Itoh, S. Skare, I. N. B, D. Craig Miller, and D. B. Ennis. The presence of two local myocardial sheet populations confirmed by diffusion tensor MRI and histological validation. *Journal of Magnetic Resonance Imaging*, 34:1080–1091, 2011.

[36] L.-W. Kuo, J.-H. Chen, V. J. Weeden, and W.-Y. I. Tseng. Optimization of diffusion spectrum imaging and q-ball imaging on clinical system. *NeuroImage*, 41:7–18, 2008.

[37] D. Le Bihan, E. Breton, D. Lallemand, P. Grenier, E. Cabanis, and M. Laval-Jeantet. MR imaging of Introvoxel Inchorent Motions: Application to Diffusion and Perfusion in Neurologic Disorders. *Radiology*, 161:401–407, 1986.

[38] J.-H. Lee and C. S. Springer. Effects of Equilibrium Exchange on Diffusion-Weighted NMR Signals: The Diffusigraphic Shutter-Speed. *Magetic Resonance in Medicine*, 49:450–458, 2003.

[39] A. Leemans, B. Jeurissen, J. Sijbers, and D. Jones. ExploreDTI: a graphical toolbox for processing, analyzing, and visualizing diffusion MR data. In *17th Annual Meeting of Intl Soc Mag Reson Med*, page 3537, Hawaii, USA, 2009.

[40] I. J. LeGrice, B. H. Smaill, L. Z. Chai, S. G. Edgar, J. B. Gavin, and P. J. Hunter. Laminar structure of the heart: ventricular myocyte arrangement and connective tissue architecture in the dog. *Am. J. Physiol.*, 269:H571–H585, 1995.

[41] J. Mattiello, P. J. Basser, and D. LeBihan. Analytical Expression for the b Matrix in NMR Diffusion Imaging and Spectroscopy. *Journal of Magnetic Resonance*, 108:131–141, 1994.

[42] C. Mekkaoui, S. Huang, H. H. Chen, G. Dai, t. reese, W. J. Kostis, A. Thiagalingam, P. Maurovich-Horvat, J. N. Ruskin, U. Hoffmann, M. P. Jackowski, and D. E. Sosnovik. Fiber architecture in remodeled myocardium revealed with a quantitative diffusion CMR tractography framework and histological validation. *Journal of Cardiovascular Magnetic Resonance*, 14:70, 2012.

[43] P. P. Mitra and B. I. Halperin. Effects of finite gradient pulse width in pulsed field gradients diffusion measurements. *J Magn Reson*, 113:94–101, 1995.

[44] S. Nielles-Vallespin, C. Mekkaoui, P. Gatehouse, T. G. Reese, J. Keegan, P. F. Ferreira, S. Collins, P. Speier, T. Feiweier, R. de Silva, M. P. Jackowsky, D. Pennell, D. E. Sosnovick, and D. Firmin. In Vivo Diffusion Tensor MRI of the Human Heart: Reproducibility of Breath-Hold and Navigator-Based Approaches. *Magnetic Resosnance in Medicine*, 70:454–465, 2013.

[45] M. Nilsson, J. Latt, E. Nordh, R. Wirestam, F. Stahlberg, and S. Brockstedt. On the effects of a varied diffusion time in vivo: is the diffusion in white matter restricted? *Magn Reson Imaging*, 27(2):176–187, 2009.

[46] V. Patel, I. D. Dinov, J. D. Van Horn, P. M. Thompson, and T. A. W. LONI MiND: metadata in NIfTI for DWI. *Neuroimage*, 51(2):665–676, 2010.

[47] A. J. Pope, G. B. Sands, B. H. Smaill, and I. J. LeGrice. Three-dimensional Transmural Organization of Perimysial Collagen in the Heart. *Am J Physiol Heart Circ Physiol*, 295:H1243–H1252, 2008.

[48] P. Pullens, A. Roebroeck, and R. Goebel. Ground Truth Hardware Phantoms for Validation of Diffusion-Weighted MRI Applications. *Journal of Magnetic Resonance Imaging*, 32:482–488, 2010.

[49] S. B. Reeder, B. J. Wintersperger, O. Dietrich, T. Lanz, A. Greiser, M. F. Reiser, G. M. Glazer, and S. O. Schoenberg. Practical approaches to the evaluation of signal-to-noise ratio performance with parallel imaging: application with cardiac imaging and a 32-channel cardiac coil. *Magnetic Resonance in Medicine*, 54(3):748–754, 2005.

[50] D. F. Scollan, A. Holmes, R. Winslow, and J. Forder. Histological validation of myocardial microstructure obtained from diffusion tensor magnetic resonance imaging. *Am J Physiol Heart Circ Physiol*, 274:H2308–H2318, 1998.

[51] D. E. Sosnovic, R. Wang, G. Dai, T. G. Reede, and W. V. J. Diffusion MR tractography of the heart. *Journal of Cardiovascular Magnetic Resonance*, 11:47, 2009.

[52] D. E. Sosnovic, R. Wang, G. Dai, T. Wang, E. Aikawa, M. Novikov, A. Rosenzweig, R. J. Gilbert, and V. J. Weeden. Diffusion Spectrum MRI tractography Reaveals the Presence of a Complex Network of residual Myofibers in Infarcted Myocardium. *Circ Cardiovascular Imaging*, 2:206–212, 2009.

[53] E. O. Stejskal and J. E. Tanner. Spin Diffusion Measurements: Spin Echoes in the Presence of a Time Dependent Field Gradient. *J. Chem. Phys.*, 42(1):288–292, 1965.

[54] G. J. Strijkers, A. Bouts, W. M. Blankesteijn, T. H. J. M. Peeters, A. Vilanova, M. C. van Proijen, H. M. H. F. Sanders, E. Heijman, and K. Nicolay. Diffusion tensor imaging of left ventricular remodeling in response to myocardial infarction in the mouse. *NMR Biomed.*, 22:182–190, 2009.

[55] K. Sungheon, G. Chi-Fishman, A. S. Barnett, and C. Pierpaoli. Dependence on Diffusion Time of Apparent Diffusion Tensor of Ex-Vivo Calf Tongue and Heart. *Magnetic Resonance in Medicine*, 54:1387–1396, 2005.

[56] J. E. Tanner. Use of the Stimulated Echo in NMR Diffusion Studies. *J. Chem. Phys.*, 52:2523, 1970.

[57] C. M. W. Tax, B. Jeurissen, S. B. Vos, M. A. Viergever, and A. Leemans. Recursive calibration of the fiber response function for spherical deconvolution of diffusion MRI data. *NeuroImage*, 2013.

[58] I. Teh, M. Lohezic, D. Aksentijevic, and J. E. Schneider. Accelerated fast spin echo diffusion spectrum imaging in the mouse heart ex-vivo. *Journal of Cardiovascular Magnetic Resonance*, 15(Suppl 1):W6, 2013.

[59] F. Torrent Guasp, M. Ballester, G. D. Buckberg, f. Carreras, A. Flotats, I. Carrio, L. E. Samuels, and J. Narula. Spatial orientation of the ventricular muscle band: Physiologic contribution and surgical implications . *J Thorac Cardiovasc Surg 2001*, 122:389–392, 2001.

[60] H. C. Torrey. Bloch equation with diffusing terms. *Phys Rev*, 104:563–565, 1956.

[61] J. D. Tournier and F. Calamante. Direct estimation of the fiber orientation density function from diffusion-weighted MRI data using spherical deconvolution. *NeuroImage*, 23:1176–1185, 2004.

[62] J. D. Tournier, F. Calamante, and A. Connelly. Robust determination of the fiber orientation distribution in diffusion MRI: non-negativity constrained super-resolved spherical deconvolution. *NeuroImage*, 35:1459–1472, 2007.

[63] W. Y. I. Tseng, V. J. Weeden, T. J. Reese, R. N. Smith, and E. Halpern. Diffusion Tensor MRI of Myocardial Fibers and Sheets: Correspondence With Visible Cut-Face Texture. *Journal of magnetic Resonance Imaging*, 17:31–42, 2003.

[64] D. S. Tuch. *Diffusion MRI of Complex Tissue Structure*. PhD thesis, Massachusetts Institute ot Technology, January 2002.

[65] D. S. Tuch. Q-Ball Imaging. *Magnetic Resonance in Medicine*, 52:1358–1372, 2004.

[66] D. S. Tuch, T. G. Reese, M. R. Wiegell, N. Makris, J. W. Belliveau, and V. J. Weeden. High Angular resolution Diffusion Imaging Reveals Intravoxel White Matter Fiber Heterogeneity. *Magnetic Resonance in Medicine*, 48:577–582, 2002.

[67] V. J. Wedeen, P. Hagmann, W. Y. I. Tseng, T. G. Reese, and R. M. Weisskoff. Mapping Complex Tissue Architecture With Diffusion Spectrum Magnetic Resonance Imaging. *Magnetic Resonance in Medicine*, 54:1377–1386, 2005.

[68] E. X. Wu and M. M. Cheung. MR diffusion kurtosis imaging for neural tissue characterization. *NMR Biomed.*, 23:836–848, 2010.

[69] E. X. Wu, Y. Wu, J. M. Nicholls, J. Wang, S. Liao, S. Zhu, C. P. Lau, and H. F. Tse. MR Diffusion tensor Imaging Study of Postinfarct Myocardium Structural Remodeling in a Porcine Model. *Magnetic Resonance in Medicine*, 58:687–695, 2007.

[70] E. X. Wu, Y. Wu, K. Tang, J. Wang, M. C. Ng, E. S. Sang, C. W. Chan, S. Zhu, C. P. Lau, and H. F. Tse. Study of myocardial fiber pathway using magnatic resonance diffusion tensor imaging. *Magnetic Resonance Imaging*, 25:1048–1057, 2007.

[71] M. T. Wu, M. Y. M. Su, Y. L. Huang, K. R. Chiou, P. Yang, H. B. Pan, T. Reese, V. J. Weeden, and W. Y. Tseng. Sequential Changes of Myocardial Microstructure in Patients Postmyocardial Infarction by Diffusion-Tensor Cardiac MR - Correlation With Left Ventricular Structure and Function . *Circ Cardiovasc Imaging*, 2:32–40, 2009.

[72] Y. Wu, C. Zou, W. Liu, W. Liao, w. Yang, D. A. Porter, X. Liu, and E. X. Wu. Effect of b-value in revealing postinfarct myocardial microstructural remodeling using MR diffusion tensor imaging. *Magnetic Resonance Imaging*, 31:847–856, 2013.

[73] J. Xu, M. Does, and J. C. Gore. Sensitivity of MR Diffusion Measurements to Variations in Intracellular Structure: Effects of Nuclear Size. *Magnetic Resonance in Medicine*, 61:828–833, 2009.